# COUPLED FLOW FIELD AND HEAT TRANSFER IN AN ADVANCED INTERNAL COOLING SCHEME

A thesis accepted by the Faculty of Aerospace Engineering and Geodesy
of the Universität Stuttgart
in partial fulfillment of the requirements for the degree of
Doctor of Engineering Sciences (Dr.-Ing.)

by
Filippo Coletti
born in Perugia, Italy

| | |
|---|---|
| Committee chair: | Apl. Prof. Dr.-Ing. Ulrich Rist |
| Committee members: | Prof. Dr.-Ing. habil. Bernhard Weigand |
| | Prof. Dr. Tony Arts |

Date of defense: 21st October, 2010

Institute of Aerospace Thermodynamics
Universität Stuttgart
2010

*Misura ciò che è misurabile, e rendi misurabile ciò che non lo è.*

Galileo Galilei (1564 – 1642)

*A Marta Vázquez Álvarez*

# Acknowledgments

A thesis is never a conclusive accomplishment. In the same way, the list of persons who deserve being thanked by its author can never be complete. Nevertheless, it is a pleasant exercise of memory to recall at least some of the many exceptional persons who contributed, knowingly and unknowingly, to the successful end of my doctoral carrier.

Prof. Tony Arts has been my supervisor at VKI throughout these years. Since he picked me up as a stagiaire, he guided me attentively and still let me the freedom I needed. He dispensed countless hints, advises, lessons. He taught me anything from radial equilibrium to thermocouples calibration. He taught me that an experiment starts in the mind of the investigator. He taught me to apply to my own work the same criticism as if it was somebody else's. He taught me that asking the right questions is the key for the interpretation. He taught me that the spark in the eyes of a researcher shall never die out. And he taught me all this with the force of the example. His door has always been open, and every time I entered he had the right word at the right time. He is more than a mentor, he is a true friend.

It is a privilege for me to have Prof. Bernhard Weigand as a supervisor. I benefited from his deep knowledge of fluid dynamics and heat transfer, his scientific excellence and his insightful comments. Even more, I enjoyed the genuine enthusiasm he puts in anything he does. He is a terrific lecturer, and I was honored to have him speaking at the VKI Lecture Series in Internal Cooling in Turbomachinery.

The former VKI director Mario Carbonaro offered me the possibility of joining the Institute. I did not fully realize the implications at the moment, but today I can only thank him, together with his predecessors, who spent their lifetime making the von Karman Institute what it is.

Several members of the VKI faculty have contributed to make this work more solid, pushing me to look at things from different perspectives. The constructive criticism of Prof. Jean-Marie Buchlin opened the way to some of the most interesting findings of this work. I gratefully acknowledge the sharp questions and the pertinent remarks of Prof. René Van den Braembussche and Prof. Michel Riethmuller. Prof. Tom Verstraete has wrestled with conjugate heat transfer as much as I have: it was a pleasure to have him at my side in this fight.

Roberto García Casado was my advisor for only few months, but I did not forget his kindness and his sincerity. Later on, every time I worked with a younger student, it would be like looking at myself through the eyes of Roberto. His advises stayed with me throughout these years, more than he can imagine.

In pretty much everything I did for this thesis, I was assisted by one or more students. They called me "advisor", but we were and are just friends, putting efforts together. Alessandro Armellini, Luca Patricelli, Emanuele Facchinetti, Daniele Forlani and Manfredi Scialanga have given me more than what I can express in words. The hours in the lab, the problems, the solutions, the moments of satisfaction and the ones

of discouragement wouldn't have felt the same without them. They never give up. They are my team.

I have had the chance of crossing my path with some outstanding colleagues working in my same field, both at VKI and ITLR. Alberto Di Sante has been my advisor-in-pectore in the early stage of my investigation. Beni Cukurel has been the dialectic pole I needed in several intense and fruitful discussions. It was a pleasure to share ideas with Peter Vass across the invisible line that separates experiments and numerics. Marco Schüler took his time to train me in transient liquid crystals thermography with unlimited patience. It was a pleasure to introduce Sebastian Spring and Rico Poser to the audience before their impressive presentations at the VKI Lecture Series.

I read a lot. Someone I know says I read too much. As far as fluid dynamics goes, I will lovingly blame Christelle and Evelyne: they were tireless in providing any paper or book I wanted, whether it was in the VKI archive or not. Un grand merci.

The reader should realize that this thesis is not just made of words, thoughts and ideas. There's that, too. But it is as well made out of Plexiglas, steel, wood, Inconel. The work of the VKI engineers, technicians and workers (in particular in the Turbomachinery and Propulsion Department) was instrumental. Julien, Yves, Pierre, Jean-Christophe, Carlo, Mohammed, Terence, Walter, Maurizio, Vincent, Willy: my gratitude goes to them all.

At VKI (and in its neighborhood that they call Brussels) I found unforgettable friends. Marco Pau has been the voice and the face of my thoughtful moments since our Diploma Course. If I didn't have to convince him about my ideas, I wouldn't believe in them as much today. Flora Tomasoni has been sitting two meters on my right for three years. I can't count the times she saved my life with a post-it. Our talks at the whiteboard will be echoing in our office for years to come. Michael Bilka was there every time my life took a spin in the last five years, and it happened quite a few times. Before meeting Mike I didn't know I had a brother, so different from me, so similar to me. Tomás Hofer and Konstantinos Myrillas were my family for nine months in Rhode-Saint-Genèse, Avenue des Tilleuls 73. They kept me from dying from starving, and made those days as magic as only a Diploma Course can be. Alessandro Gambale gave me undeniable demonstration of how you can be a king from inside the VKI basement. If I think back to the endless conversations we had during our stage, it strikes me how many of his predictions came true. I shared with Marco Panesi my first accommodation in Belgium. He tried to convince me to escape, but I could read in between the lines: thank you Marco for making me like this place.

Raf Theunissen, Diego Paolucci, Kate Bernstein, Domenico Verrastro and I tumbled several times inside and outside a car, one fatidic night of November during my Diploma Course. When we all stood up after all, they were still my best friends. Now they are spread at the four corners of the world. But there are links that you cannot break.

It is a plain fact that at VKI people come and go. It's in the very nature of the Institute. Andrés, Mario, Jason, Giacomo, Baris, Javier, Julien Bodart, Sergio, Catherine, Fabio, Jan, Mehmet, Francesco, Marco Maglio, Nicolas, Michelangelo, Alessandro Parente, Thomas, Tim, Jeremy, Elisa (and counting) arrived/left sometime

during my stay. They did (or will) wander away. It does not matter: I thank them for being there when I needed, and for making these years unique.

At the end of this journey, my family deserves my gratitude more than anybody. My father Maurizio, my mother Anna Maria and my sister Federica loved me enough to do the most difficult, the most important thing: to let me go. At the same time they have managed to be at my side every day, following each experiment, each presentation, each deadline of these years from one thousand miles away, with unshakable trust in my potential. Grazie.

At the beginning of my PhD I thought I was past the most startling period of my life. And then came Marta. She reminded me things I had forgotten, reshaped my list of priorities, and changed the language of my thoughts. In the months while I was writing, while the work was getting hold of me, while books and papers and notes were piling up around us, she has put me in the condition of reaching the goal, and has stood my mental and physical absence in the way she does every thing: with infinite grace. The last words of this page, as any other word henceforth, are dedicated to her, who holds my love.

*Filippo Coletti*

*Bruxelles, August 2010*

# Table of contents

# List of symbols

## Abbreviations

| | |
|---|---|
| BC | boundary condition |
| CCD | Charge Coupled Device |
| CFD | Computational Fluid Dynamics |
| DC | Direct Current |
| EF | Enhancement Factor |
| FEM | Finite Element Method |
| FPA | Focal Plane Array |
| IFOV | instantaneous field of view |
| IR | Infrared |
| LDV | Laser Doppler Velocimetry |
| NETD | Noise Equivalent Temperature Difference |
| PIV | Particle Image Velocimetry |
| RANS | Reynolds-average Navier Stokes |
| TLC | Thermocromic Liquid Crystals |
| VKI | von Karman Institute |

## Roman symbols

| | | |
|---|---|---|
| $a_{ij}$ | | exponent of basic dimensional units (Eq. 2.2) |
| $A_h$ | [$m^2$] | heated area in convective heat transfer |
| $A_{rib}$ | [$m^2$] | wet surface area of the rib (Eq. 7.5) |
| $A_0$ | [$m^2$] | heated area in conjugate heat transfer |
| $AI$ | | average pixel intensity level (Eq. 4.1) |
| $Bi$ | | Biot number (Eq. 2.20) |
| $BI$ | | background pixel intensity level (Eq. 4.1) |
| $c_P$ | [$Jkg^{1-}K^{-1}$] | fluid specific heat |
| $C$ | | numerical constant (Eq. 4.1) |
| $C_P$ | | pressure coefficient (Eq. 5.4) |

| | | |
|---|---|---|
| $d$ | | n. of independent dimensionless groups (Eq.2.4)<br>characteristic wall thickness |
| $D$ | [m] | hydraulic diameter |
| $e$ | [m] | rib height |
| $E$ | [$Wm^{-2}$] | radiative power (Eq. 4.14) |
| $Ec$ | | Eckert number (Eq. 2.10) |
| $f$ | [m] | focal length<br>Darcy-Weisbach friction factor (Eq. 5.2) |
| *G0,…, G4* | | investigated geometries |
| $h$ | [$Wm^{-2}K^{-1}$] | heat transfer coefficient (Eq. 2.7) |
| $i$ | | index |
| $I$ | [A] | current |
| *Imp I, II, III* | | jet impingements |
| *IRMS* | | *rms* of light intensity fluctuations (Eq. 4.1) |
| $k$ | [$Wm^{-1}K^{-1}$]<br>[$m^2s^{-2}$] | thermal conductivity<br>turbulent kinetic energy |
| $K$ | | solid-to-fluid thermal conductivity ratio (Eq. 2.17) |
| $l$ | [m] | turbulent length scale |
| $L$ | [m] | Channel length (Eq. 5.2) |
| $m$ | | number of basic unit (Eq. 2.2) |
| $M$ | [$Wm^{-2}$] | total emissive power (Eq. 4.12) |
| $M_\lambda$ | [$Wm^{-3}$] | spectral emissive power (Eq. 4.12) |
| $n$ | | number of physical variables (Eq. 2.4)<br>mean refraction index (Eq. 4.4) |
| $N$ | | Number of independent samples (Eq. 4.2, 4.3) |
| $Nu$ | | Nusselt number (Eq. 2.11) |
| $p$ | [m] | physical variable (Eq. 2.2),<br>helix pitch of liquid crystals molecules (Eq. 4.4 ) |
| $P$ | [Pa] | pressure |
| $Pr$ | | Prandtl number (Eq. 2.9) |
| $PR$ | [%] | percentage of pressure recovery (Eq. 5.3) |
| $q$ | [$Wm^{-2}$] | heat flux |
| $Q$ | [W] | power heat |

| | | |
|---|---|---|
| $r$ | | rank of the matrix $a_{ij}$(Eq. 2.4) |
| *rms* | | root mean square |
| *Re* | | Reynolds number (Eq. 2.8) |
| *S1,S2* | | separation lines |
| $T$ | [K] | temperature |
| *th* | [m] | wall thickness |
| *TS* | | turbulent flow structure |
| $u,u',u'',v,w$ | [$ms^{-1}$] | fluctuating velocity components along axes $x, y', y'', z$ |
| $U,U',U'',V,W$ | [$ms^{-1}$] | Mean velocity components along the axes $x, y', y'', z$ |
| $V$ | [V] | Voltage |
| *VS1, 2* | | upward flow structures |
| $x, y', y'', z$ | | coordinate axes |
| $X_i$ | | basic unit (Eq. 2.2) |
| $y^+$ | | wall distance in wall units |
| $Y$ | | non-dimensional abscissa along mid-wall slot span |
| $Z_c$ | | confidence coefficient (Eq. 4.2, 4.3) |

## Greek symbols

| | | |
|---|---|---|
| $\alpha$ | [deg] | angle of search of the "tracking bug" |
| $\delta$ | [K] | error tolerance in wall temperature measurement |
| $\Delta t$ | [s] | time step for numerical integration |
| $\varepsilon$ | [$m^2s^{-3}$] | normalized error (Eq. 4.2, 4.3)<br>surface emissivity<br>fin effectiveness (Eq. 7.4) |
| $\varepsilon_\lambda$ | [$m^{-1}$] | monochromatic emissivity |
| $\eta$ | | fin efficiency (Eq. 7.3) |
| $\theta$ | [K]<br>[deg] | temperature head (Eq. 2.6)<br>angle of incident light (Eq. 4.4) |
| $\Theta$ | | Non-dimensional wall temperature (Eq. 2.16) |
| $\lambda$ | [m]<br>[m] | reflected light wavelength (Eq. 4.4)<br>electromagnetic radiation wavelength (Eq. 4.12) |
| $\mu$ | [$m^2s^{-1}$] | fluid dynamic viscosity |
| $\Pi$ | | dimensionless group (Eq. 2.2) |

| | | |
|---|---|---|
| $\rho$ | [$kgm^{-3}$] | fluid density<br>reflectivity (Eq. 4.13) |
| $\sigma$ | | standard deviation operator |
| | [$Wm^{-2}K^{-4}$] | Stefan-Boltzmann constant |

## Subscripts

| | |
|---|---|
| *0* | outer surface<br>total condition |
| *amb* | ambient |
| *avg* | average |
| *aw* | adiabatic wall |
| *b* | bulk |
| *base* | base surface |
| *cond* | conductive |
| *conv* | convective |
| *exit* | exit slot |
| *f* | fluid |
| *fin* | real fin |
| *h* | heated wall |
| *id* | ideal |
| *Inc* | Inconel |
| *inlet* | inlet section |
| *Joule* | Joule effect |
| *mid* | mid-wall slot |
| *nh* | non-heated wall |
| *norm* | normalized |
| *Plexi* | Plexiglas |
| *rad* | radiative |
| *s* | static condition |
| *supply* | air supply |
| *w* | wall surface |

# Abstract

State-of-the-art gas turbines are designed to operate at turbine inlet temperatures in excess of 1850 K. Such temperature levels are sustainable only by means of an aggressive and efficient cooling of the components exposed to the hot gas path. Not only the maximum metal temperature needs to be kept below the safety limits, but the thermal field must be reasonably uniform, in order to limit the thermal stresses. This requires from the designer the most accurate knowledge of the local heat transfer rate. The need for such detailed information is in conflict with some common practices in the cooling system design: numerical simulations are often compared against area-averaged experimental data; the link between coolant flow field and heat transfer rates is scarcely analyzed; moreover, the coupling between convection and conduction is hardly taken into account.

The present thesis aims at the aero-thermal characterization of a trailing edge cooling channel geometry. Cooling the trailing edge, one of the life-limiting parts of the airfoil, represents an especially challenging task since the aerodynamic requirement of high slenderness is conflicting with the need of integrating internal passages. The focus of the study is on three main aspects of the internal cooling technology: (i) the details of the coolant flow field; (ii) the contribution of the obstacles' surface to the heat transfer; and (iii) the effect of the conduction through the cooling channel walls.

The investigated cooling channel geometry is characterized by a trapezoidal cross-section. It has one rib-roughened wall and slots along two opposite walls. The coolant passes through a smooth inlet channel upstream of the investigated cavity; it crosses the divider wall through a first row of inclined slots, producing crossing-jets; the latter impinge on the rib-roughened wall, and the jet-rib interaction results in a complex flow pattern, rebounding the coolant towards the opposite smooth wall; finally the air exits through a second row of slots along the trailing edge. Such a scheme represents a combination of internal forced convection cooling and impingement cooling. An engine-representative Reynolds number equal to 67500 is defined at the entrance of the inlet channel.

A comprehensive experimental investigation is carried out on a magnified model of the channel, at a scale of 25 : 1 with respect to engine size (applied to both the cavity volume and the walls thickness). The main flow structures are identified and characterized by means of particle image velocimetry, allowing to deduce a model of the highly three-dimensional mean flow. Each jet is shown to impinge on the three ribs in front of the slot, and the jet-rib interaction produces two upward deflections in each inter-rib domain.

Distributions of heat transfer coefficient are obtained by means of liquid crystals thermography on the rib-roughened surface as well as on the opposite smooth wall in a purely convective regime, with a uniform heat flux imposed at the solid-fluid interface. The thermal patterns on the channel walls show the footprints of the flow features detected by the velocity measurements. Globally, the top side of the rib shows

the highest Nusselt number among the investigated surfaces. The presence of the ribs enhances the global heat transfer level (averaged on all surfaces) by 14%.

The aero-thermal results suggest a definite margin for improvement of the heat transfer performance by varying one or more geometrical parameters. In this perspective, the ribs have been tapered and shifted with respect to the slots position. Both expedients have proven to be useful in reducing the extent and intensity of the aforementioned hot spots in the vicinity of the ribs: an enhancement of about 20% in area-averaged heat transfer rate is achieved with respect to the standard configuration.

The thermal behavior of the ribbed wall has also been investigated in conjugate heat transfer regime, in order to study the effect of the wall conduction on the thermal levels. By matching the solid-to-fluid thermal conductivity ratio found in an engine, the correct thermal boundary conditions for the convective problem are attained, which guarantees full similarity between laboratory model and engine reality. Infra-red thermography coupled to a finite element analysis is used to retrieve the whole thermal pattern through the considered rib-roughened wall. Nusselt number levels in conjugate regime differ by up to 30% locally and 25% globally with respect to the purely convective results. Neglecting wall conduction when evaluating the heat transfer coefficient leads to underestimating the maximum surface temperature by 26 to 33 K at engine conditions. Decreasing the wall thermal conductivity increases the overall heat transfer coefficient on the ribbed surface. However lower conductivities amplify local temperature gradients and hot spots.

# Zusammenfassung

Heutige Gasturbinen sind darauf ausgelegt, bei Turbineneintrittstemperaturen über 1850K betrieben zu werden. Solch hohe Temperaturniveaus sind nur mittels gezielter und effizienter Kühlung der thermisch hochbeanspruchten Bauteile realisierbar. Hierbei ist es zum einen notwendig, die Maximaltemperatur des Metalls unterhalb der Schmelztemperatur zu halten. Zum anderen ist auf eine gleichmäßige Temperaturverteilung zu achten, um thermisch bedingte Spannungen zu minimieren. Für die Auslegung von Gasturbinenschaufeln kommt daher einer möglichst genauen Bestimmung der lokalen Wärmeübergangszahl eine besondere Bedeutung zu. Die Nachfrage hiernach steht jedoch oft im Widerspruch zu etablierten Auslegungsverfahren: hier werden üblicherweise die Ergebnisse aus numerischen Simulationen mit flächengemittelten Werten aus Experimenten verglichen. Die Wechselwirkungen zwischen dem Strömungsfeld des Kühlmediums und der Wärmeübergangszahl sind nur unzureichend analysiert. Zudem wird die Kopplung zwischen Konvektion und Wärmeleitung bisher kaum berücksichtigt.

Das Ziel dieser Arbeit ist die aero-thermodynamische Charakterisierung des Kühlkanals in der Hinterkante einer Gasturbinenschaufel. Die Kühlung der Hinterkante stellt eine besondere Herausforderung dar, da an dieser Stelle der Einbau eines internen Kühlkanals durch die geometrischen Vorgaben stark begrenzt ist. Die Schwerpunkte dieser Arbeit liegen auf drei wichtigen Aspekten interner Kühltechnologie: (i) die genaue Beschreibung des Strömungsfeldes des Kühlmediums; (ii) der Beitrag der Rippenfläche zum Wärmeübergang; (iii) den Einfluss der Wärmeleitung durch die Wände des Kühlkanals.

Der untersuchte Kühlkanal hat einen trapezförmigen Querschnitt. Auf einer Wand befinden sich Rippen während die zwei gegenüberliegenden Wände mit Schlitzen versehen sind. Das Kühlmedium gelangt stromauf durch einen glatten Einlaufkanal in die Testkammer. Dabei durchquert es eine Trennwand mit einer Reihe schräg angeordneter Schlitze, wodurch sogenannte „crossing-jets“ entstehen, die anschließend auf die berippte Wand prallen. Durch die Wechselwirkung zwischen Strahl und Rippen entstehen komplexe Strömungsmuster, welche das Kühlmittel zur glatten gegenüberliegenden Wand zurückprallen lassen. Schließlich strömt die Luft durch eine zweite Reihe von Schlitzen an der Hinterkante aus. Solch ein System repräsentiert eine Kombination aus berippter interner Kühlung und Prallkühlung. Am Einlauf des Kühlkanals wird eine Reynolds-Zahl von Re=67500 eingestellt, welche die Bedingungen in einer realen Gasturbine wiedergeben soll.

Es wird eine umfassende experimentelle Untersuchung an einem vergrößerten Modell (Maßstab 25:1) durchgeführt. Die Hauptströmungsstrukturen werden mittels PIV visualisiert. Dadurch ist es möglich, auf ein dreidimensionales Modell der Hauptströmungsrichtung zu schließen. Es konnte gezeigt werden, dass jeder „jet“ auf den drei Rippen vor dem Schlitz auftrifft und dass durch diese Interaktion in jedem Rippenzwischenraum zwei Ablenkungen stromauf erzeugt werden.

Die Verteilungen des Wärmeübergangskoeffizienten an der berippten sowie an der gegenüberliegenden glatten Wand wurden mit Hilfe von Flüssigkristallen bestimmt. Diese Daten wurden in einem System mit gleichmäßigem Wärmestrom gemessen, welcher an der Grenzfläche Feststoff-Flüssigkeit erzeugt wurde. Die Wärmeübergangsmuster an der Kanalwand zeigen die Spuren der Strömungseigenschaften aus den Geschwindigkeitsmessungen. Ganzheitlich betrachtet zeigt die Oberseite der Rippen die höchste Nusselt-Zahl unter allen betrachteten Oberflächen. Die Rippen erhöhen den globalen Wärmeübergang um 14%.

Die aerothermischen Ergebnisse legen nahe, dass eine bestimmte Grenze zur Verbesserung des Wärmeübergangs bei Änderungen einer oder mehrerer geometrischer Parameter existiert. Vor diesem Hintergrund wurden die Rippen schräg angeordnet und relativ zu den Schlitzen versetzt. Beide Maßnahmen haben bewiesen, dass sie zur Verringerung von Ausdehnung und Intensität der oben genannten Hotspots beitragen: ein Anstieg um etwa 20% in der gemittelten Wärmeübergangszahl bezogen auf die Standardkonfiguration ist zu verzeichnen.

Das thermische Verhalten der berippten Wand wurde auch im Bereich des konjugierten Wärmeübergangs untersucht, um den Einfluss der Wärmeleitung der Wand auf den Wärmeübergang zu untersuchen. Durch Einhaltung eines für Gasturbinen realistischen Verhältnisses der thermischen Leitfähigkeit (fest-flüssig), wurden korrekte thermische Randbedingungen für das Problem erlangt. Diese garantieren die Gleichheit zwischen den Bedingungen im Labor und den realen Bedingungen im Triebwerk. Um alle thermischen Muster auf der betrachteten Wand mit Rippen zu bestimmen, wurde die Infrarotthermographie gemeinsam mit der Finite-Elemente-Analyse eingesetzt. Die Nusselt-Zahl in einem konjugierten System weicht lokal um 30% und global um 25% von den Ergebnissen des rein konvektiven Wärmeübergangs ab. Dies bedeutet, dass die maximale Oberflächentemperatur unter Realbedingungen um 26 bis 33 K von den Ergebnissen mit einem konstanten Wandwärmestrom als Randbedingung abweicht. Eine Verringerung der Wärmeleitfähigkeit der Wand führt zu einer Erhöhung des gesamten Wärmeübergangs an der berippten Oberfläche. Andererseits verstärken niedrigere Wärmeleitfähigkeiten lokale Temperaturgradienten und Maximalwerte.

# Chapter 1 – Introduction

This first chapter sets the background for the present research effort. Simple technological considerations demonstrate the importance of cooling the hot-gas-path components of modern gas turbines. The focus is on the internal cooling of the turbine blades. A review of the literature evidences the limited attention received by three relevant aspects of the internal cooling process: the details of the velocity fields, the contribution of the turbulators to the heat extraction, and the effect of wall conduction. This thesis finds its motivation in the need of emphasizing those aspects, in the frame of the experimental investigation of an advanced trailing edge cooling scheme.

## *1.1 – Gas turbines for propulsion and power generation*

Gas turbines engines are internal combustion engines: the expansion of the high temperature and pressure gases produced by the combustion directly applies a force to the movable component of the engine. Among the various means of producing either thrust or power, the gas turbine engine is one of the most satisfactory; its main advantage is the high thrust-to-weight ratio. The range of applications where gas turbines are used is enormous, therefore any small gain in thermal efficiency and performance translates into a major economic impact worldwide.

A simple gas turbine comprises three main sections: a compressor, a combustor and a power turbine. The pressure of the evolving fluid, generally air, is increased in the compressor. The flow temperature is raised in the combustor, by igniting fuel in dedicated burners. The highly energetic gas from the combustor is expanded through a turbine that drives the compressor, to which it is connected via a shaft running through the center of the engine. Behind the turbine the gas still contains a significant amount of energy which can be extracted in various forms: in aircrafts the surplus energy is transformed into a high velocity jet; for stationary, power generating gas turbines, the extra energy is converted into shaft-power for a generator, which converts the mechanical energy into electrical power. Figure 1.1 presents a schematic jet engine layout, while a sectioned General Electric J85 turbojet is displayed in Fig. 1.2.

Gas turbines are thermodynamically described by the Joule cycle (also named Brayton cycle, Fig. 1.3, left). In the ideal cycle, compression and expansion of a gas are adiabatic and isentropic, and the change of kinetic energy is negligible; there are no pressure losses in the combustion chamber and exhausting ducts; the working fluid is a perfect gas of constant properties. Despite such simplifications, the analysis of the ideal cycle leads to instructive observations, including the following one: increasing the maximum temperature of the cycle (exit of the combustor/inlet of the high pressure turbine, point 3 in Fig. 1.3) augments the extracted work. However the ideal cycle thermal efficiency does not depend on the maximum temperature. Conversely, considering a real cycle, i.e. taking into account the losses associated with irreversible

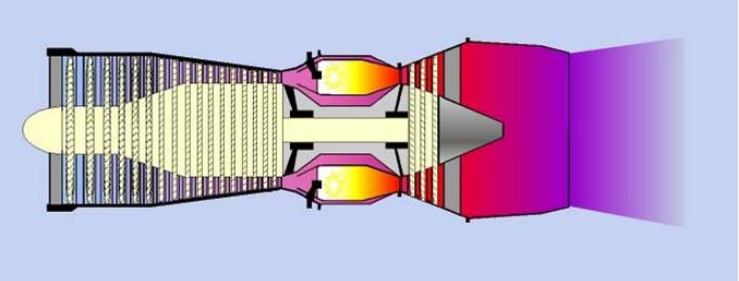

**Fig. 1.1** **Jet engine layout (source: Cervenka (2000))**

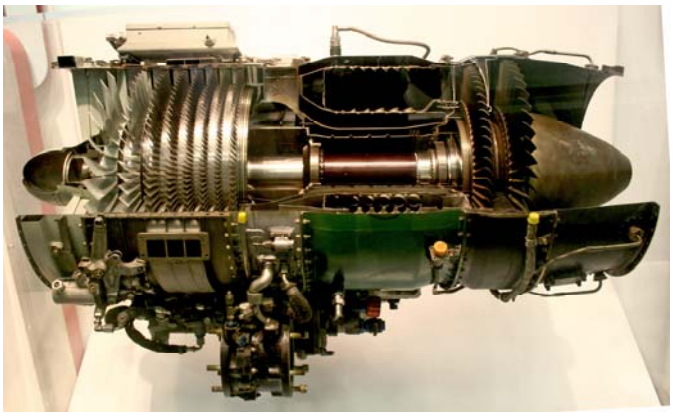

**Fig. 1.2** **J85 General Electric Turbojet (source: http://www.456fis.org)**

transformations, the efficiency increases with turbine inlet temperature. Finally the specific thrust, defined as the thrust output per unit mass flow through the engine, also increases with turbine inlet temperature. This is impressively demonstrated in Fig. 1.4, where the specific core power (which can be related to the specific thrust) of various gas turbine engines is plotted against rotor inlet temperature.

More details on the impact of increasing the turbine inlet temperature on the performance of ideal and non-ideal gas turbines cycles can be found in Lakshminarayana (1996) and Saravanamuttoo et al. (2001).

## *1.2 – Blade cooling technology and design*

State-of-the-art gas turbines are designed to operate at turbine inlet temperatures in excess of 1850 K. The materials most commonly employed in the high temperature parts include high-temperature, high-strength nickel or cobalt-based super-alloys, coated with yttria-stabilized zirconia oxide ceramics (thermal barrier coating, TBC). However, since the super-alloys cannot withstand temperatures above 1350 K, cooling

must be applied to the turbine components exposed to the combustion gases. In general the coolant is air bled from the high pressure compressor, which bypasses the combustor and enters the blade through its root. The coolant is then ejected at the

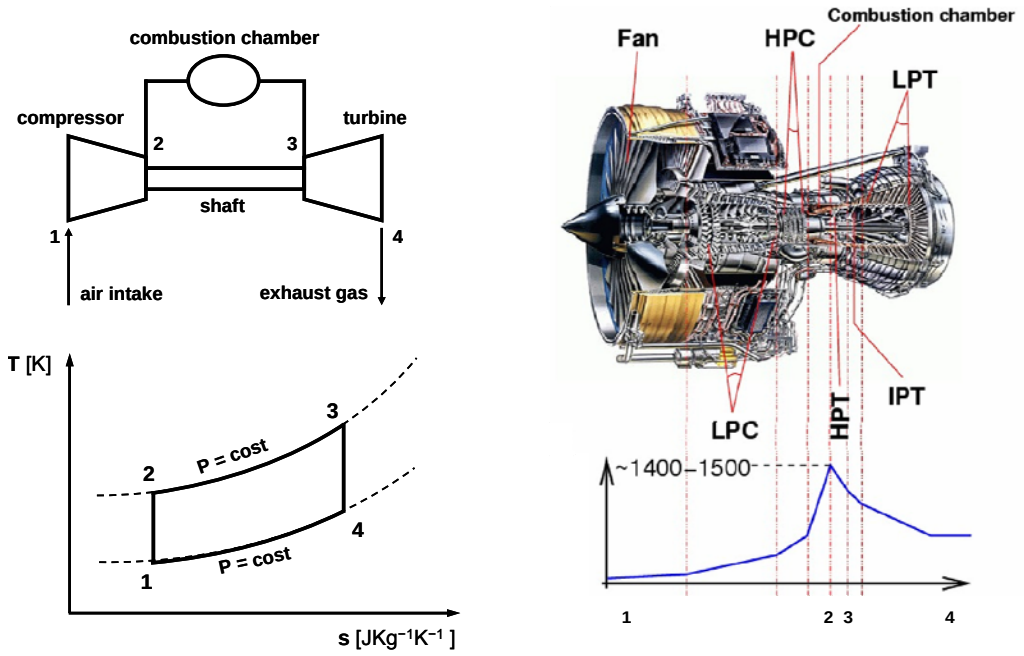


**Fig. 1.3** **On the left: schematic lay-out of a gas turbine (top) and the ideal Joule cycle (bottom). On the right: gas temperature evolution (in degrees Celsius) across the Rolls- Royce Trent 800 (after Cervenka (2000))**

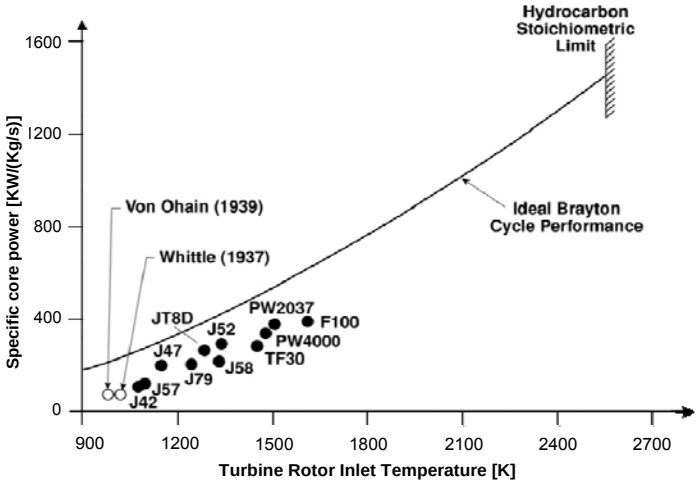


**Fig. 1.4** **Evolution of gas turbine engines performance in terms of specific core power (source: Koff (1991))**

blade tip, through trailing edge cooling slots or through surface film cooling holes. More than 20% of the discharge air from the compressor is used to cool the high-pressure turbine, which presents a severe penalty on the thermodynamic efficiency. Still, for both aeronautic and power gas turbines, the advantages of cooling outweigh the various disadvantages, including the technical difficulties of designing the cooling devises. Figure 1.5 shows the historical development of turbine inlet temperatures, highlighting the separate impact of materials improvement and cooling technology.

Several cooling techniques are employed in the high pressure stages of the turbine, as represented in Fig. 1.6: in general the airfoil is cooled by a combination of internal convective cooling, i.e. directing coolant inside the hot gas path components, and external film cooling, i.e. bleeding internal cooling flows along the exterior skin of the

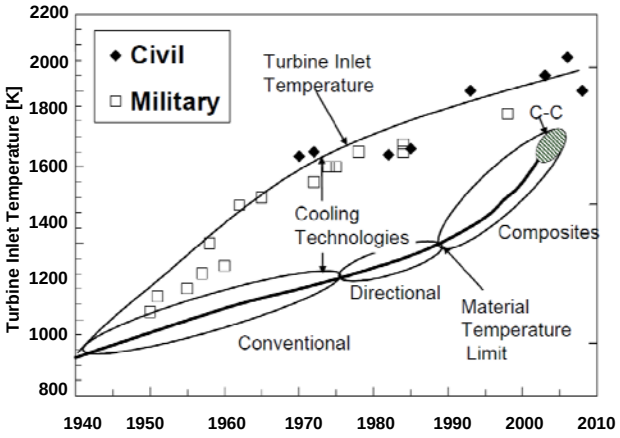


**Fig. 1.5** **Evolution of turbine inlet temperature and blade material temperature limits (source: Ballal and Zelina (2004))**

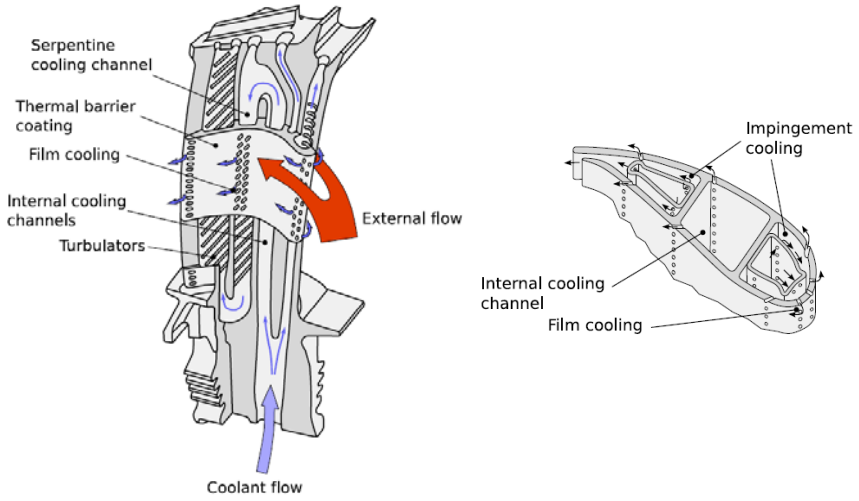


**Fig. 1.6** **Overview of cooling techniques for gas turbine blades**

components to form a protective layer. In the former case the heat transfer coefficients need to be maximized, in order to augment the heat extraction from the material; in the latter case vice versa the lowest convective heat transfer levels for the blade external surface are targeted, so to limit the heat flux from the hot stream.

In internal cooling architectures the coolant flows through channels, whose walls are most often roughened with turbulators such as ribs, pins and dimples. These devices enhance the cooling capability by augmenting convective heat transfer and turbulence transport coefficients, besides increasing the surface area for convective heat transfer. High performance is achieved when forced convection is coupled with impingement cooling: the coolant bleeds via rows of holes through a perforated wall separating two cavities; jet arrays are produced and a large heat transfer enhancement is achieved in the impingement regions. An extensive review of mechanisms and performance of heat transfer cooling techniques was presented by Han et al. (2000).

The design of the cooling systems for turbine airfoils is a complex process, which requires a multi-disciplinary approach. Not only the maximum component temperature needs to be kept below the safety limits, but its thermal field must be reasonably uniform, in order to reduce thermo-mechanical stresses. This requires from the design team the highest control of the techniques at hand. In reviewing the cooling design process, Bunker (2006) divides it in four levels: the first level coincides with the preliminary design of the engine, in which the target performance of the cooling system is set, including coolant consumption, turbine airfoil lifetime and inspection intervals; the following level concerns the conceptual design of the components, based on 1D, 2D or 3D complexities, and is primarily used to compare various options in cooling design; the third level includes surrounding effects and constraints from aerodynamics, material properties, mechanical loads etc., and it is most of the time performed at one single steady-state operating condition (e.g. 100% load); the last level addresses the operational transient aspects, to determine if requirements or constraints are violated under conditions such as start-up and restarts.

It is worth noticing that today large part of the design tools employed at the various levels are developed from correlations, simulations and experiments carried out in simplified environments, especially as far as the thermal boundary conditions are concerned. This is due on one hand to a lack of extended data sets, and on the other hand to the desire of speeding up the design process, in view of the shortest time-to-market. Nevertheless, the decisive impact of the boundary conditions seriously questions the admissible level of simplification, as it will be discussed at length in Chapter 2 and Chapter 7.

## *1.3 – Literature review*

This section concerns selected aspects relevant to internal cooling technology addressed by previous contributions. The focus is on those features which are significant for the present case, without attempting to summarize the enormous body of literature concerning internal cooling techniques for turbine blades. The topic was

reviewed by Han et al. (2000) and Weigand et al. (2006), while von Wolfersdorf and Weigand (2010) outlined the fundamental physical aspects of internal cooling and reviewed several heat transfer measurement techniques.

### 1.3.1 – Internal cooling in rib-roughened channels

The literature about rib-roughened channels is particularly extensive. The first experimental studies focused on cavities of rectangular cross section: the seminal work of Han and coworkers (Han et al. (1978) Han (1984), Chandra et al (1988)) showed how the heat transfer performance is strongly influenced not only by the Reynolds number but also by geometrical parameters such as the passage aspect ratio, the blockage ratio, the rib spacing and the rib angle of attack. The importance of the rib shape was addressed by Liou and Hwang (1993) and Taslim and Spring (1994). Taslim and his group also performed several studies on channels of non-rectangular section (Taslim et al. (1997)), which is a more realistic situation for cooling cavities located at the leading edge or the trailing edge of the airfoil.

A number of authors stressed the major contribution of the heat transferred by the rib, recognizing that the heat transfer levels are in general higher on the turbulators' surface than elsewhere in the channel (Taslim and Wadsworth (1997), Wang et al. (1998)). Yet in most studies only an average heat transfer value for each obstacle is presented, and reports showing spatially resolved heat transfer distributions over the rib surface are scarce. Metzger et al. (1988) published span-averaged Nusselt number distributions on the rib-roughened surface of a rectangular channel. Liou and Hwang (1992) reported convection coefficients around the perimeter of a ribbed channel wall. Local heat transfer levels on a rib-roughened wall including the tip of the rib were presented by Shen et al. (1996) and Ligrani and Mahmood (2003), but no information was given for the lateral sides of the turbulators. The lack of knowledge of local heat transfer on the rib surfaces constitutes an undesirable deficiency both when designing and comparing cooling schemes and when assessing the reliability of computational tools. An exception in this sense is represented by the work of Cakan (2000), where detailed heat transfer coefficient distributions were reported for all the surfaces of the high blockage ratio rib-roughened channel studied by the author.

### 1.3.2 – Impingement cooling in smooth and ribbed channels

Among the different internal cooling techniques, impingement cooling is a discipline per se, and various reviews exist (e.g. Viskanta (1993), Han and Goldstein (2001)). Here we are mostly interested in multiple jets applications recently reviewed by Spring and Weigand (2010), which present additional complexity related to the interaction between adjacent jets and between jets and crossflow. Florschuetz et al. (1980), Bunker and Metzger (1990) and van Treuren et al. (1994), among others, showed the influence of several parameters including: jets Reynolds number, orifice plate-to-target plate distance, jets spacing, open area ratio, and jet-to-cross flow

momentum ratio. Ekkad et al. (2000) investigated the effect of the jets inclination with respect to the target plate. Gillespie et al. (1998) looked at the effect of extraction holes opened in the target plate.

The large number of influencing factors reflects the flexibility of the technique, which can be adjusted to the specific need of the case. This is all the more true if impingement cooling is used in combination with turbulence promoters such as ribs: in this case the relative position of the turbulators to the holes, the rib height-to-hole diameter ratio and the increase of heat transfer surface play a major role, as highlighted by Taslim et al. (2003) and Rhee et al. (2004).

### 1.3.3 – Complex internal cooling schemes

In the first decades of experimental research in turbine internal cooling, mainly simplified geometries have been considered, both for the relative technical simplicity and for the desire of acquiring widely applicable information. However, as designers explore new strategies for achieving efficient cooling with minimum coolant flow rates, more complex architectures have gained consideration. At the same time, advances in experimental techniques have allowed the investigation of models that closely resembles the sophisticated configurations employed in today's turbine airfoils. Acharya et al. (2010) recently reviewed the influence of real-life cooling channels features, as the sudden turning and/or contraction at the entrance of the cavity, and discussed the performance of innovative architectures as the lattice structure. Bunker (2004) studied the heat transfer enhancement and pressure losses in a rectangular matrix structure of orthogonal ribs. Poser et al. (2008) obtained detailed heat transfer coefficient distributions on a complex serpentine cooling circuit. Hoefler et al. (2010) investigated an impingement cooling configuration in a trapezoidal channel with ribs on the target surfaces and bleed holes on the fourth wall. Segura and Acharya (2010) studied the swirl-induced thermal enhancement in a channel with a double helix trip strip.

### 1.3.4 – Internal cooling in trailing edge channels

The trailing edge is often a life-limiting part of the blade. The efficient cooling of this area represents an especially challenging task, since the aerodynamic requirement of high slenderness is conflicting with the need of integrating internal cooling cavities. Taslim et al. (1995) considered the influence of Reynolds number and geometrical parameters in a trapezoidal channel with tapered ribs and bleed holes. The ribbed trailing edge cavity of Kiml et al. (2001) was instead rectangular, and the authors evaluated the effect of the ribs angle. The aero-thermal performance of various means of ejecting the coolant along the trailing edge is reported, as e.g. by Martini et al. (2006) on a pressure side cut-back, and by Fiala et al. (2010) comparing a letterbox and a gill slot geometry. Gillespie et al. (2000) and Saha et al. (2008) measured the

heat transfer coefficients in a lattice structure in a trapezoidal trailing edge scheme. Cunha et al. (2006) presented analytical models for representative trailing edge configurations and compared their performances.

To the author's best knowledge, the only case resembling the geometry investigated in the present thesis (and in the publications related to it) was presented by Taslim et al (1998). With respect to the present contribution, Taslim et al. (1998) evaluated the effect of varying the Reynolds number, but did not perform any flow field analysis, neither did they attempt to measure heat transfer levels on the ribs' surface.

### 1.3.5 – Studies of coupled flow field and heat transfer

Relatively few studies present a direct combination of flow measurements and heat transfer distributions in the same channel configuration. This lack is regrettable, as any insight on the origin and impact of the fluid motion in the cooling cavities is greatly helpful to the designer. Furthermore, wide and trustworthy experimental databases reporting the velocity fields are necessary to assess the reliability of CFD codes in predicting the complicated internal cooling flow patterns. As pointed out by Iacovides and Launder (2007), detailed aerodynamic information is instrumental in distinguishing whether the modelization is faithfully capturing the phenomenon, or whether acceptably predicted thermal levels derive from misestimations compensating each others.

The complex features of the flow in ribbed channels and its influence on the heat transfer was highlighted by Rau et al. (1998), Liou et al. (1998) and Iacovides et al. (2001) using laser Doppler velocimetry (LDV). However, point-wise measurements techniques are unable to identify instantaneous flow structures and velocity gradients. Particle image velocimetry (PIV) on the other hand provides full field information. Using standard PIV two-dimensional velocity fields were obtained by Son et al. (2002) in a two-pass ribbed channel and by Casarsa et al. (2005) in a single pass ribbed channel. By means of stereoscopic PIV Chanteloup et al. (2002) obtained three-components velocity fields in a two-pass channel. Those studies revealed the highly three-dimensional nature of the flow fields and the crucial effects of large vortical structures on the heat transfer.

Similarly to rib-roughened channels cooling, also in jet impingement cooling the characterization and understanding of the aerodynamic features is fundamental for the interpretation of heat transfer data and for developing more effective schemes. O'Donovan and Murray (2007) correlated the mean and fluctuating velocity field of a single jet impingement obtained by LDV with the time-averaged and root-mean-square heat transfer rates on the target surface. Arrays of jets where investigated using PIV by Dano et al. (2005), who looked at the influence of the nozzle shape, and Thibault et al. (2009), who considered the effect of crossflow.

### 1.3.6 – Effects of thermal boundary conditions and conjugate heat transfer

All the papers mentioned above, as most of the available research studies related to turbomachinery, consider artificial thermal boundary conditions imposed at the solid-fluid interface, hence neglecting the effect of wall conduction. In fact, the latter strongly affects the temperature distribution, and hence the heat transfer coefficient levels. Therefore a truly realistic representation of the heat transfer phenomenon should consider the coupling of conduction and convection, which will be referred here as conjugate heat transfer (although this term can be used to indicate the coupling between any heat transfer modes).

A number of contributions on conjugate heat transfer were presented in the literature of general heat transfer, since the early works by Perelman (1961) who first formulated the problem, and Luikov et al. (1971) who provided the first analytical solution for a flat plate in convective-conductive regime. Mori et al. (1974) gave an analytical solution for the conjugate Graetz problem (heat transfer to laminar flow in a circular tube, taking the wall conduction into account). In more recent publications, the conjugate effects were investigated mostly in the field of electronics, e.g. by Fedorov and Viskanta (2000) who analyzed the conduction-convection coupling in a microchannel-based heat sink for electronic packaging applications.

In turbomachinery most of the contributions dealing with conjugate heat transfer are oriented to the numerics, as those of Heselhaus (1998) and Verstraete et al. (2010), who considered full blade geometries with simplified cooling architectures. Only few papers deal with the conjugate investigation of rib-roughened channels. Webb and Ramadhyani (1985) simulated a fully developed rib-roughened channel at different Reynolds and Prandtl numbers. Young and Vafai (1998) analyzed numerically a wall mounted obstacle in a two-dimensional flow and found that solid-to-fluid thermal conductivity ratio plays a major role. Iaccarino et al. (2002) modeled a similar problem and concluded that the heating mode is a critical factor, suggesting that the different thermal boundary conditions could actually explain the significant scatter in previous experimental studies.

Experimental investigations of conjugate heat transfer are scarce, especially in turbomachinery applications. Martiny (1999) investigated experimentally an effusion cooling plate and considered two materials of different thermal conductivity. At the von Karman Institute Fedrizzi and Arts (2004) studied a ribbed channel with angled ribs, while Agostini and Arts (2005) considered transverse ribs of high blockage ratio. In these efforts the ribbed wall was machined out stainless steel and uniform heat flux was imposed at the back-side of the wall. The heat transfer pattern was then retrieved solving the conduction equation within the ribbed domain, using as boundary conditions the temperature distribution measured on the wet surfaces by infrared thermography. Both studies found areas of negative heat flux along the lateral sides of the ribs, which is not physically sound.

This brief review has stressed the importance of achieving detailed information in cooling schemes of increasing complexities. The development of more effective design strategies progresses parallel to the quest for more sophisticated characterizations of the aero-thermal processes. Among the addressed topics, the

contribution of the turbulators to the heat transfer, the impact of the velocity fields and the effect of wall conduction are all aspects of evident importance. Nevertheless these issues do not find the due space in the technical literature, simingly because of the technical difficulty of characterizing them in laboratory experiments.

## *1.4 – Motivation and Objectives*

The present thesis aims at extending the available knowledge in the field of internal cooling, through the complete aero-thermal characterization of a particular cooling scheme, representative of a trailing edge channel in today's engine development technology. The focus is on three aspects which deserve high attention from both researchers and designers working in internal cooling field, yet often overlooked, as it emerges from the literature review above: (i) the aerodynamical details of the coolant flow, (ii) the contribution of the obstacles' surface to the heat transfer, and (iii) the effect of the conduction through the cooling channel walls. This goal is to demonstrate the high level of complexity that modern blade cooling architectures present, stressing the need for a deeper analysis, if not a rethinking of the common modelization strategies. It does not intend to add to the list of heat transfer correlations for internal cooling schemes.

The investigated cooling channel geometry is illustrated in Fig. 1.7. It is characterized by a trapezoidal cross-section, one rib-roughened wall, and slots along two opposite walls. The flow path can be summarized as follows: the air enters the inlet channel; it crosses the divider wall (mid-wall) through a first row of inclined slots, producing the so-called crossing-jets; the latter impinge on the rib-roughened wall: the jet-rib interaction results in a complex flow pattern, in which the coolant is rebounded against the opposite smooth wall; finally the air exits to the ambient through a second row of slots along the exit wall.

Such a scheme represents a combination of internal forced convection cooling and impingement cooling. An engine-representative Reynolds number equal to 67500 is defined at the entrance of the cavity (inlet section in Fig. 1.7).

A comprehensive experimental investigation is carried out on a magnified model of the channel, at a scale of 25 : 1 with respect to engine size applied to both the cavity volume and the walls thickness. The specific goals of the research are:

- identify and characterize the flow structures determinant for the heat transfer process in the studied geometry
- determine the heat transfer levels on the channel walls, including the ribs surfaces, in a purely convective regime
- qualify the aero-thermal effect of the rib insertion, with respect to a configuration without turbulators

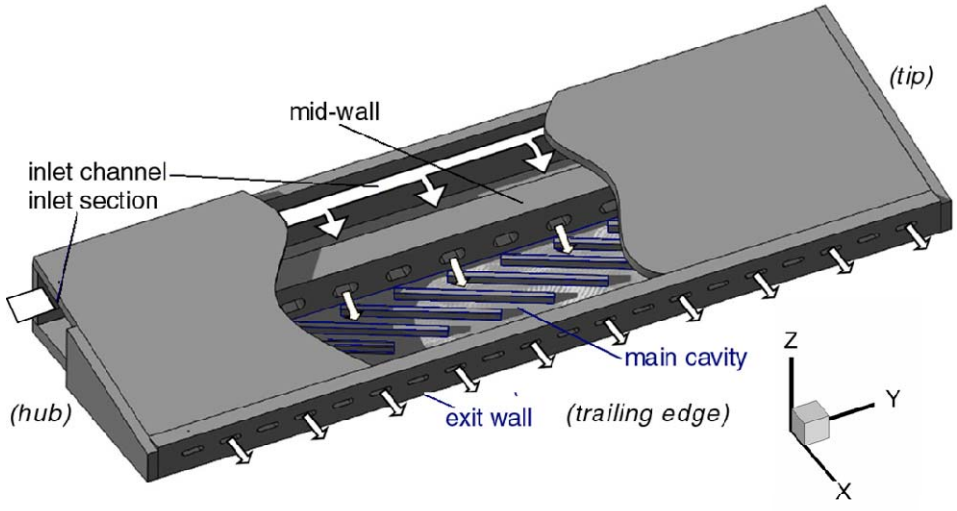


**Fig. 1.7 Test section: nomenclature and coordinate system**

- qualify the effect of varying geometrical parameters, as the relative rib-jet position and the shape of the ribs, in a purely convective regime
- compare the heat transfer levels on the ribbed wall in a conjugate heat transfer regime with those attained in a purely convective regime

The originality of the present contribution, with respect to most published reports in the field of internal cooling, stems from:

- the complex, non-academic features of the investigated cooling scheme
- the detailed analysis of the flow structures correlated to the thermal features
- the highly-resolved heat transfer distributions obtained on the surface of the turbulence promoters
- the evaluation of the wall conduction effect on the heat transfer coefficient and on the resulting wall temperature levels

## *1.5 – Outline*

The convective heat transfer problem and the conjugate heat transfer problem in internal flows are assessed in the next Chapter 2. The fundamental parameters are derived by means of dimensional analysis, stressing the consequences of including the wall conduction in the domain of interest.

The experimental set-up is presented in Chapter 3. The investigated cooling geometry, referred to as standard ribbed geometry, is described, together with three

modified geometries in which the ribs are shifted and/or tapered. The operating conditions are defined.

Chapter 4 presents a detailed description of the applied experimental procedures, mainly particle image velocimetry, liquid crystals thermography, and infrared thermography (the latter coupled with finite element analysis). The techniques are briefly outlined, while attention is drawn on the specific implementation, on the measurements details and on the data processing.

Chapter 5 is devoted to the outcome of the aerodynamic investigation: the pressure drop across the test section and the influence of the rib insertion is assessed. As for the flow field, the three-dimensional flow field in the rib-roughened geometry is reconstructed from detailed two-dimensional velocity fields. Qualitative mean flow models are deduced from flow visualizations for the configuration without ribs and for the three modified ribbed geometries.

In Chapter 6 the heat transfer performance in purely convective regime is characterized by means of spatially resolved Nusselt number distributions. These are obtained on the wall where the impingements take place and on the opposite smooth wall, both for the rib-roughened configurations and for the one without ribs (which stands as term of comparison).

In Chapter 7 the heat transfer performance in conjugate regime is assessed for the standard rib-roughened geometry. Distributions of non-dimensional wall temperature and Nusselt number along the rib-roughened wall are obtained for three wall materials of different thermal conductivity. Heat transfer data obtained on the surface of the turbulators allow to evaluate the rib performance.

The major conclusions are summarized in Chapter 8, comparing the achieved goals with the initial objectives. Recommendations for further work are also given.

Appendix A contains the analysis of the main sources of uncertainty for the reported quantities. A list of the publications this thesis has led to so far is given in Appendix B.

# Chapter 2 – Convective and conjugate heat transfer in internal flows

In a convective problem the heat transfer levels depend not only on the velocity field and on the fluid properties, but also on the thermal boundary conditions (Kays et al. (2004), Dorfman (2009). When the conduction through the wall is not negligible, the conductive and convective heat transfer modes are fully coupled: the convective fluid motion will affect the heat extraction from the wall, hence influencing the conduction pattern; in turn, the conduction through the wall will influence the wall temperature distribution, hence the convective heat transfer coefficient. This coupling of heat transfer modes is referred to as conjugate heat transfer. The key parameter is the temperature distribution at the solid-fluid interface: indeed, the properties of a conjugate problem are the same as those of a convective problem where an identical temperature field is imposed along the wall surface (Dorfman (2009)).

When devising and investigating a model of a real internal cooling channel (by numerics or by experiments) the reproduced thermal boundary conditions should resemble the engine environment. If this is not the case, the modelization of the heat transfer process can be inaccurate in the first place. In most of the available studies in the field, the thermal boundary conditions are clearly not realistic: either the temperature (Dirichlet boundary condition) or the heat flux (Neumann boundary condition), or the heat transfer coefficient (Robin boundary condition) are specified at the solid-fluid interface. In a real cooled airfoil, of course, none of them are respected: the only constraint is the interface continuity of temperature and heat flux, as it results from the coupled convective and conductive heat transfer modes. The latter is referred to as conjugate (or fourth type) thermal boundary condition.

In the reports that investigate cooling channels schemes using simplified boundary conditions it is assumed (most often implicitly) that the influence of the thermal boundary conditions is negligible. This is sometimes a fair assumption: for example the Nusselt number for fully developed pipe flow with uniform heat flux at the wall differs by less than 3% from the case with isothermal wall (Kays et al. (2004)) for air. However, for situations with large spatial thermal gradients and/or geometrical asperities, the impact of the wall temperature distribution can be much greater. Such situations are common in internal blade cooling, since large use is made of jet impingements, turbulators and bleeding holes. In the numerical study of Heselhaus (1998) of a film cooled blade a computation with adiabatic condition at the wall was compared with a conjugate calculation: the local heat transfer levels were shown to differ by more than 50%, the results of the conjugate calculation being in far better agreement with the measured temperature values. Iaccarino et al. (2002) also demonstrated the strong impact of thermal boundary conditions on the heat transfer coefficient in the vicinity of a square rib.

The problem of describing the heat transfer process in blade cooling channels is tackled in the present chapter. In order to obtain useful information from a model simulating a real cooling channel, an invariant descriptor of the heat transfer process must be available, i.e. the measured descriptor should be transportable from the investigated model to the reality, in any geometrically similar situation. Dimensional analysis is used here to derive the appropriate descriptors of the process, both in the purely convective and in the conjugate heat transfer mode. For a description of the method of dimensional analysis and its applications in fluid mechanics, the reader is referred to Weigand and Simon (2006).

## *2.1 – Dimensional analysis: the Buckingham Pi Theorem*

The idea at the basis of the dimensional analysis is to exploit the dimensional consistency of physical equations in order to group variables together into dimensionless parameters. If all these parameters are set to be constant, full similarity between two processes is obtained. This method presents two appealing advantages:

- the dimensionless parameters are less numerous than the original variables
- results obtained in terms of dimensionless parameters are applicable to any similar phenomena (e.g. in configurations of different scales)

The first aspect can be exploited to reduce the effort for solving the governing equations of the problem, as the number of variables is reduced. The second aspect allows to design meaningful experiments and to properly scale the test results to the original configuration (in the present case the real blade cooling channel).

Maybe the most relevant result of dimensional analysis is the Buckingham Pi Theorem, formulated by Buckingham (1914), who gave a solid theoretical basis to the "method of dimensions" of Rayleigh. Let us consider a problem which can be described by the behavior of $n$ physical variables $p_j$. In mathematical terms, such problem can be characterized by a relation of the form:

$$f(p_1,...,p_n) = 0 \tag{2.1}$$

The dimension of the physical variables can be expressed by the product of $m$ basic units $X_i$ (e.g. length, mass, time, etc.), powered by some exponent $a_{ij}$.

$$\left[p_j\right] = \prod_{i=1}^{m} X_i^{aij} \tag{2.2}$$

Since the choice of the units used does not influence the physical process, Eq. 2.1 can be reduced to a relation between $d$ independent dimensionless quantities:

$$f(\Pi_1,...,\Pi_d) = 0 \tag{2.3}$$

where $\Pi_j$ are the so called dimensionless groups, obtained as products of the physical quantities. The Buckingham Pi Theorem states that the number of independent dimensionless groups is:

$$d = n - r \tag{2.4}$$

where $r$ is the rank of the dimension matrix $a_{ij}$. If the fundamental units are independent (as it is typically the case), $r$ coincides with $m$.

## *2.2 – Convective heat transfer in internal flows*

Let us consider the system displayed in Fig. 2.1, where a purely convective heat transfer process takes place in a cooling channel. The convective regime is assumed to be forced, i.e. buoyancy forces driven by density differences are negligibly small respect to inertia forces. This is usually verified for non-rotating cooling channels, as the one considered in the present research. Time-dependence is also neglected, as gas turbine internal cooling channel processes are considered steady (in the time-average sense). The physical process can be described by a relation of the form:

$$f(D,u,\rho,\mu,c_P,k_f,\theta,h) = 0 \tag{2.5}$$

where the physical variables which appear to play a role are respectively: geometrical length scale, velocity, density, dynamic viscosity, specific heat capacity and thermal conductivity of the fluid, temperature head, and heat transfer coefficient. The temperature head is the difference between the wall temperature $T_w$ and a reference fluid temperature $T_f$:

$$\theta = T_w - T_f \tag{2.6}$$

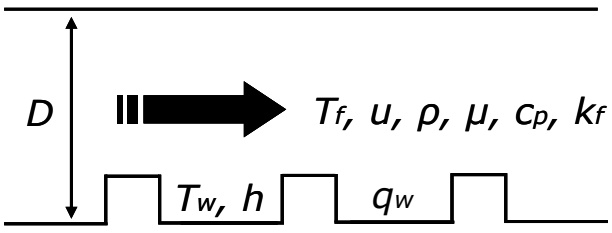


**Fig. 2.1** **Major physical variables in purely convective heat transfer in internal flow**

Among possible descriptors of heat transfer in internal flows, the heat transfer coefficient is the most common choice, and is defined by the Newton's law:

$$h = \frac{q_w}{\theta} \tag{2.7}$$

where $q_w$ is the wall-normal heat flux. The classic heat transfer coefficient definition is fully appropriate only for situations where a uniform wall temperature is imposed at the solid-fluid interface; abrupt changes of the thermal boundary condition may force the heat transfer coefficient to $\pm\infty$ (Kays et al. (2004)). The definition of the heat transfer coefficient can be made independent from the thermal boundary conditions using the adiabatic wall temperature $T_{aw}$ as reference flow temperature, as reviewed by Moffat (1998). However, $T_{aw}$ is also dependent on the thermal boundary conditions, and needs to be evaluated for each case. This is particularly cumbersome: either the heat transfer surface has to be covered with independent heaters (as in Anderson and Moffat (1992)), or multiple transient tests have to be performed to extrapolate $T_{aw}$ (as in Chambers et al. (2003)). In the present case we choose the reference fluid temperature as the inlet temperature; therefore the heat transfer coefficient is inherently dependent on the thermal boundary conditions, namely on the temperature distribution along the streamlined wall. In the present cooling scheme this choice of the reference fluid temperature is primarily dictated by practical reasons. However, it will be helpful for stressing the advantages of the conjugate approach.

In convective heat transfer, four fundamentals units are to be considered: mass, length, time and temperature. Given the eight physical variables in Eq. (2.5), according to the Buckingham Pi Theorem, the problem can be described by the behavior of four non-dimensional groups. By means of the recurring sets method and a proper choice of the variables, the following non-dimensional groups are derived:

$$Re = \frac{\rho u D}{\mu} = \frac{\text{inertia forces}}{\text{viscous forces}} \tag{2.8}$$

$$Pr = \frac{\mu c_P}{k_f} = \frac{\text{viscous diffusion}}{\text{thermal diffusion}} \tag{2.9}$$

$$Ec = \frac{u^2}{c_P \theta} = \frac{\text{kinetic energy}}{\text{flow enthalpy}} \tag{2.10}$$

$$Nu = \frac{hD}{k_f} = \frac{\text{conductive resistance}}{\text{convective resistance}} \tag{2.11}$$

which are respectively: the Reynolds number, the Prandtl number, the Eckert number, and the Nusselt number. The Eckert number is a measure of the viscous dissipation in the flow, and can therefore be neglected in the present application because of the moderate velocity levels (in the model as well as in reality). Therefore Eq. (2.5) has a dimensionless equivalent in the following relation:

$$f(Re, Pr, Nu) = 0 \tag{2.12}$$

which can be made explicit for the Nusselt number:

$$Nu = Nu\,(Re, Pr) \tag{2.13}$$

Hence, in experimental investigations, distributions of Nusselt number measured on a magnified model at different temperature levels will hold in a similar internal cooling cavity at engine conditions, provided that *Re* and *Pr* are kept constant between engine conditions and laboratory environment. *Pr* is essentially a property of the fluid, which in the present case is air as in most engine applications; *Re* has to be fixed equal to engine-representative values (typically by adjusting the flow velocity).

It should be noticed that different choices in grouping the variables would lead to different (and equally valid) dimensionless groups. The presented analysis yields results similar to what is presented in classic fluid mechanics textbooks as Schlichting (1979).

## *2.3 – Conjugate heat transfer in internal flows*

Let us now consider the forced convective, steady heat transfer process sketched in Fig. 2.2. With respect to the preceding case, the conduction in the wall of finite thickness is taken into account. The heat is supplied to the wall as a uniform heat flux imposed at its outer side. No constraint is forced at the solid-fluid interface, except thermal equilibrium and heat flux continuity (fourth type thermal boundary condition). The relation describing the process this time can be written as:

$$f\,(D, u, \rho, \mu\, c_P, k_f, \theta, q_0, k_w, d) = 0 \tag{2.14}$$

$k_w$ is the wall thermal conductivity and $q_0$ is the imposed heat flux level. In the first place one can avoid defining the heat transfer coefficient $h$: if $q_0$ is included in the set of variables, $h$ is redundant as $q_w$ is linked in deterministic manner to $q_0$: the heat flux at the wall is univocally determined once the velocity field, the wall temperature head and $q_0$ are fixed. $d$ is the characteristic thickness of the wall. In the present investigation the channel volume and the wall thickness are scaled with the same ratio; one length scale is therefore sufficient. The application of Buckingham Theorem leads to the following dimensionless version of Eq. 2.14:

$$f(Re, Pr, \Theta, K) = 0 \tag{2.15}$$

where two non-dimensional groups are introduced: the non-dimensional wall temperature $\Theta$ and the solid-to-fluid thermal conductivity ratio $K$, defined as follows:

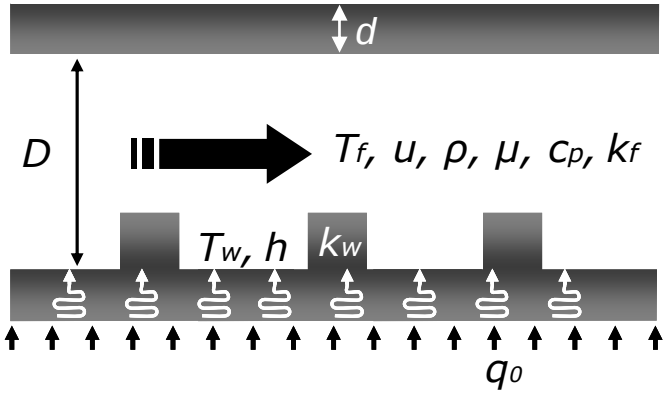


**Fig. 2.2 Major physical variables in conjugate heat transfer in internal flow**

$$\Theta = \frac{k_f \theta}{q_0 D} \tag{2.16}$$

$$K = \frac{k_w}{k_f} \tag{2.17}$$

Equation 2.15 can be made explicit for Θ:

$$\Theta = \Theta\,(Re, Pr, K) \tag{2.18}$$

Hence, distributions of non-dimensional wall temperature measured on a magnified model at different temperature levels will hold in a similar internal cooling cavity at engine conditions, provided that, besides *Re* and *Pr*, also *K* is kept constant between engine conditions and laboratory environment. Here the conjugate nature of the phenomenon, and the particular wall temperature distribution entailed by the heat transfer process, is included in the modelization; therefore the applied thermal boundary condition is inherently correct (provided that a uniform heat flux condition at the outer side of the wall is a realistic representation of the engine reality over the considered blade span).

A similar reasoning can be followed if the heat transfer coefficient is defined; in this case $q_0$ is redundant. The dimensional analysis results then in a group of dimensional parameters where *Nu* substitutes Θ:

$$Nu = Nu\,(Re, Pr, K) \tag{2.19}$$

The result of the present dimensional analysis is similar to what is summarized for conjugate heat transfer by Shah and London (1978), who instead uses the Peclet number (which is equal to *RePr*).

If one considers two different length scales for the solid and the fluid, the Biot number is added to the set of parameters above:

$$Bi = \frac{hd}{k_w} = \frac{\text{conductive resistance of wall}}{\text{convective resistance}} \tag{2.20}$$

where $d$ is the thickness of the wall. The value of the Biot number is often used as a criterion to assess if a conjugate heat transfer problem can be approximated as purely convective. In the present case (trailing edge cooling channel with different wall conductivities) the average Biot number ranges between 0.1 and 1.7, with a value of about 0.2 for the engine-like case; this means that neither the thermal resistances of the body nor the one of the fluid are negligible: therefore it can be foreseen (and the results will confirm) that the conjugate effect will be significant.

As one can see, both $\Theta$ and $Nu$ are transportable from laboratory experiments to the engine environment, provided the levels of $Re$, $Pr$ and $K$ are respected. Since in the present situation a reference fluid temperature is assumed, the non-dimensional temperature contains only one unknown quantity, the wall temperature. In this sense, as pointed out by Faghri and Sparrow (1980), the Nusselt number is a less convenient parameter to describe conjugate heat transfer, since it expresses the ratio of two unknowns, heat flux and wall temperature head. When measured, both groups can be used to validate conjugate heat transfer calculations. However, to retrieve $Nu$ from temperature measurements one needs to solve the conduction through the wall (direct measurement of temperature and heat flux at the same location is usually not a viable solution). On the other hand, wall temperature measurements are sufficient to evaluate $\Theta$. Nevertheless, solving the conduction through the wall may provide important insights on the heat transfer process, as the heat flow pattern within the solid becomes available. Finally, when comparing results from the conjugate mode with purely convective quantities for the same configuration, as it will be done in the present study, the use of the Nusselt number (almost universally adopted in literature) is certainly convenient. In the present research, both $\Theta$ and $Nu$ are obtained for the conjugate heat transfer configuration, as they provide different but equally interesting insights.

An observation is to be made: considering the operative temperatures and the conductivity of modern blading materials (nickel or cobalt-based super-alloys), materials with conductivity about 10 $Wm^{-1}K^{-1}$ at ambient temperature should be employed for the wall in order to properly match $K$ in the laboratory. Ni-based super-alloys used for blading, like Nimonic and Inconel, are among the few machinable materials that fit this requirement. Indeed, thermal conductivities of those super-alloys have temperature dependence similar to the one of air: in both cases the thermal conductivity increases of a factor 2.6 for a temperature raise of 1000 K. This circumstance leads to the following appealing conclusion: if a real engine component is used to perform conjugate heat transfer investigations at a temperature level different from the real operating conditions, the conductivity ratio is naturally matched. The weak temperature dependence of $K$ for Nimonic-air coupling is illustrated in Fig. 2.3. The abscissa refers to the metal temperature, while the air

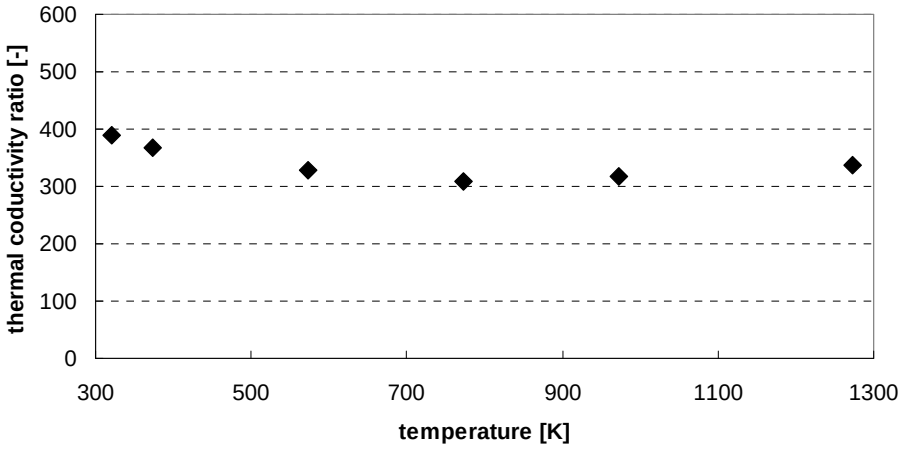


**Fig. 2.3** **Temperature dependence of thermal conductivity ratio for Nimonic-air coupling**

temperature at which the conductivity is evaluated derives from assuming a coolant-to-metal temperature ratio of 0.85. The temperature ratio is higher than the classic values of about 0.7, but it is considered more representative of the present trailing edge channel, where the coolant has warmed up in (at least) one preceding cavity before entering the investigated one. The values of thermal conductivity for Nimonic (grade 105) are taken from Kaye and Laby (1995).

# Chapter 3 – Experimental-apparatus

An open loop test facility was designed and constructed in order to perform the investigation reported in this thesis. The test stand is presented in the next section, followed by a description of the set-up. The operating conditions are summarized.

## *3.1 – Test section*

The measurement campaign is conducted on a large scale model reproducing a trailing edge cooling channel representative of a modern engine turbine blade at a scale of about 25 : 1 (Fig. 3.1). The channel is machined mainly out of Plexiglas: it is

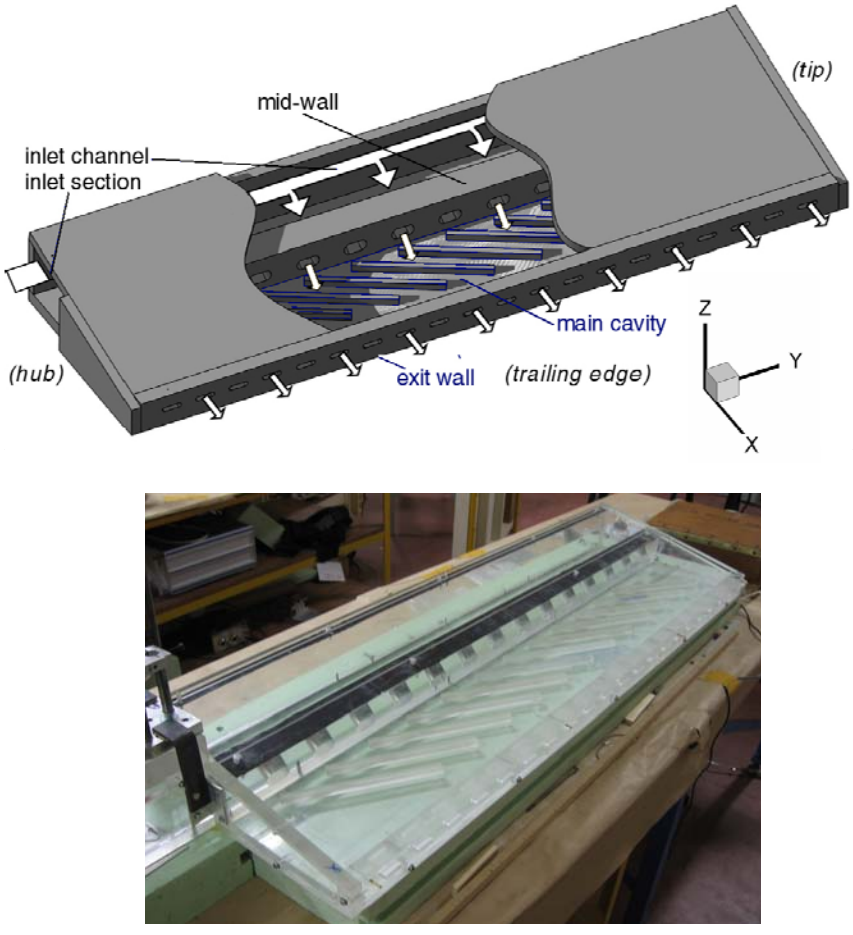


**Fig. 3.1** **Test section: nomenclature and coordinate system (up) and picture (down)**

1130 mm long, 340 mm wide, and has a maximum height of 108 mm. It consists of two parallel trapezoidal cavities: one, the inlet channel, simulates the passage before the trailing edge and has a hydraulic diameter $D_{inlet}$ = 81.4 mm; the other is the actual object of the present investigation: a trapezoidal cavity of low aspect ratio representing the trailing edge cavity. The two passages are separated by a perforated wall (mid-wall) provided with 14 racetrack-shaped slots (named mid-wall slots, hydraulic diameter $D_{mid}$ = 21.9 mm). The axes of the mid-wall slots are sloped down with an angle of 27° with respect to the *xy* plane (Fig. 3.2). The length of the mid-wall slots is about twice their hydraulic diameter.

The wall towards which the mid-wall slots are inclined (also called impingement wall) is equipped with square section ribs, one in front of every slot (Fig. 3.3). They are spaced with a pitch of 7.5*e*, *e* being the rib height, and are inclined at an angle of 30 degrees with respect to the *y*-direction. Due to the trapezoidal cross section, the blockage ratio (rib height/channel height) increases with the *x*-coordinate; it is 0.3 at halfway between mid-wall and exit wall.

In the standard rib-roughened configuration, on which the present study is mainly focused, the ribs' edges are aligned with the slots' edges (Fig. 3.3, left). In the following, unless differently specified, the referred rib-roughened configuration will be the standard one. The effect of varying the rib-slot alignment and the rib shape are investigated in three modified configurations.

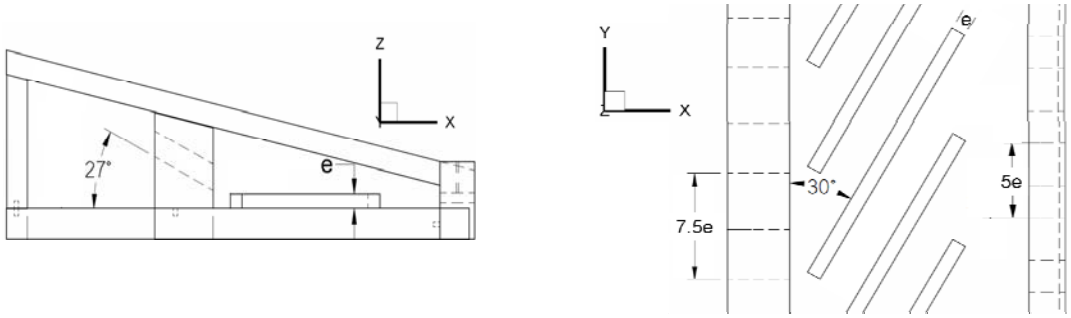


**Fig. 3.2** **Side view of the channel (left) and top view of the ribbed wall (right)**

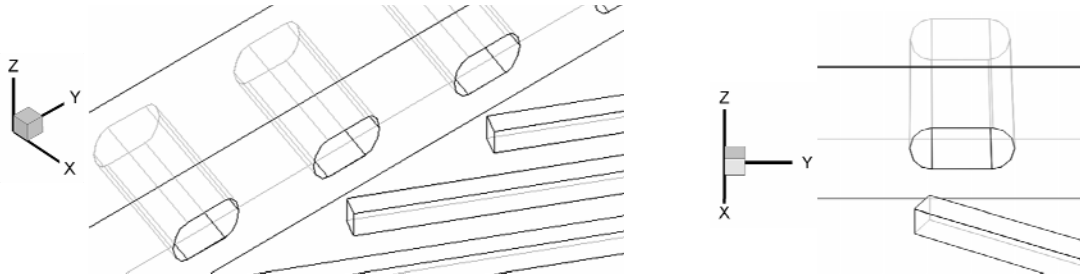


**Fig. 3.3** **Mid-wall slots: slot-rib periodicity (left) and rib-slot alignment (right) in the standard rib-roughened configuration**

All the Plexiglas plates from which the channel is built are 15 mm thick, except for the mid-wall (42.5 mm) and the exit wall (25 mm). The different parts of the channel are hermetically connected to each other, to avoid any leakage to the ambient.

The exit wall is provided with 20 slots of hydraulic diameter $D_{exit}$ = 11.7 mm, aligned with the $x$-axis. Their length is about twice their hydraulic diameter. They present a spacing of about 5$e$, hence they do not follow the periodicity of the inlet slots.

Static pressure taps of 1.5 mm diameter are drilled in each mid-wall slot and exit slot. All the holes are drilled at right angle with the internal surfaces, at halfway between inlet and outlet of each slot.

The smooth wall, opposite to the rib-roughened one, is available in four different versions depending on the applied measurement technique:

- one Plexiglas wall equipped with holes in correspondence of the pressure taps of the mid-wall slots, plus four equally spaced taps at halfway between mid-wall and exit wall
- one wall in scratch-proof glass, for performing PIV and liquid crystal thermography on the ribbed wall
- one wall in Plexiglas equipped with a heating foil and painted with liquid crystals, for performing liquid crystals thermography on the smooth wall itself
- one wall in Plexiglas with a large opening on the central part, in order to insert an optical window for performing infrared thermography

The central part of the rib-roughened wall (5 ribbed domains, from the 5$^{th}$ to the 9$^{th}$) is interchangeable, and six versions are available:

- one wall in Plexiglas, on top of which Plexiglas ribs are glued, to perform liquid crystals thermography on the floor between the obstacles
- one wall in Plexiglas, with a slot to insert a rib made of highly insulating material wrapped in a heating foil, to perform liquid crystals thermography on the rib surface
- one wall identical to the latter, but with the slot in a different position, to study the effect of changing the rib-to-slot relative position
- one ribbed wall machined in one piece of stainless steel (AISI 304), to study conjugate heat transfer at high values of solid-to-fluid conductivity ratio
- one ribbed wall machined in one piece of nickel-based alloy (Inconel 625), to study conjugate heat transfer at engine-representative values of solid-to-fluid conductivity ratio

- one ribbed wall machined in one piece of ceramoplastic (Mykroy-Mycalex), to study conjugate heat transfer at low values of solid-to-fluid conductivity ratio

The values of thermal conductivity for the material used to investigate conjugate heat transfer are listed in Tab. 3.1

Figure 3.4 displays the interchangeable part of the ribbed wall for investigating conjugate heat transfer, which comprises five adjacent ribbed domains. The wall thickness excluding the turbulators is 1.5*e*, also representative of a real blade wall. Each one of the three walls of different conductive materials is instrumented with 4 K-type thermocouples inserted from the back side up to 0.5 mm from the wet surface. The location of the thermocouples is shown in Fig. 3.4 (numbers from 1 to 4): they are inserted at location far enough from the studied domain (central rib), not to alter the conduction through the investigated portion of the wall.

As for the shape and position of the obstacles, besides the standard configuration, three additional configurations are considered: one results from a *y*-direction shift of the ribs equal to half of the mid-wall slots pitch; one results from tapering the ribs with an angle of 2.3°, which leads to a rib height of 2 mm at the downstream edge (i.e. 0.2*e*, where *e* is the height of the obstacle at the upstream edge, see Fig. 3.5); the last one results from the combination of shifting and tapering the ribs. In the subsections where

| Material | Grade | $k$ [$Wm^{-1}K^{-1}$] @ 300 K |
|---|---|---|
| Stainless steel | AISI 304 | 18.5 |
| Inconel | 625 | 9.8 |
| Ceramoplastic | Mykroy-Mycalex | 1.15 |

**Tab. 3.1** **Thermal conductivity of the materials used for the ribbed wall in conjugate heat transfer regime**

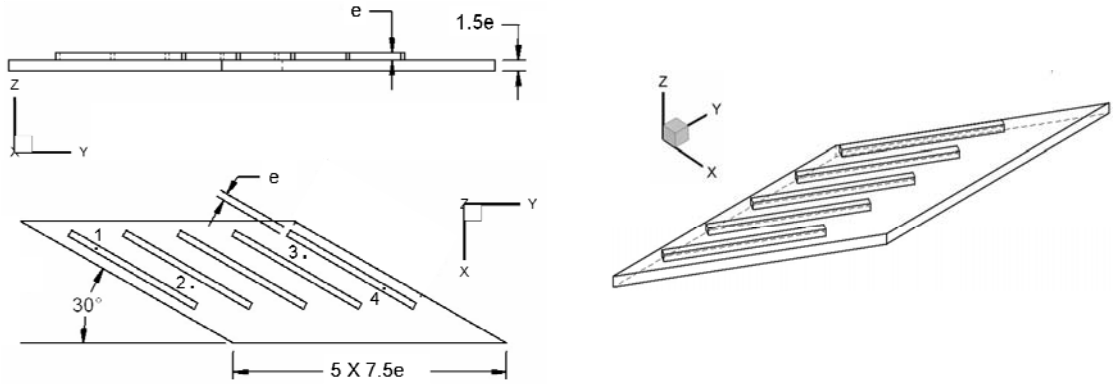


**Fig. 3.4** **Slab to insert in the central part of the ribbed wall for investigating conjugate heat transfer**

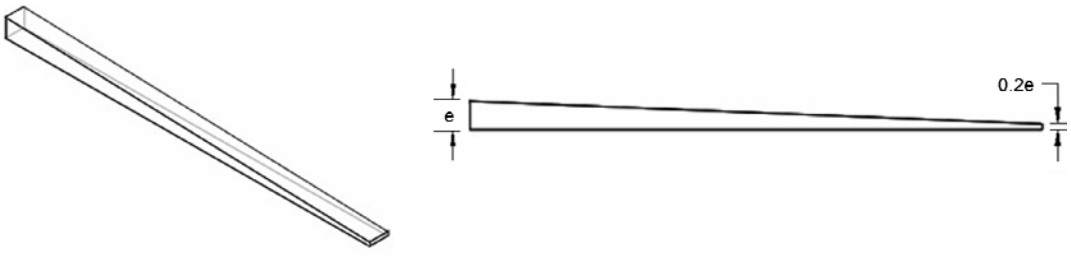


**Fig. 3.5** **Isometric view (left) and side view (right) of the tapered rib**

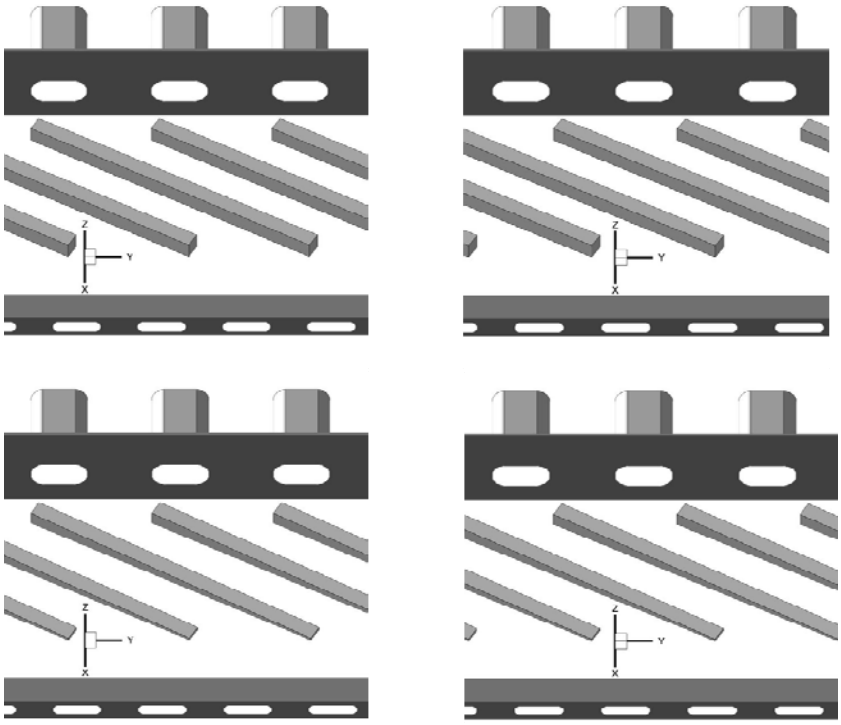

**Fig. 3.6** **Rib geometries: configuration *G1* (top left), *G2* (top right), *G3* (bottom left) and *G4* (bottom right).**

the modified geometries are examined they will be addressed as *G2* (shifted ribs), *G3* (tapered ribs) and *G4* (shifted and tapered ribs), with *G1* referring to the standard geometry. The four configurations are displayed in Fig. 3.6.

## *3.2 – Experimental installation*

The experimental set-up is sketched in Fig. 3.7. The air flow is regulated by a 2.2 kW centrifugal blower, which discharges through a 9 kW heat exchanger and then into a settling chamber. The latter is connected to the test section via an 1100 mm long

channel, which is actually a prolongation of the inlet channel of the test section. A honeycomb within the settling chamber helps reducing the swirl of the flow generated by the blower. For the heat transfer measurements, a 2.4 kW DC power supply is employed to dissipate current through heating foils of Inconel 600 attached to the investigated channel wall.

A remark is worth making about the chosen air flow system. Unlike most facilities of the same type, which function in suction mode, the present one works in pressure mode: the blower is placed upstream of the test section, thus the air flow is at higher static pressure than the ambient. Suction mode facilities normally produce more regular entrance conditions, as the inlet flow does not present the swirl and high turbulence level caused by the blower. In the present case though, working in suction mode would have required the insertion of a plenum downstream the exit wall: given the geometrical configuration, this would have make impractical to probe the 20 exit slots, which is done traversing a Prandtl tube and a thermocouple. However, the settling chamber, the honeycomb and the inlet channel guarantee good flow quality at the inlet section (Fig. 3.8): the inlet velocity profile displays a high degree of symmetry, and hot wire measurements performed in similar facilities in VKI laboratories using the same components show turbulence intensity levels around 1.5% in the bulk flow and up to 10% in the boundary layer.

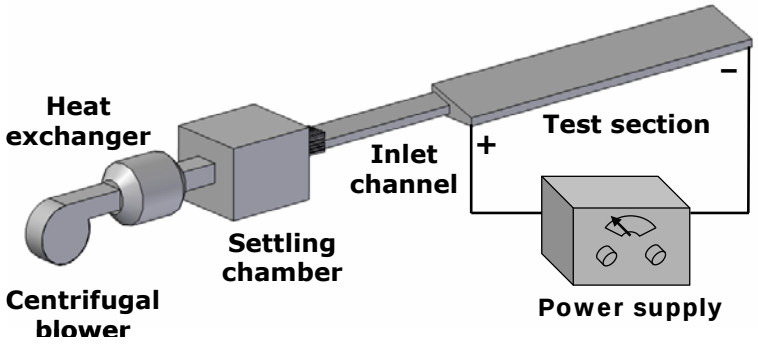


**Fig. 3.7** **Sketch of the experimental installation**

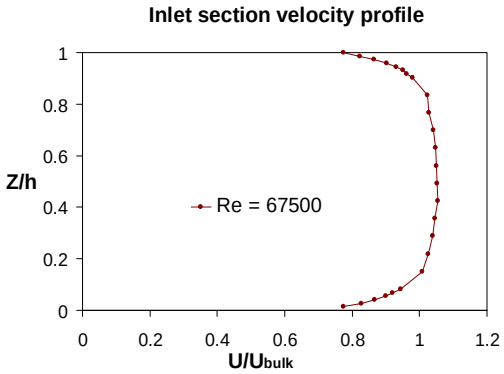


**Fig. 3.8** **Inlet velocity profile for the present study**

## *3.3 – Operating conditions*

The operating conditions are monitored at the inlet section by static pressure taps, a traversing Pitot probe (diameter 1.5 mm) and one K-type thermocouple inserted in a Monel tube (diameter 1.2 mm). The inlet velocity profile is characterized traversing the Pitot probe along the cross-section in two perpendicular axes, both passing through the center of the inlet section. All experiments are conducted at a fixed Reynolds number equal to *Re* = 67500, representative of today's engine development technology. The Reynolds number is based on the inlet section hydraulic diameter, bulk flow velocity and local air properties:

$$\mathrm{Re} = \frac{\rho U_b D_{inlet}}{\mu} \tag{3.1}$$

$U_b$ is the bulk velocity, $\rho$ the density and $\mu$ the dynamic viscosity of the coolant air at the inlet section. *Re* is adjusted by tuning the blower; this operation is based on the total pressure observed with the Pitot tube placed at the inlet section centerline, which is related to the bulk velocity. Such relation is computed evaluating the shape of the velocity profile by means of the two perpendicular traverses, and hence computing the ratio between the maximum (centerline) velocity and the bulk (section-averaged) velocity. The best estimation of the inlet Reynolds number uncertainty is ±2% based on a 95% confidence interval. In order to check pressure and mass flow distribution across the various slots, static pressure taps are drilled in each mid-wall and exit slot.

The average Reynolds number of the crossing jets is 18500, based on the mid-wall slots hydraulic diameter and on a bulk velocity supposed equal for each slot. The outlet conditions are quantified by means of a Prandtl probe (diameter 1.5 mm) and a K-type thermocouple inserted in a Monel tube (diameter 1.2 mm) traversing the outlet section of the exit slots. Assuming an even mass flow distribution along the row of exit slots, the outlet Reynolds number based on their hydraulic diameter is about 15100.

The geometrical periodicity of the channel in the *y*-direction allows considering the central part of the main cavity to be representative of most of the test section. Apart from side effects due to the proximity to the lateral walls, maximum variations of 4% in crossing jets static pressure and 6% in exit jets velocity are identified along the channel. This justifies the choice of concentrating the experimental effort in the central area, i.e. from the $6^{th}$ to the $8^{th}$ ribbed domain, proceeding in positive *y*-direction.

# Chapter 4 – Measurement procedures and data processing

## *4.1 – Outline of the experimental investigation*

In the present chapter consideration is given to the measurement techniques utilized to characterize the cooling geometry, from the aerodynamic as well as from the thermal standpoint.

The static pressure distribution across the channel in the various studied configurations is determined by means of static pressure taps connected to differential transducers.

A detailed flow field analysis is carried out in the rib-roughened geometry using two-dimensional particle image velocimetry. The main flow structures are identified and a mean flow model of the three-dimensional flow in the trailing edge cavity is reconstructed.

Steady state liquid crystals thermography is applied to measure the heat transfer coefficient distributions in purely convective regime along the impingement wall and on the opposite smooth wall; such analysis is carried out for the configuration without ribs, for the standard rib-roughened configuration, and for the three modified ribbed configurations.

Infrared thermography is employed to obtain non-dimensional temperature distributions and distributions on the rib-roughened wall in conjugate heat transfer regime, for three values of the thermal conductivity ratio. Coupled with a finite element analysis, the results of the thermography allow evaluating the heat transfer coefficient distributions.

A qualitative model of the flow in the cooling channel, for both the rib-roughened configurations and in the one without ribs, is obtained by means of surface-streamline flow visualizations: wool tufts, ink dots tracers and oil film techniques are applied along the walls.

The results of the application of those measurement techniques are given in Chapter 5 for the aerodynamics, Chapter 6 for the convective heat transfer, and Chapter 7 for the conjugate heat transfer.

## *4.2 – Two-dimensional particle image velocimetry*

### 4.2.1 – Principles of PIV

Particle image velocimetry (PIV) is a non-intrusive technique that allows for capturing velocity information of the whole flow fields. It belongs to the family of

methods based on imaging and analysis of flow tracers. The idea at the base of PIV is very simple: whole velocity fields are measured by taking two consecutive images of the particles following the fluid motion: the velocity is calculated from the known time difference and the measured particles displacement. The feasibility of the technique was demonstrated for the first time at the von Karman Institute (Meynart (1979)), when the method was still referred to as "laser speckle velocimetry".

Here we will refer to the standard version of the technique, in which the two components of the velocity field lying on the measurement plane are evaluated (2D-PIV). Nowadays further developments allow measuring all the three velocity components on planes (stereoscopic PIV) or volumes (holographic PIV, tomographic PIV), at the cost of additional technical complexities. Moreover, we will refer to non-time-resolved PIV, in which the instantaneous realizations are statistically independent. Details on the technique can be found, among other sources, in Raffel et al. (1998), Adrian (1991), and in several Lecture Series held at VKI (e.g. Scarano and Riethmuller (2009)).

The measurement principle is illustrated in Fig. 4.1: small tracers are added to the flow and illuminated twice by a light sheet produced by a pulsed laser. The two laser pulses are separated by a time interval (separation time), whose extension depends upon the flow velocity and dimensions of the investigated area. The light sheet is produced from the laser beam by means of dedicated optics, and its orientation contains the dominant flow direction. The light scattered by the particles is collected in an image grabber, which stores the two instantaneous frozen flow pictures in a digital form. For the processing of the recorded images, the two frames are divided into small sub-areas called interrogation windows. Assuming that all the particles within one interrogation window move homogeneously during the separation time, the most likely displacement vector is determined for each window by means of cross-correlation statistical methods, and the velocity is computed from the time interval occurring between the two frames.

The 2D cross-correlation exploited consists of the spatial convolution of the signal related to the light scattered by the tracers in a couple of PIV images: each interrogation window is cross-correlated with its correspondent in the other image of the couple. The resulting correlation map will present a peak at the location of the most likely displacement of the particles inside the window (Fig. 4.1, bottom).

From the experimental standpoint, several technical aspects of two-dimensional PIV deserve attention, as they affect the measurement accuracy and drive the choice of the experimentalist. The main parameters that need to be optimized during measurements and processing are: laser sheet thickness, separation time, magnification factor (i.e. the number of pixels resolved along a millimeter on the objective plane) and interrogation window size.

Milestones in the development of PIV include (but are not limited to) the work of Riethmuller and co-workers at VKI (e.g. Scarano and Riethmuller (2000)), Adrian and coworkers at University of Illinois (Keane and Adrian (1990)), Westerweel and Scarano at Delft Technical University (Westerweel and Scarano(2005)), Gharib and co-workers at California Institute of Technology (Willer and Gharib (1991)), Stanislas and co-workers at University of Lille (Foucaut et al. (2004)).

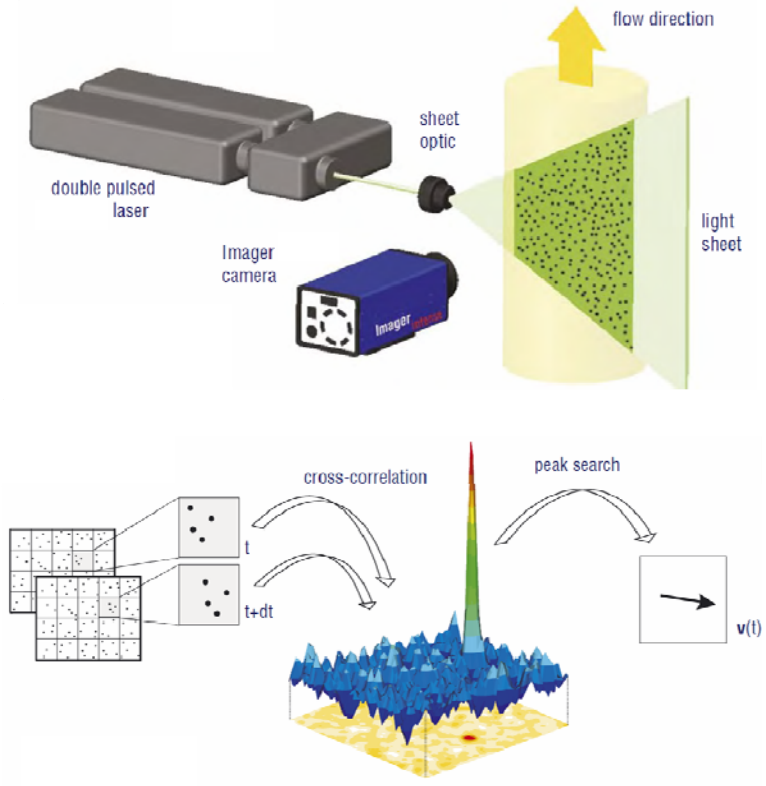


**Fig. 4.1** **Schematic of PIV working principle: measurement setup (top) and cross-correlation (bottom). (source: La Vision GmbH, http://www.piv.de)**

### 4.2.2 – Experimental apparatus for PIV

The employed 2D-PIV system comprises:

- Laser: Nd-Yag pulsed laser, 632.8 nm, 250 mJ per pulse, maximum pulse frequency of 10 Hz
- Camera: PCO SensiCam CCD, resolution of 1280 x 864 pixels, 12-bit output and minimum time interval of 200 ns
- Acquisition system provided with image grabbing software connected with the camera
- Synchronizer: it coordinates the laser pulse with the camera acquisition
- Camera objectives: one with focal length $f$ = 105 mm, and one with $f$ = 70 mm
- Laser optics: two cylindrical lenses of $f$ = -40mm and -60 mm; three spherical lenses of $f$ = -1000 mm, 600 mm, 1000 mm

- Seeding generator: designed and built in VKI, it works with vaporized oil (Global Mix Smoke Fluid, Le Maitre) and produces particles of about 2 microns in diameter (Fabry (1998))

The settings chosen for the devices and the details of the optical arrangements for each measurement plane are described in the following section.

### 4.2.3 – Measurement campaign

The PIV measurements and processing have been carried out in the frame of the Diploma Course Project of Alessandro Armellini (Armellini (2007)). PIV is performed in the central area of the test section in the standard ribbed configuration, along eight measurement planes whose position and nomenclature is illustrated in Fig. 4.2 (where the index *i* stands for the 7$^{th}$ slot and rib):

- *x'y* is a plane containing the mid-wall slot axis
- *xy1* is a plane parallel to the ribbed wall and is placed at 0.2*e* from the floor (*e* is the rib height)
- *xy2* is a plane parallel to the ribbed wall and is placed at 1.5*e* from the floor
- *x"y* is a plane parallel to the smooth inclined wall, placed at 0.3*e* from it
- *xz_core_i* is a plane perpendicular to both ribbed wall and mid-wall, and is positioned at 3/4 of the width of the mid-wall slot *i*
- *xz_core_i+1* is a plane perpendicular to both ribbed wall and mid-wall, and is positioned at 3/4 of the width of the mid-wall slot *i+1*
- *xz_mid_i_i+1* is a plane perpendicular to both ribbed wall and mid-wall, and is positioned in between of slots *i* and *i+1*
- *xz_mid_i+1_i+2* is a plane perpendicular to both ribbed wall and mid-wall, and is positioned in between of slots *i+1* and *i+2*

Apart from planes *xz_core_i+1* and *xz_mid_i+1_i+2*, which mainly serve for verification of the flow periodicity, all the investigated planes result from the juxtaposition of multiple windows. In total, the campaign includes twenty two different PIV windows. The choice of the measurements settings has been carefully optimized; given the complexity of the flow, this has been an especially challenging task.

The laser sheet thickness is kept in the typical range of 1 to 1.5 mm, except for the portion of plane *x'y* outside the jet, where a thicker sheet is used (2 mm) in order to reduce out-of-plane particles loss in a region of highly three-dimensional flow.

For all planes, with the exception of *x"y*, a 105 mm objective is used, and a magnification factor of 25 to 29 pixel/mm is obtained. This corresponds to a field of view of about 50 x 35 mm$^2$. For plane *x"y*, on the other hand, a shorter focal length of

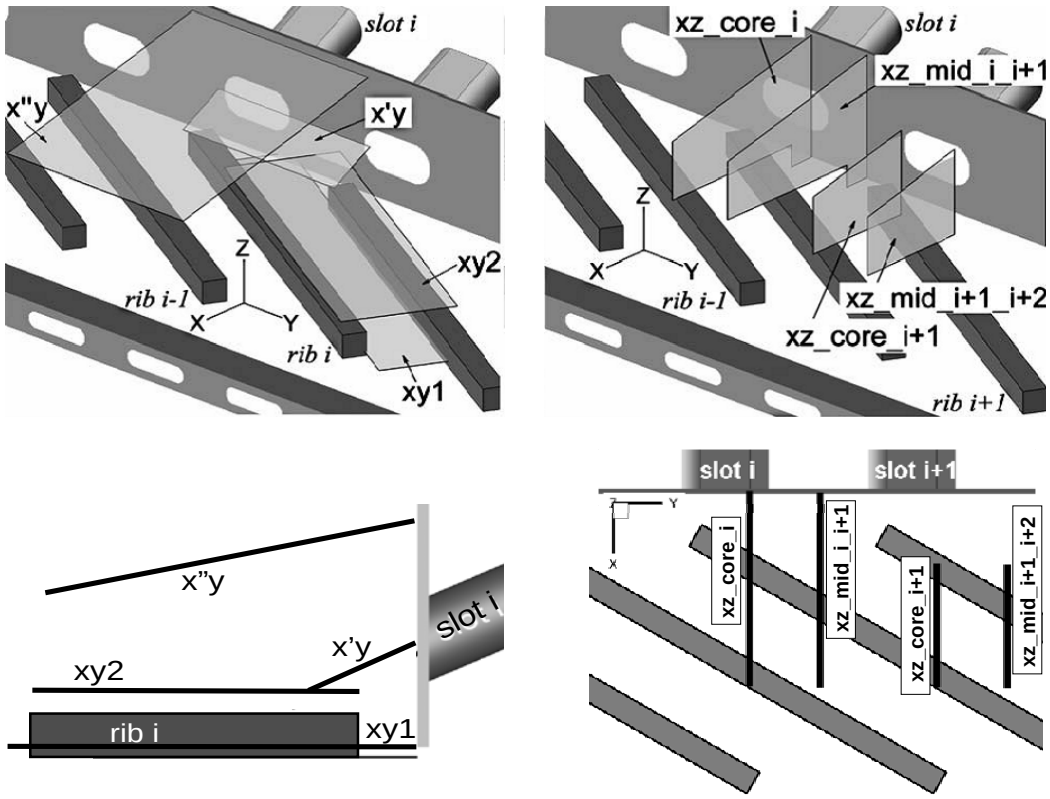


**Fig. 4.2** **PIV measurement planes: isometric view (top), lateral view (bottom left) and top view (bottom right)**

70 mm is adopted; the corresponding magnification factor is 13 pixel/mm, resulting in a field of view of about 100 x 70 mm$^2$. The latter choice is driven by the large size of this measurement window. However even in plane *x"y* the flow features are resolved with a satisfactory level of detail (see the following subsection).

The chosen separation time varies substantially among the measurement planes. An effort has been made to attain average particle displacements of 8 to 10 pixels, which is the recommended value: small enough to neglect acceleration or curvature in the trajectories of the tracers between the two exposures (Raffel et al. (1998)), but also large enough to obtain accurate results from the cross-correlation. The separation time is set at about 20 μs in the region of higher in-plane velocities (planes *xy1*, *x'y* and *xz_core* inside of the jet). Values of 35 to 40 μs are set for the areas of slower velocity (planes *xz_mid*, *x'y* and *xz_core* outside of the jet). Higher separation times in these areas (which are characterized by highly three-dimensional flow) would give raise to strong out-of-plane loss of particles and consequent deterioration of the measurement quality, as verified in the processing phase. In plane *x"y* the lower magnification factor dictates a larger separation time (55 μs).

The transparency of the test section (machined out of Plexiglas, with the inclined wall opposite to the ribbed wall made in scratch-proof glass) allows the optical access for laser and camera.

Planes *x'y*, *x"y* and *xy2* are obtained shooting the laser through the sidewalls (hub or tip in Fig. 3.1) and looking through the glass wall. For those planes, the lens set-up is a standard one, composed of a cylindrical lens with focal length $f$ = -40 mm and a spherical lens of $f$ = 600 mm.

Also for plane *xy1* the optical access for the camera is through the glass wall, but the laser is shot through the inlet channel and the mid-wall, in direction parallel to the ribs. In order to reduce the amount of light absorbed by the solid medium, and to avoid burning the Plexiglas, the part of the inlet channel wall crossed by the laser is substituted with a glass window (150 x 40 mm$^2$, 8 mm thick). Since the measurement plane is at only 2 mm from the wall, it is vital to minimize the laser sheet divergence, in order to keep its thickness as constant as possible for the long distance it travels close to the wall surface. For this purpose, a lenses configuration with two spherical lenses of opposite focal length ($f$ = -1000 mm and $f$ = 1000 mm) and one cylindrical lens ($f$ = -60 mm) is chosen. This guarantees a constant laser sheet thickness, as illustrated in Fig. 4.3.

Planes *xz* are obtained with an optical access from the side wall (the tip in Fig. 3.1). The laser sheet is deflected by 90° using a movable prism. This allows locating the measurement plane at different locations along the *y*-axis without displacing the laser head. The apparatus is displayed in Fig. 4.4.

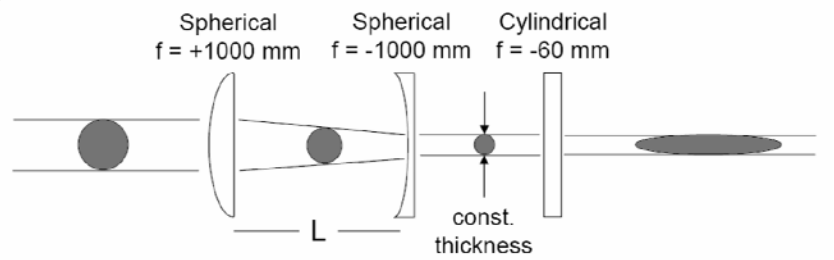


**Fig. 4.3** **Lenses configuration employed for plane *xy1* (Armellini (2007))**

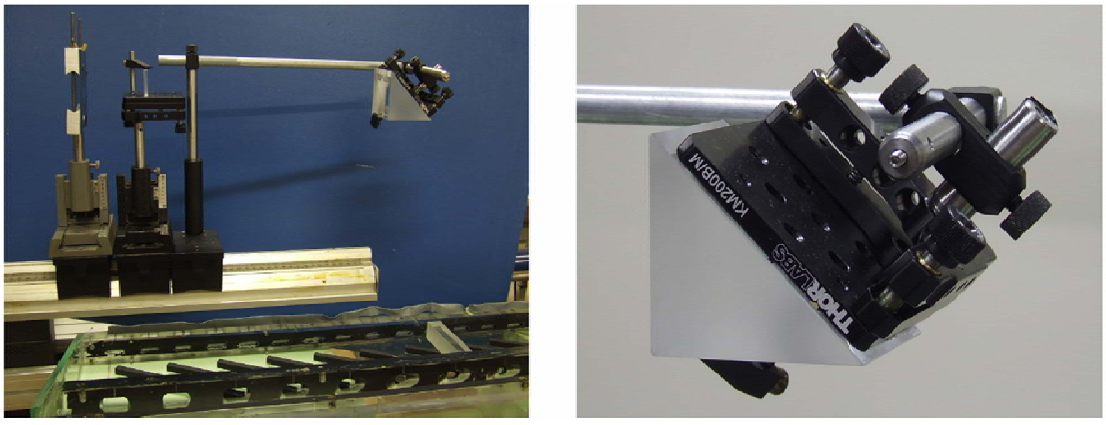

**Fig. 4.4** **Optics employed for planes *xz*: lenses and prism can slide on a rail (left); on the right, close up on the prism**

The camera optical axis is kept perpendicular to the measurement plane for all measurements. The acquisition frequency is set at 2 Hz, which guarantees that the realizations are statistically uncorrelated.

### 4.2.4 – Image processing

The processing is realized by means of the cross-correlation based interrogation algorithm Wi.D.I.M (Scarano and Riethmuller (2000)) which uses an iterative multigrid approach: the displacement field obtained on a coarse grid is used as predictor for computing the corrected displacement on a finer grid. At each refinement step the interrogation windows undergo a sub-pixel offset and a first order deformation. Such method is especially advantageous in flows presenting strong shear, as the one investigated here. The peak location is estimated by means of a three point Gaussian interpolation with sub-pixel accuracy, limiting the rms error to about 0.05 pixels. After each step of grid refinement, the software performs a validation procedure based on signal-to-noise ratio and deviation from neighborhood average.

Before submitting the PIV data to the processing code, an automatic subtraction of a background image is applied to every realization, in order to reduce the background noise. Generating a suitable background image is not trivial. The usual practice is to use the average of a series of images without seeding particles, collecting only the spurious information (e.g. reflections from the walls of the apparatus). However, the realizations without tracers do not necessarily give representative intensity levels, as they lack the light scattered by the particles. A method which uses images of seeded flow was suggested by Wereley et al. (2002) who generated the background image selecting the minimum gray intensity level at each pixel.

In the present work a novel technique to generate background images from realizations with tracers is applied (Armellini (2007)). In order to separate the noise from the particles signal, the root mean square (*rms*) of the light intensity fluctuations at each pixel is used: as the particles have a random position, the higher the *rms* at a certain pixel, the higher the probability that the light received by the detector comes from a particle (and not from a reflection or another steady noise). Given a series of realizations, the background intensity level for each pixel (*BI*) is the average intensity

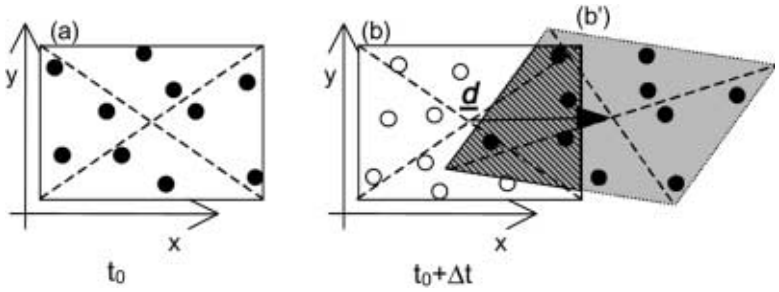


**Fig. 4.5** **Window transformation due to in-plane particle motion in the code Wi.D.I.M (source: Scarano and Riethmuller (2000))**

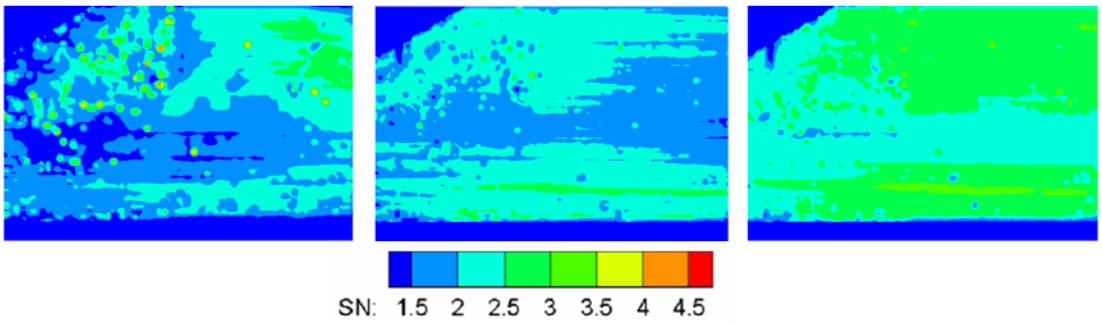


**Fig. 4.6** **Contours of signal-to-noise ratio: no background subtraction (left), subtraction of background generated from images without seeding (middle) and subtraction of background generated with the present method (right)**

value computed from the raw images (*AI*), weighted with the *rms* of the light intensity fluctuations (*IRMS*):

$$BI = C \cdot AI \cdot \left[ \left( 1 - \frac{IRMS}{\max(IRMS)} \right) \right] \tag{4.1}$$

The constant $C$ is added for tuning purposes, and is normally set between 0.7 and 1. This method proves to be successful in improving the measurement quality, especially for planes close to the wall surface. An example is given in Fig. 4.6, where the signal-to-noise ratio with and without background subtraction (no seeding approach and present approach) is displayed for a portion of plane *xy1*, which is the hardest region to investigate in this PIV campaign. Applying the present method, an acceptable signal-to-noise ratio is achieved.

Interrogation windows of 48 by 48 pixels$^2$ are used for the image processing, with one step refinement and 50% overlapping, for a final vector spacing of 12 pixels. This results in a resolution higher than 2 vectors per mm, i.e. a vector spacing of 0.05*e*, except for plane *x"y* where the lower magnification factor leads to about 1 vector per mm (vector spacing of 0.1*e*).

Vector validation is based on the signal-to-noise ratio and the local median threshold. Apart from a limited region of plane *xy1*, the signal-to-noise ratio is above 3 in every investigated area, and the percentage of invalid vectors is below 5%. Only valid vector where sampled to obtain the quantities presented in this thesis.

### 4.2.5 – Uncertainty of the flow statistics

The accuracy of a single PIV realization is affected by different kinds of error sources. The so-called *bias errors* affect in a different but steady way all the instantaneous velocity vectors. They are due to incorrect estimation of the

magnification factor, stability and accuracy of the trigger signals, velocity lag of tracer particles, optical distortion of the lens system, and cross-plane velocity component. The bias errors can be effectively controlled by an accurate choice of the measurement parameters. On the other hand the *random errors* are associated to the evaluation process of the instantaneous images. They can be significantly reduced if the tracers are sharply imaged and advanced evaluation algorithms are used. Such errors are random in nature (Keane and Adrian (1990), Willert (1996)) and hence are mostly filtered out in the averaging process.

When evaluating statistical quantities computed from a limited number of realizations, the sampling error must be considered. In the present case this error is expected to be much larger than other error sources, and therefore is taken as the overall upper bound error estimate. The time-averaged quantities are computed on the basis of 1000 realizations; the sampling frequency (2 Hz) is sufficiently low to consider each one statistically independent from the others. From the theory of signal analysis (Bendat and Peirsol (1986)), given $N$ independent samples, the normalized errors for the mean velocity and the *rms* of the velocity fluctuation can be computed as:

$$\varepsilon_U = \frac{\sigma[U]}{U} = \frac{Z_c}{\sqrt{N}} \frac{rms(u)}{U} \tag{4.2}$$

$$\varepsilon_{rms(u)} = \frac{\sigma[rms(u)]}{rms(u)} = \frac{Z_c}{\sqrt{2N}} \tag{4.3}$$

$U$ is the mean velocity (averaged over the ensemble of realizations), $u$ is the velocity fluctuation, $\sigma[\cdot]$ denotes the standard deviation, and $Z_c$ is the confidence coefficient, which is set here equal to 1.96 for a 95% confidence level. The resulting uncertainties in the mean velocities and *rms* are function of the measurement position, but are everywhere below 2% and 5%, respectively.

## *4.3 – Steady-state liquid crystals thermography*

### 4.3.1 – Thermochromic liquid crystals

Liquid crystals constitute a class of mesomorphic matter, unique in exhibiting mechanical properties of liquids (fluidity and surface tension) and optical properties of solids (anisotropy to light, bi-refringence). Certain liquid crystals (cholesteric or chiral nematic) are thermochromic: they react to changes in temperature rearranging their molecular arrangement, which in turn change the color they display.

Thermochromic liquid crystals (TLC) present four temperature-dependent phases. Below a given temperature, dependent on the chemical composition ($T_1$ in Fig. 4.7), TLC behave hydrodynamically like a cream or paste with high viscosity, and are

optically inactive. In this state the molecules are well ordered and close to each other like in a solid crystal. When the temperature increases above a given threshold ($T_1 < T < T_2$) the arrangement passes through the smectic phase, which belongs to the mesomorphic state characteristic of the TLC: the crystals are still optically inactive, but the molecules are separated in layers. As the temperature is further increased ($T_2 < T < T_3$) the molecules enter the cholesteric phase: in-between two layers, the molecules orientation is twisted by a certain angle; an overall helicoidal architecture is formed, i.e. the molecular director traces out a helix in space (Fig. 4.7, right). The degree of twist is defined by the pitch $p$, which is the height of the helix after one total rotation. The pitch is proportional to the wavelength $\lambda$ of the selectively reflected light, as described by the Bragg diffraction equation (Fig. 4.8, left):

$$n \cdot p \cdot \sin(\theta) = \lambda \tag{4.4}$$

where $n$ is the mean refraction index and $\theta$ is the angle of the incident light beam with respect to the layer. As $p$ decreases with increasing temperature, the reflected light changes from red to yellow, green, blue and violet (Fig. 4.8, right). The bandwidth of the wavelength of maximum reflectance ($\Delta\lambda$) depends on the TLC composition, and can be of 1 to 5 degrees Celsius (narrow-band TLC) or 10 to 20 degrees (wide-band TLC). If the temperature continues increasing ($T > T_3$), the liquid crystals typically undergo a further phase transition to an isotropic liquid, which is optically inactive. For further details on liquid crystals in general and TLC in particular the reader is referred to Fergason (1968), Collings and Hird (1997) and the handbook of Hallcrest Ltd. (1991).

TLC are widely used to provide surface temperature distributions with high-spatial resolution. Their selective reflectivity can be exploited for accurate temperature-color calibration, making them technically valuable for precise temperature field

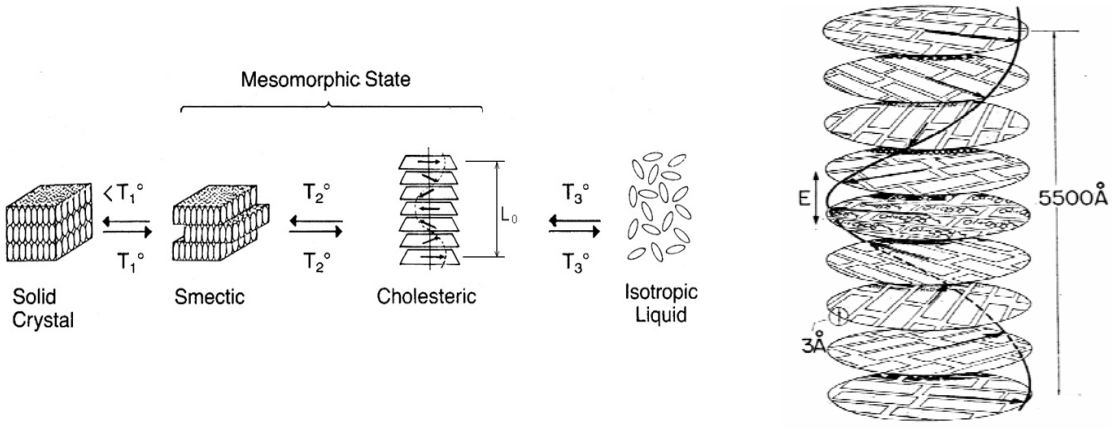


**Fig. 4.7** **On the left: schematic representation of the phase changes experienced by TLC (source: Hallcrest Ltd. (1991)). On the right: molecular organization of the cholesteric phase (source: Fergason (1966))**

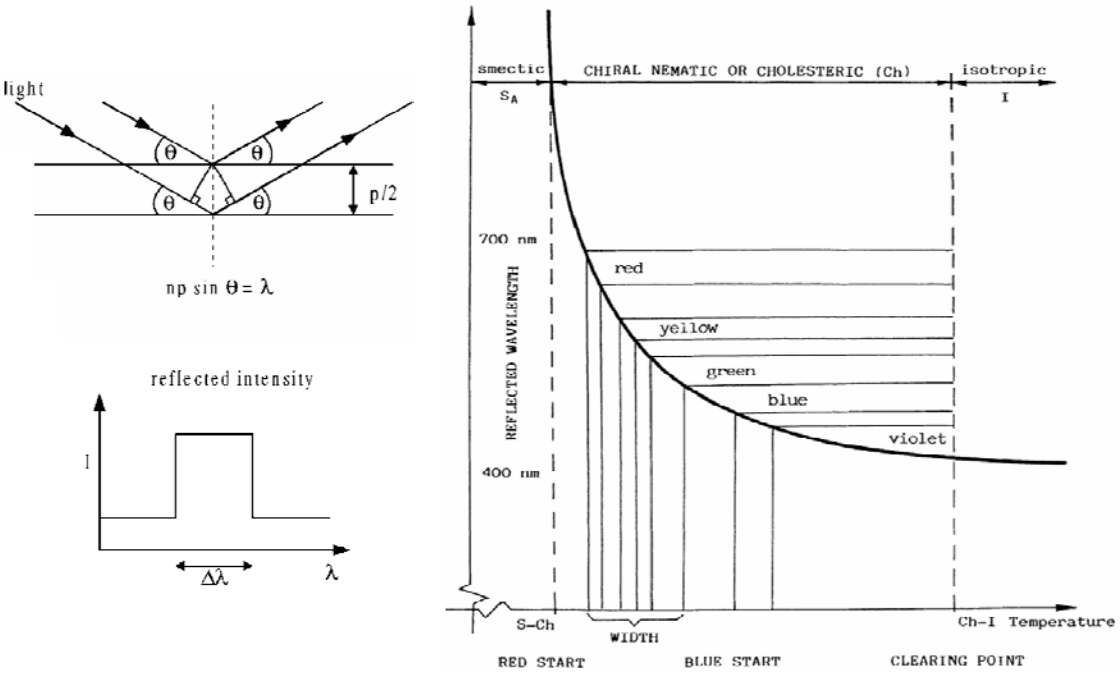


**Fig. 4.8** **On the left: simplified diagram of selective reflection of TLC (source: Ireland and Jones (2000)). On the right: wavelength of maximum reflectance and molecular state as a function of TLC temperature (source Stasiek et al. (1999)).**

measurements, as reviewed by Ireland and Jones (2000). Their primary advantage over competing techniques such as infrared thermography and temperature sensitive phosphor paints is their drastically reduced cost. A possible drawback is due to lighting and viewing angle effects on the reflected wavelength (first reported by Fergason (1968)) which causes a shift in the perceived color. However Farina et al. (1994) argued that an arrangement where a white light source and the detector are moved together over a TLC-coated surface will provide negligible color shift.

The most common fashion of applying thermochromic liquid crystals to a surface is to use a micro-encapsulated form of the material. Tiny spherical capsules with thin gelatin walls (about 20 microns in diameter) are diluted in a binder, and the emulsion is sprayed onto the model. The encapsulation prevents environmental factors like mechanical stresses, chemical agents and electrical fields from altering their optical properties. Encapsulated TLC are available in the temperature range of -30 to 115 degrees Celsius.

Several methods have been developed over the last two decades for performing thermal measurement in fluid dynamics by means of TLC. A first classification concerns the temporal nature of the experiments, i.e. steady state techniques and transient techniques. A second distinction is to be made on the method to capture the color information, i.e. single color capturing and hue capturing. Typical combinations are single color capturing in transient experiments using narrow-band TLC, and hue

capturing in steady state using wide band TLC, but other combinations have been successfully applied as well.

Major advancements in the various approaches are due to Akino and Ichimiya at Yamanashi University (Akino et al. (1989)), Moffat and Eaton at Stanford University (Farina et al. (1994)), Jones and Ireland at Oxford University (Wang et al. (1995)), Baughn and coworkers at University of California Davis (Baughn et al. (1985)), Camci and co-workers at Pennsylvania State University (Camci et al. (1992)), Arts and co-workers at VKI (Rau et al. (1993)), and Weigand and von Wolfersodorf at Stuttgart University (Poser et al. (2007)). Among the several reviews available, the reader is referred to the one by Ireland and Jones (2000).

In the present thesis the steady state technique with single color capturing is used, as proposed by Akino et al. (1989). The advantage of this method is the absence of any numerical scheme required to retrieve the heat transfer coefficient, and the simple and relatively inexpensive hardware requirement. The major drawbacks are the long total measurement time, the difficulties in applying the heater foil onto the channel surface, and the need for developing a reliable tool for the detection of isochromatic/isothermal lines.

### 4.3.2 – Calibration of the TLC

The idea at the base of the technique proposed by Akino et al. (1989) is to use optical band-pass filters to extract isochromatic/isothermal lines along a heated surface coated with TLC. Adjusting the heating regime, the experimentalist can cover the complete investigated area in terms of heat transfer information. The resulting thermal map can be used to evaluate the heat transfer coefficient, provided that the convective heat flux is accurately known.

In the present case the instrumentation for the TLC calibration and measurement comprises:

- two different microencapsulated TLC sprayable coatings, R35C5W and R55C5W, from Hallcrest Inc.
- black paint, also from Hallcrest Inc.
- four 50 W tungsten halogen lamps
- an instrumented calibration plate (described in the following)
- one 2.4 kW DC power supply
- foils of Inconel 600, 25 microns in thickness
- double-side adhesive of high thermal conductivity, from 3M©
- one grey-scale *IMC-500* 8-bit CCD camera, 512 x 512 pixels
- five narrow band optical filters of central wavelength 550, 590, 599, 610, and 640 nm

- acquisition system connected with the camera provided with image grabbing software (i2S-PCScope™)

A mix of two TLC types is used: R35C5W, and R55C5W. As their codes suggest, they are nominally active in the range 35-40°C and 55-60°C, respectively. The use of a mixture of liquid crystals has the advantage that less heating regimes are needed to map out the heat transfer coefficient distribution on the investigated surface. Furthermore, since in the considered cooling scheme highly and poorly cooled regions coexist, detecting isotherms at 55°C in a strongly cooled region requires heating regimes that would damage the channel walls in the weakly cooled areas (as Plexiglas softens at 60°C). The straightforward solution of using only low temperature TLC is unsatisfactory, as this would decrease the driving temperature head $\theta$ for all measurements, which would unnecessarily reduce the accuracy (see Appendix A for a detailed uncertainty analysis). Of course attention must be paid in distinguishing one TLC from the other in the color display, but the large difference in activation temperatures leaves no space for ambiguity. The choice of the activation bandwidth (5°C, relatively broad for this technique) is dictated by the will of resolving isotherms for different colors also in regions of high spatial temperature gradients. The two types of TLC are calibrated both separated and after mixing: R35C5W does not show appreciable discrepancies between the two cases, while R55C5W presents, after mixing with R35C5W, a shift of almost half a degree towards lower temperatures. The reasons for this behavior are unclear; however only the mix is used and the corresponding calibration is adopted.

The calibration plate is depicted in Fig. 4.9. It consists of a 3 mm thick slab of aluminum, along which a linear temperature gradient is established by means of a resistive heater and a cooling serpentine tube placed at both ends of the plate. The linearity of the temperature distribution is checked by 9 T-type thermocouples, inserted at 0.5 mm below the surface and equally spaced along the slab. To enhance the contrast, the plate is first sprayed with a layer of black paint, on top of which the TLC mix is applied. An airbrush with a 1.5 mm nozzle is used for applying both the black paint and the TLC. The total thickness of the coating (black paint and liquid crystals) is kept as low as possible (less than 80 microns), in order to have a negligible temperature gradient across it. The thermocouple locations are marked by white dots using a perforated template. The slab is insulated by low conductivity material (*TAUfoam*, $k$ = 0.024 $Wm^{-1}K^{-1}$) to reduce conduction losses, and enclosed in a Plexiglas case to avoid natural convection. Thermal steady state is reached along the plate at a temperature range for which the TLC are active, and the intensity is detected through the CCD camera. The band-pass filters are mounted on a revolving disk, so that they can be placed successively in front of the camera objective. As for the illumination, halogen lamps are installed to avoid direct reflection into the camera sensor. Attention is paid to maintain a fixed angle (about 45 degrees) between the axes of the lamps and the optical axis of the camera, to be reproduced during the measurements: as reminded above, keeping the same relative orientation of light sources and camera minimizes the shift in the detected color (Farina et al. (1994)).

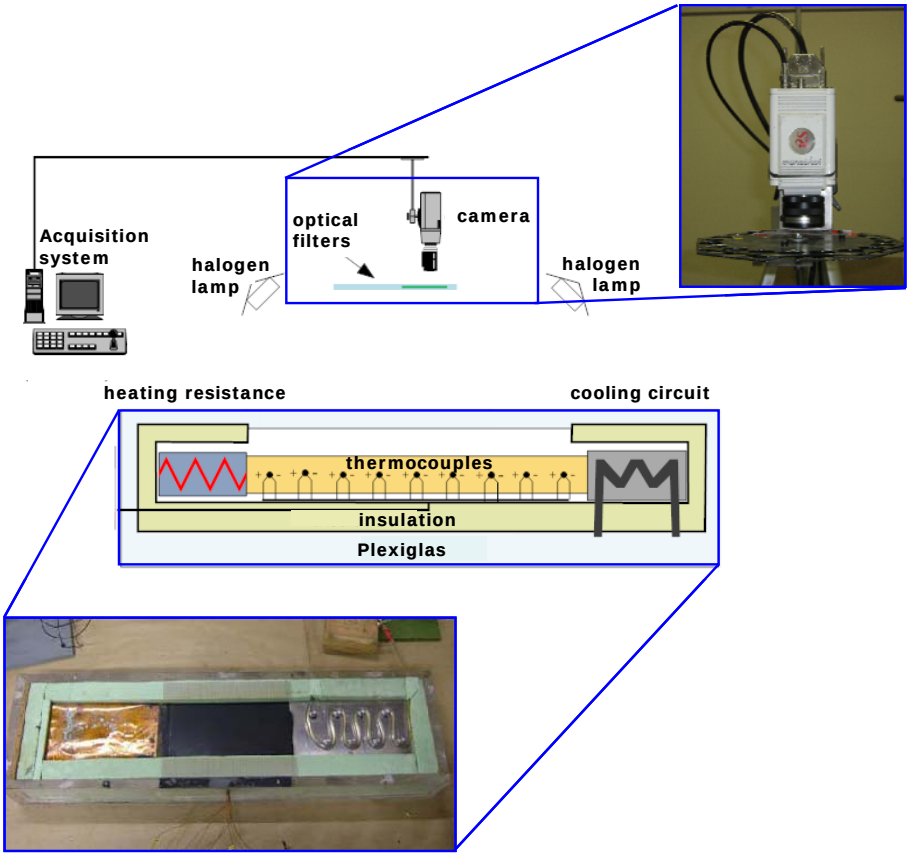


**Fig. 4.9 Schematic of the calibration plate for TLC**

A typical grayscale display of the calibration plate is shown in Fig. 4.10, along with the intensity profile extracted along a horizontal abscissa, directed as the thermal gradient. The intensity recorded by the detector (camera plus optical filter) exhibits a maximum at the central wavelength of the selected filter. The thermocouples provide the *peak intensity temperature*, i.e. the temperature at the abscissa corresponding to the peak, which is therefore associated to the corresponding wavelength. One hundred horizontal profiles are extracted and averaged in order to exclude spurious peaks. To further reduce the uncertainty, several independent calibrations (from 15 to 20) with different temperature gradients are considered, and the final uncertainty is deduced from statistics, using a relation equivalent to Eq. 4.2, with the peak intensity temperature in place of the velocity. The results of the calibration for the two types of TLC in the mixtures are presented in Fig. 4.11, where the error bars are associated to a 95% confidence level.

The processing of the calibration images is automatically realized by an algorithm implemented MATLAB® and includes:

- detection and location of the thermocouple positions

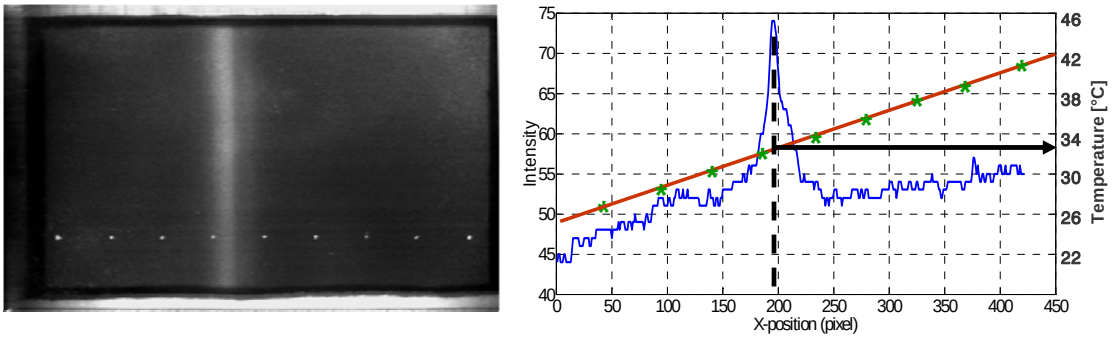


**Fig. 4.10** **Left: grayscale display on the calibration plate, as detected by the CCD through the optical filter. Right: intensity profile extracted along a horizontal abscissa**

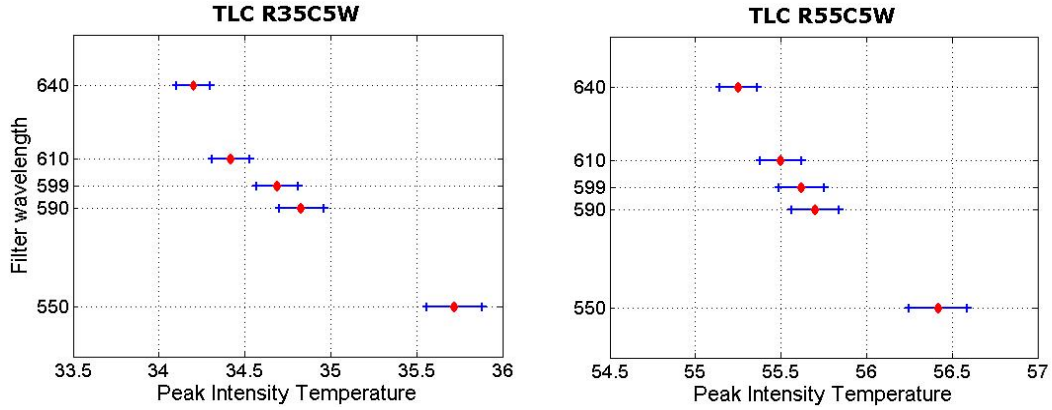


**Fig. 4.11** **Calibration of the TLC mixture for the two types of liquid crystals used**

- extraction and averaging of the intensity profiles
- quantification of the temperature gradient
- evaluation of the peak intensity temperatures and estimation of the uncertainty

The user performs all the operations through a graphic interface.

### 4.3.3 – Detection of the isotherms

By means of TLC calibration, the color display along the investigated surface can be converted in temperature distribution, or more exactly in contours of five temperature levels, one for each optical filter used during the calibration.

In the captured grayscale image, the isochromatic/isothermal lines along the heat transfer surfaces are lines of maximum intensity. Therefore the problem of identifying

isotherms translates in the one of detecting maximum intensity lines. The latter is a classical problem of pattern recognition in digital images. In the present thesis, an algorithm based on the method for boundary tracking described by Castleman (1995) is developed and applied. The work performed by Luca Patricelli during his Short Training Program at VKI (Patricelli (2007)) has been instrumental for the development and implementation of the algorithm.

In its basic version, the detection algorithm searches the 3 x 3 neighborhood centered on the point (i.e. pixel) *i*, supposed located on the line of maximum intensity: given the current point *i* and the previous one *i-1*, the candidates as successive point *i+1* are the neighbor diametrically opposite to the previous point and the neighbors on either side of it; the one with highest gray level is selected (Fig. 4.12, left). However, if the image is noisy this type of tracking is likely to deviate from the path of maximum intensity. Noise effects are reduced by implementing the so-called *tracking bug* Castleman (1995): a rectangular averaging window is defined to embody the bug, whose rear portion is centered on the current point *i*, while its orientation is given by the current and the previous point *i-1* (Fig. 4.12, right). The bug is subsequently oriented at an angle $\alpha$ to either side, looking for the new direction, and the average intensity under the bug is computed for each position. When the bug is in the position of highest average intensity, the next point *i+1* is taken as one of the pixels under its front portion.

The present application of the method is implemented in MATLAB®, and the detection of the maximum intensity paths (corresponding to isochromatic/isothermal paths) is eased by the selection of a number of *guide points*, which can be picked on the image via a graphical user interface: the position of the next guide point drives the choice of the pixel to be selected among the ones on the front portion of the bug. The first guide point is the location where the bug starts its tracking. When the last guide point is reached, the pixels selected during the tracking process are fitted with a piecewise Hermite cubic spline. An example of the application of the algorithm on a TLC display is presented in Fig. 4.13. The algorithm is provided with a graphic user

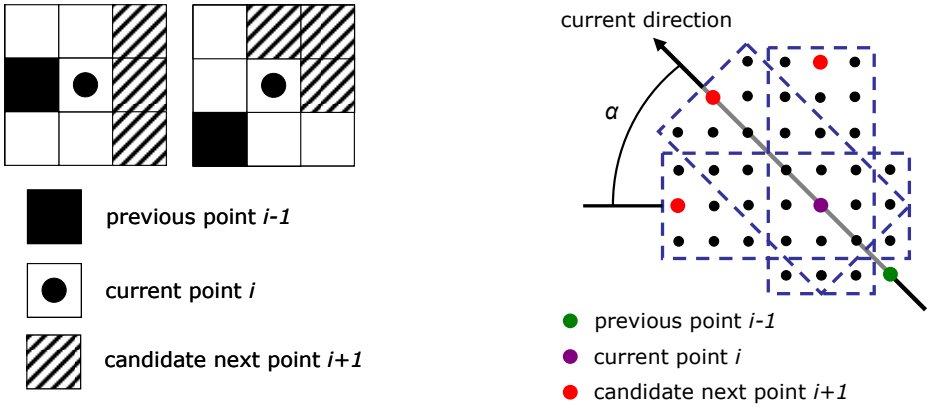


**Fig. 4.12** **Illustration of the tracking process: 3x3 neighborhood (left) and tracking bug (right). After Castleman (1995).**

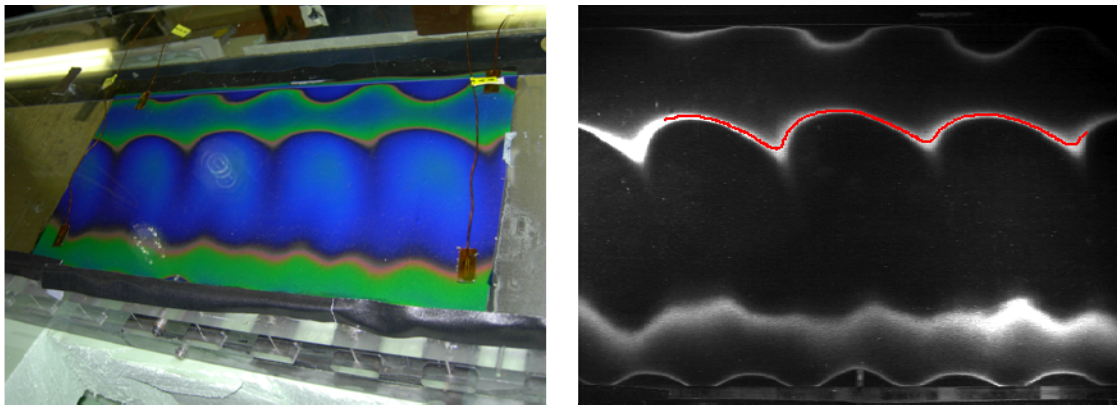

**Fig. 4.13** **Example of the application of the tracking algorithm: TLC color display (left) and maximum intensity line detected on the grayscale image (right)**

interface, which allows for selecting the guide points, the size of the bug and the angle of investigation $\alpha$, besides applying a projective transformation for the images skewed by the perspective.

### 4.3.4 – Measurement procedure

As mentioned above, the knowledge of the temperature distribution along the surface allows the evaluation of the heat transfer coefficient, provided that the heat flux extracted by convection is known and a reference fluid temperature is defined. A uniform heat flux boundary condition is imposed at the solid-fluid interface dissipating direct current through a foil of Inconel 600 (25 microns in thickness) which is connected to a 2.4 kW power supply, and glued with a highly conductive adhesive (also about 25 microns) onto the wet side of the wall. This provides a uniform heat flux boundary condition for the heat transfer process, which is therefore purely convective, in the sense specified in Chapter 2. The choice of Inconel as resistive material is suggested by the fact that its thermal and dielectric properties vary negligibly in the present temperature range.

The application of heating foils and TLC coating onto the channel surfaces is performed in different ways, depending on the investigated areas (Fig. 4.14): when investigating the impingement wall, the Inconel is glued on the Plexiglas surface and coated with black paint and TLC; in the ribbed configurations, Plexiglas ribs are glued on top of the coating. When investigating the opposite smooth wall, the liquid crystals are sprayed directly on the Plexiglas wall, the black paint is applied on the TLC, and the Inconel foil is glued onto the coating. For the measurements on the rib surface, first the Inconel foil is carefully folded and glued on the target rib; then the ensemble is inserted in a slot open in the bottom wall; finally it is coated with black paint and TLC (Fig. 4.15). This strategy greatly eases the application of the heating foil on the turbulator, with respect to gluing it on the ribbed wall. The inserted rib is machined

out o of rigid insulating foam *TAUfoam*, in order to minimize the conductive losses. This arrangement has been devised and tested during the VKI Short Training Program

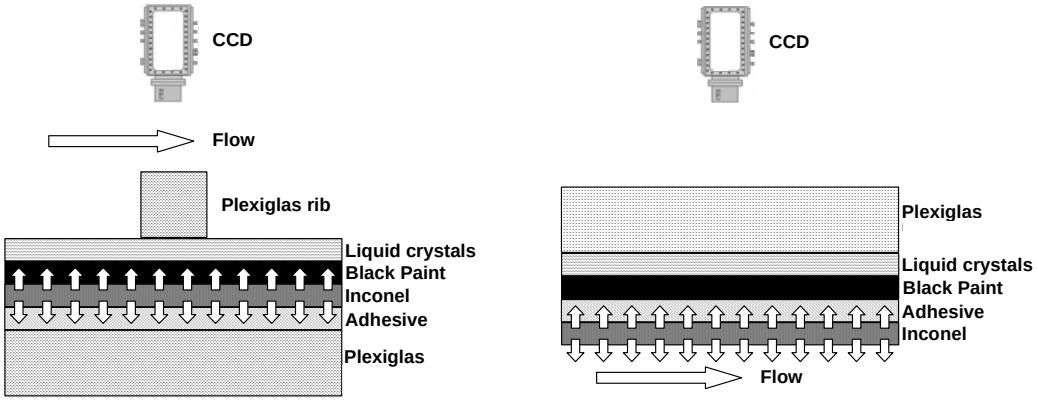


**Fig. 4.14** **Schematic of the arrangement for TLC measurements on the floor of the impingement wall (left) and the opposite smooth wall (right)**

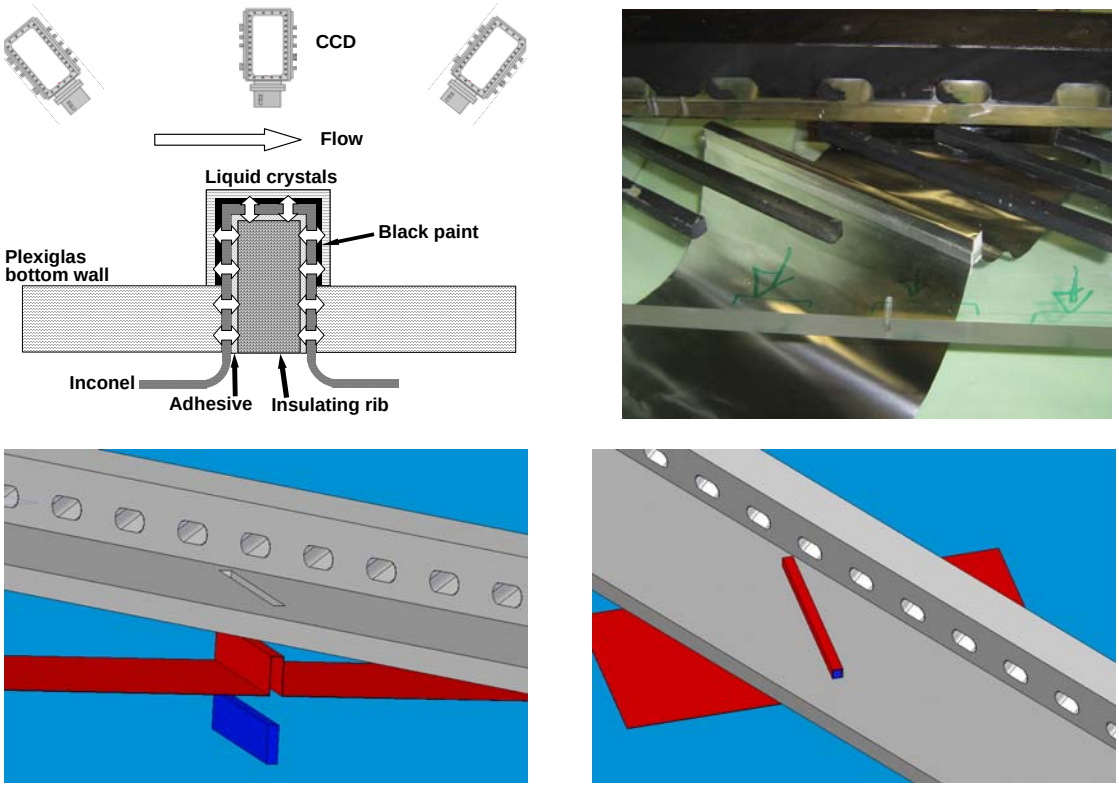


**Fig. 4.15** **Method for TLC measurement on the rib surface: top left: schematic of the arrangement; top right: the investigated rib wrapped in the Inconel foil and inserted in the ribbed wall; bottom: CAD representation of the arrangement**

of Emanuele Facchinetti (Facchinetti (2008)).

The temperature distribution along the investigated wall can be measured as long as the surface is kept within the activation range of the TLC. This is accomplished by varying the heat flux level, i.e. tuning the Joule power across the Inconel foil. By doing so the isotherms are shifted over the entire investigated surface; full coverage is obtained with 10 to 15 heating regimes. For each power level, steady state conditions are attained in about 20 to 25 minutes (no visible change in the color pattern); the TLC image is acquired about 15 minutes after that.

To maximize the robustness of the method, the same apparatus used for calibration (CCD camera, optical filters, lamps, with given relative orientation of lamps and camera) is employed during measurements. When looking at the impingement floor and at the opposite smooth wall, the optical access is relatively simple, with the camera perpendicular to the considered surface. When looking at the rib surface, three different orientations of the camera (and hence of the lights) are employed in order to optimize the resolution. The maximum angle between the optical axis with respect to the wall-normal never exceeds 40 degrees; as attention is paid to keep the same relative orientation of camera and lamps, the TLC show no appreciable color shift. A typical resolution of 3 pixels per mm is achieved in the acquired images.

### 4.3.5 – Heat transfer evaluation and thermal losses assessment

In pure convection, which is the regime investigated by TLC thermography, the heat transfer performance will be quantified in terms of Nusselt number:

$$Nu = \frac{hD_{mid}}{k_f} \tag{4.5}$$

where $h$ is the heat transfer coefficient, $k_f$ is the thermal conductivity of the fluid (air) and $D_{mid}$ is the hydraulic diameter of the mid-wall slots. The latter is taken as reference length, since the jet impingements prove to be the dominant feature for the aero-thermal performance. The heat transfer coefficient is defined as:

$$h = \frac{Q_{conv}}{A_h(T_w - T_f)} \tag{4.6}$$

where $Q_{conv}$ is the power heat released in the flow by forced convection, $A_h$ is the heated area, $T_w$ is the wall temperature measured by TLC and $T_f$ is the reference flow temperature. The latter is defined as the total temperature of the flow entering the test section $T_{inlet}$, monitored with a K-type thermocouple. This definition is preferred to a mean flow temperature, due to the difficulty of defining a clear flow direction, and to the unfeasibility of measuring the temperature along the exit of the channel for each heating regime. A limited number of temperature measurements along the exit slots (described in detail later) indicate that a definition of $T_f$ based on mean (inlet/outlet)

air temperature would lead to a reference fluid temperature about 1.7 K higher then $T_{inlet}$, which in turn would lead to an increase in the evaluated Nusselt number levels of about 6 to 10% (depending on the local wall temperature).

$Q_{conv}$ can be computed from the energy balance applied to the investigated surface:

$$Q_{conv} = Q_{Joule} - Q_{rad} - Q_{cond,h} \tag{4.7}$$

$Q_{Joule}$ is the power dissipated inside the heating element applied on the surface, while $Q_{rad}$ and $Q_{cond,h}$ are the thermal losses respectively by radiation and by conduction through the heated wall, as depicted in Fig. 4.16. The power input is:

$$Q_{Joule} = VI \tag{4.8}$$

where $I$ is the current dissipated when applying a voltage $V$ across a heating foil of area $A_h$. The applied voltage range between 6 and 11 volts, with corresponding levels of current from 20 to 37 amperes, resulting in an imposed Joule power per unit area of 550 to 2100 $Wm^{-2}$. When studying the floor in between two ribs, the uniformity of the Joule heat flux is affected by the presence of the Plexiglas turbulators glued on the heating foil. In order to qualify such effect, a study using the finite element method (FEM) is carried out by means of the software COMSOL Multiphysics® (Fig. 4.17): a two-dimensional model including an Inconel foil inserted between a Plexiglas wall and a Plexiglas rib is discretized with an unstructured mesh of about 24,000 elements and studied by FEM under heat transfer conditions representative of the investigated case: a distributed heat source (representative of the applied power input) is applied inside the heating layer, while a conduction losses of $0.05Q_{Joule}$ is assumed (in accordance with the experimental value reported below); piecewise distributions of heat transfer coefficients are imposed along the three sides of the obstacle. Although the $h$ distribution has a significant effect on the quantitative results, the qualitative trend is the one displayed in Fig. 4.17: the wall-normal heat flux $q$ presents

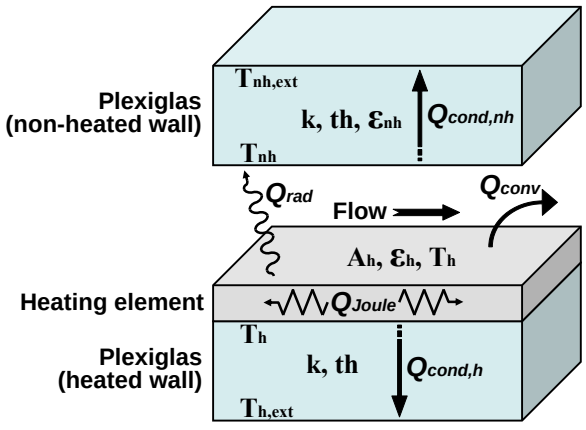


**Fig. 4.16 Schematic of the energy balance in the heated cavity**

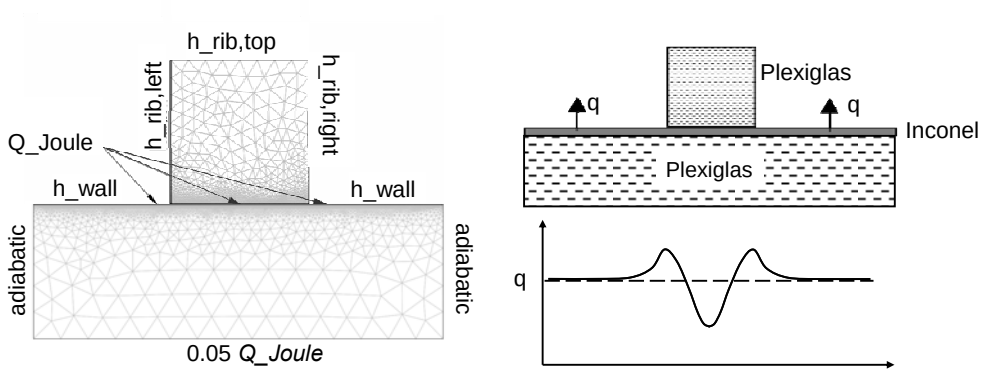


**Fig. 4.17** **Effect of the Plexiglas rib mounted onto the heating foil. Left: discretized domain. Right: qualitative heat flux trend from the FEM analysis**

local peaks in the vicinity of the rib, which can be as high as 180% of the nominal level. However those singularities die out (within the uncertainty associated to the value of the nominal Joule power) at a distance of 0.2*e*, and therefore do not significantly affect the heat transfer levels on the target surface.

The radiative heat is computed using a simplified model for parallel and isothermal plates, neglecting the presence of the lateral walls and the small relative inclination of the two large walls:

$$Q_{rad} = \frac{A_h \sigma \left( T_h^4 - T_{nh}^4 \right)}{\frac{1}{\varepsilon_h} + \frac{1}{\varepsilon_{nh}} + 1} \tag{4.9}$$

$\varepsilon$ is the emissivity and $\sigma$ is the Stefan-Boltzmann constant. The subscript $h$ corresponds to the heated surface, the subscript $nh$ to the non-heated one. In the present case $T_h$ is equal to $T_w$, while $T_{nh}$ is averaged from three K-type surface thermocouples glued on the non-heated wall. The emissivity for the heated (TLC coated) surface is assumed to be $\varepsilon_h = 0.9$ (according to Batchelder and Moffat (1997)); the non-heated wall, being of Plexiglas, is assumed to have an emissivity $\varepsilon_{nh} = 0.86$ (quoting the vendor). The best estimation for $Q_{rad}$ ranges from 2% to 7% of the imposed Joule power, depending on the heating foil temperature, which varies within the liquid crystals activation range.

The conductive loss through the heated wall is computed assuming 1D conduction:

$$Q_{cond,h} = \frac{A_h k_{Plexi}}{th} \left( T_h - T_{h,ext} \right) \tag{4.10}$$

$k_{Plexi}$ is the thermal conductivity of the Plexiglas wall (0.19 $Wm^{-1}K^{-1}$) and $th$ is its thickness. The thermal driving potential ($T_h - T_{h,ext}$) is measured by several pairs of surface thermocouples glued on opposite sides of the wall. $Q_{cond,h}$ is kept below 5% of

the input Joule power when heating the impingement wall, thanks to the use of a strongly insulating material (*TAUfoam*) below the Plexiglas. When heating the opposite wall, the conductive loss is as high as 10%, due to the fact that no opaque insulator can be used for reasons of optical access.

An alternative way of computing the conduction loss is to assess the total enthalpy drop across the model, performing the following energy balance:

$$\sum_{i=1}^{N}\left[\int_{exit\cdot slot}\rho U c_p T_0 dA\right]_i - \int_{inlet\cdot section}\rho U c_p T_0 dA = Q_{Joule} - \left(Q_{cond,h} + Q_{cond,nh}\right) \quad (4.11)$$

In Eq. 4.10 there is no radiative term, as the Plexiglas is opaque to the infrared wavelengths and therefore no thermal radiation from the heating foil is exchanged with the ambient. On the other hand, the conduction loss includes now also the heat released through the non-heated wall, $Q_{cond,nh}$. The total enthalpy drop (left hand side of Eq. 4.10) is evaluated from velocity and total temperature measurements performed both in the inlet section and at the outlet of the exit slots. For the latter, data are acquired via a Prandtl tube (1.5 mm in diameter) and a K-type thermocouple inserted in a Monel tube (1.2 mm in diameter), which are traversed downstream of three exit slots in the central part of the channel, considered representative of most of the test section. Measurements are performed for a representative heating regime of 1500 $Wm^{-2}$. Figure 4.18 displays the two probes, while Fig. 4.19 illustrates the measurement grid (46 points for each of the three investigated slots). The evaluation of the enthalpy drop allows for assessing the total conduction loss (through heated and non-heated wall). $Q_{cond,nh}$ is also directly evaluated by means of several pairs of surface thermocouples, and found to be below 2% of the input Joule power. This allows for computing the

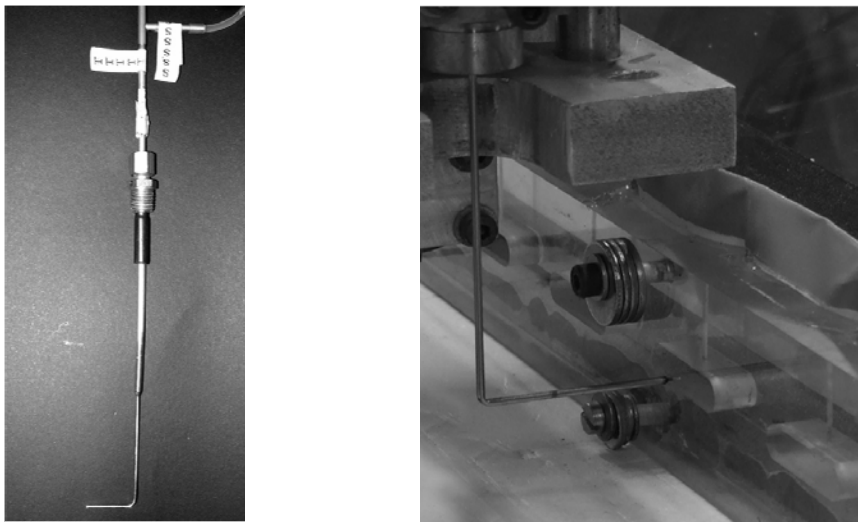

**Fig. 4.18** **Probe traversed downstream the exit slots. Left: Prandtl tube. Right: thermocouple**

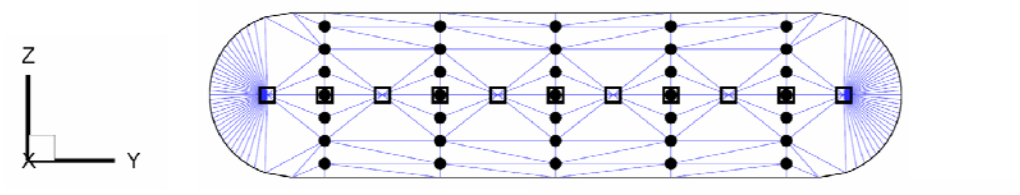


**Fig. 4.19** **Investigation of exit conditions. Top: measurement grid in the section of the exit slot. Bottom: flow temperature raise above the inlet temperature (left) and outlet velocity contour (right)**

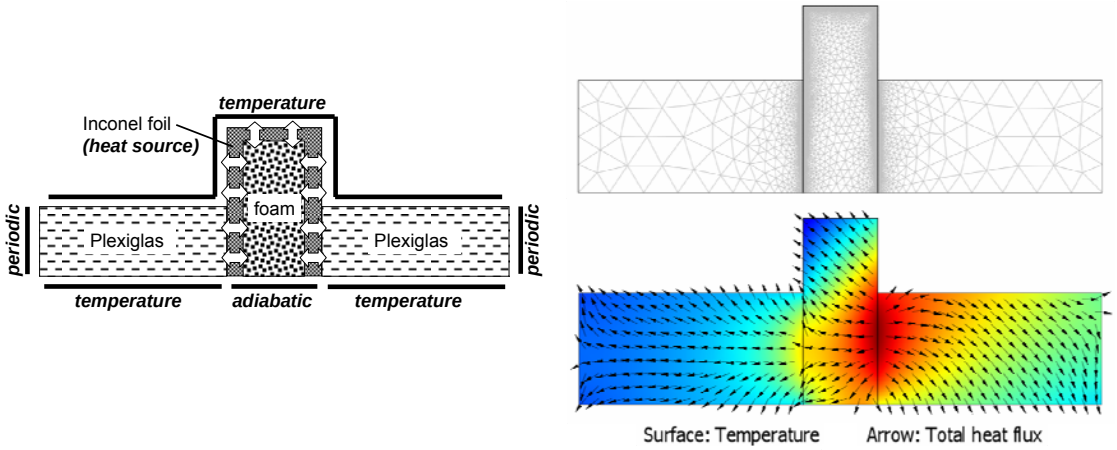


**Fig. 4.20** **FEM of the heated rib. Left: schematic of the model and boundary conditions. Right: mesh and resulting thermal pattern (red and blue indicates higher and lower temperature respectively)**

conduction loss through the heated wall, and comparing it with the direct evaluation by Eq. 4.9. The discrepancy is almost $0.05Q_{Joule}$, and is attributed to the uncertainty associated to both methods: in the first approach the strong local temperature gradients make difficult a global estimation of the conductive effects assuming 1D conduction; in the second one the enthalpy balance is based on very small inlet-to-exit temperature differences, which are hard to measure precisely. The direct evaluation by thermocouples is considered the most reliable, and its results are used for evaluating the heat transfer coefficient.

When investigating the rib surfaces, the three-dimensionality of the obstacles requires a specific analysis in assessing the thermal loss: for this purpose, a two-dimensional model similar to the experimental arrangement in Fig. 4.15 is built up in COMSOL Multiphysics®: it is discretized by an unstructured mesh of about 40,000 elements and studied by finite element analysis applying the thermal boundary condition specified in Fig. 4.20. The temperature imposed at the outer side of the floor results from a piecewise linear distribution obtained byinterpolating the data from five K-type surface thermocouples, while the temperature imposed on the wet wall is taken

from a typical TLC display when heating the rib. The side of the turbulator facing the jet is the left one in Fig. 4.20. The resulting heat flux pattern shows that the heat transfer unbalance leads to a positive conduction contribution to the convective heat flux on the impingement side and on the tip of the rib: indeed the conductive heat generated on the right side of the rib is conveyed to the other two sides of the turbulator, resulting in an increased level of heat flux extracted from those sides. To account for this effect, $Q_{conv}$ is computed correcting the total nominal Joule power input by the following conduction terms: $+0.065Q_{Joule}$ on the tip of the rib, $+0.08Q_{Joule}$ on the left side and $-0.07Q_{Joule}$ on the right side. The accuracy of these estimations is limited by the fact that the temperature distribution does vary along the length of the rib.

When considering the rib surface, the obstacle is regarded as a small object in a large cavity, and $Q_{rad}$ is negligible.

### 4.3.6 – Uncertainty of the convective heat transfer measurements

This subsection presents the results of the uncertainty analysis for the liquid crystals thermography. It is based on the Gaussian error propagation equation (i.e. the root-sum-square method) as described by Kline and McClintock (1953) and Moffat (1988), for a 95% confidence level. However, when is felt that the mutual independency of the different sources of error is not clearly assessed, a more conservative estimation is given summing up the absolute values of the different errors. The detailed calculation of the uncertainty is presented in Appendix A.

Given the definition adopted here for the heat transfer coefficient, its uncertainty mainly depends on the wall temperature measurements and on the evaluation of the heat flux truly extracted by forced convection.

The accuracy associated to the wall temperature depends not only on the precision of the TLC calibration, but also on the process of detecting the isotherms on the investigated surface. From Fig. 4.11, the maximum uncertainty associated to the TLC calibration appears to be ±0.2 K, but this value assumes exact reading of the thermocouples. Including a maximum error ±0.15 K from the K-type thermocouples, a value of ±0.35 K is taken as a conservative estimation of the TLC temperature. Possible maximum errors of about ±4 pixels in the isotherms localization process might occur: considering the resolution (about 3 pixel/mm) and the existing thermal gradients (typically below 0.5 K/mm), maximum errors of ±0.7 K are associated to the detection process. This leads to a global wall temperature uncertainty of about ±0.8 K.

The accuracy associated to the convective heat flux is mostly affected by errors in the thermal losses estimation. The uncertainty on the losses is estimated conservatively as 30% of the calculated value. As a result, $Q_{conv}$ is considered accurate within $0.02Q_{Joule}$ on the impingement wall and $0.03Q_{Joule}$ on the opposite smooth wall.

Finally, the experimental uncertainty of the heat transfer coefficient ranges between 5% and 11% depending on the location. The uncertainty on the Nusselt number is somewhat higher, between 6 and 12%, due to the inaccuracy on $D_{mid}$.

## *4.4 – Infrared thermography*

### 4.4.1 – Principles of infrared thermography

As the temperature of a body exceeds the absolute zero, the molecular agitation in the matter results in an electromagnetic radiation: the energy released increases with the body temperature. The radiation carrying thermal energy is confined to the wavelength range $0.1 \leq \lambda \leq 1000$ μm, in which one can identify the visible spectrum and the infrared spectrum. Infrared thermography measures surface temperature detecting the electromagnetic energy radiated by an object in the infrared spectral band.

The infrared spectrum is conventionally split into near, mean and far infrared (Fig. 4.21). The radiative power per unit surface emitted at a wavelength $\lambda$ by a body at absolute temperature $T$ is the spectral emissive power $M_\lambda$, which is a function of the wavelength, the surface temperature and the monochromatic emissivity $\varepsilon_\lambda$. The total emissive power over the whole spectrum is given by the Stefan-Boltzmann law:

$$M(T) = \int_0^\infty M_\lambda d\lambda = \varepsilon \sigma T^4 \tag{4.12}$$

where $\sigma$ is a universal constant. For a given temperature, the maximum attainable emissive power is given by a value of emissivity equal to 1; in this case the surface is named a black body. The latter is an ideal condition which can never be achieved by real bodies, even if it can be approximated, e.g. by dull black surfaces.

The principle of infrared (IR) thermography consists in capturing the infrared radiation emitted by a surface using an infrared radiometer (i.e. a camera sensitive to IR radiation) and transforming it in a signal which, once processed, leads to the determination of the local surface temperature. Infrared radiometers are composed of an optical unit which collects and focuses the thermal radiation beam on a photovoltaic detector; in order to increase the sensitivity, the detector is maintained at very low temperature by a cryogenic device based on Stirling cycle or on Peltier

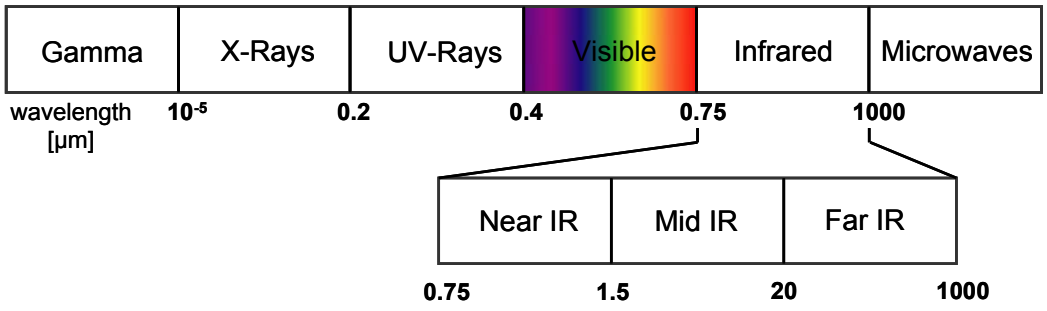


**Fig. 4.21** **Wavelength of electromagnetic radiation: spectrum with expanded infrared region**

cooling effect. In modern IR cameras the detector consists of an array of sensible elements (focal plane array, FPA) which allows visualizing a two-dimensional thermogram: each pixel is characterized by an intensity level proportional to the impinging radiation. Most of the IR cameras (as the model used in the present investigation) work in the mean infrared, particularly between 3 μm and 14 μm, as in this range of wavelength the atmosphere presents spectral bands with high IR transmissivity.

The performance of IR radiometers for steady applications is expressed by thermal sensitivity and spatial resolution. The thermal sensitivity is related to the smallest temperature difference which can be discriminated in a thermal field; this corresponds to a signal to noise ratio equal to 1, and is referred to as Noise Equivalent Temperature Difference (NETD). The spatial resolution of a FPA detector can be quantified by the instantaneous field of view (IFOV), which is the angular projection of a single element of the FPA on the image plane.

One difficulty of evaluating temperature distributions by means of IR thermography comes from the reflectivity $\rho$ of the surface imaged by the IR radiometer. The reflectivity of an opaque body (i.e. a body which has zero transmissivity) is inversely proportional to its emissivity:

$$\rho = 1 - \varepsilon \tag{4.13}$$

If a surface is characterized by high reflectivity, it will reflect an infrared energetic content emitted by the surrounding ambient at temperature $T_{amb}$. As a result, neglecting the absorptivity of the air, the infrared radiometer will receive from the investigated surface a radiative power $E$ containing two contributions:

$$E = \varepsilon\, M(T) + (1-\varepsilon)\, M(T_{amb}) \tag{4.14}$$

The second term of the right hand side of Eq. (4.13) fouls the measurement of $T$. Therefore the experimentalist will minimize it, covering the surface with a thin coating of high emissivity in the infrared spectrum (typically dull black paint, for which $\varepsilon$ = 0.95 - 0.98).

Most often the model to be imaged by the radiometer is located in a test section provided with windows. These optical accesses should have high transmittance in the infrared spectrum: good candidates are sapphire, germanium and zinc selenide. Nevertheless, due to absorption phenomenon, these windows will yield signal attenuation. This is why it is necessary to calibrate the whole measurement chain in the experimental configuration. This can be achieved by using thermocouples flush mounted on the model, and correlating the output of the IR radiometer (object signal) to the measured temperature.

Further details on infrared thermography and its application for convective heat transfer measurements can be found in Gaussorgues (1994), Astarita et al (2000) and Buchlin (2009).

### 4.4.2 – Experimental apparatus and procedure

In the present work IR thermography is employed to measure temperature distributions along the rib-roughened wall (standard configuration) in the conjugate heat transfer regime. The measurements have been performed in the frame of the Short Training Program of Manfredi Scialanga at VKI (Scialanga (2009)).

IR thermography is preferred here to TLC thermography: since in this case the conduction through the wall needs to be accounted for, the temperature measured on the wet surface has to be associated with a single value of heat flux imposed on the outer wall side. The wall temperature varies spatially by about 15 K along the rib-roughened surface, and only very wide band TLC would allow a simultaneous color display on the whole area. However, wide band TLC only guarantee accuracy within around ± 1 K. IR thermography on the other hand allows for errors comparable to narrow band TLC (in the order of ± 0.1 K).

Thermal maps are obtained in the central part of the rib-roughened wall: this is exchangeable, and can be of stainless steel, Inconel or ceramoplastic, in order to study the effect of the solid-to-fluid thermal conductivity ratio $K$. The central part of the ribbed wall (from the $5^{th}$ to the $9^{th}$ rib, Fig. 4.22) is the only area of the test section where the conjugate heat transfer process takes place. Such choice is discussed in subsection 4.4.3.

Figure 4.23 (left) schematically displays the configuration for the IR thermography. A uniform heat flux boundary condition is generated by dissipating DC power into a 25 μm thick foil of Inconel 600, glued to the outer side of the rib-roughened wall. Any electrical contact between the Inconel foil and the ribbed wall (which could occur when using the ribbed walls of metallic material) is avoided by sheathing the heating foil between two sheets of Mylar (each 0.1 mm thick). The heat losses are minimized by placing underneath the heating element a 40 mm thick slab of insulating foam (*TAUfoam*). The losses evaluation is quantified by means of seven K-type thermocouples placed at both sides of the insulating slab. The

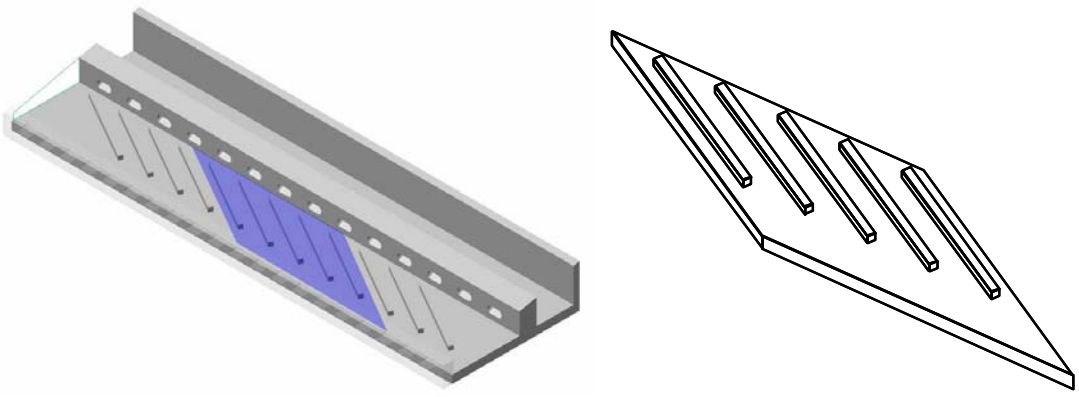

**Fig. 4.22** **Interchangeable central part of the rib-roughened wall: test section with the five central domain highlighted (left), and close up on the piece (right)**

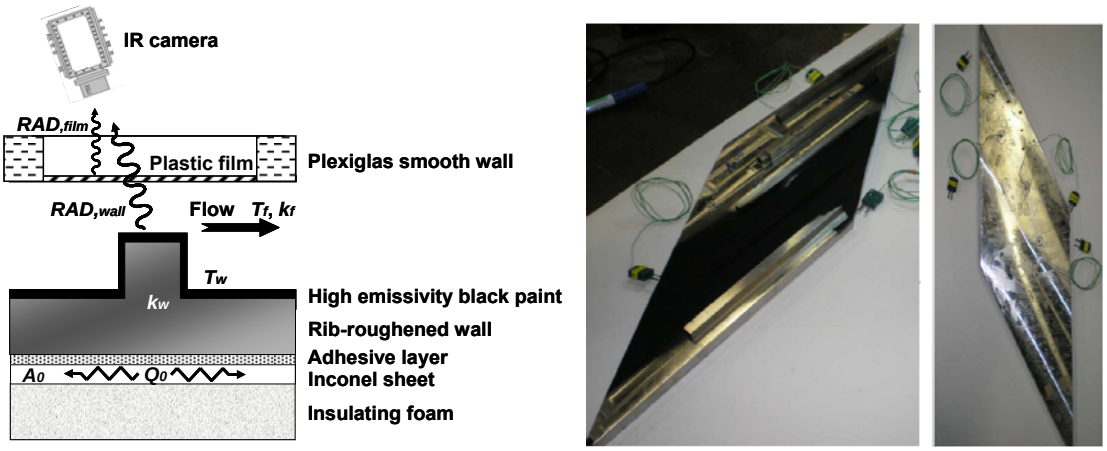


**Fig. 4.23** **Infrared thermography: measurement layout (left); view of wet side and outer side of the ribbed slab machined out of Inconel 625 instrumented with 4 thermocouples (right)**

investigated domain, located in the centre of the cavity, consists of one rib (the 7$^{th}$) and the adjacent floor. The target surface is painted with dull black paint from Mankiewicz GmbH, which has a nominal emissivity of $\varepsilon = 0.98$. The layer has a thickness of about 50 microns. Figure 4.23 (right) shows the rib-roughened slab machined out of Inconel 625.

The used IR camera is a FLIR SC 3000 with an FPA of 320 by 240 elements. It works at wavelengths between 8 and 9 μm and is cooled by a Stirling engine. It outputs thermograms of the object signal in 14 bit. The nominal value of thermal sensitivity provided by the producer is 0.02 K, but tests carried out observing an isothermal surface suggests that the NETD is 0.05 K at 30°C. The detector has an IFOV of 1.1 mrad: at the minimum focus distance of 0.3 m, this translates in a spatial resolution of about 0.3 mm. During the present measurements the achieved spatial resolution ranges from 0.5 to 1.2 mm, depending on the investigated surfaces; the lateral sides of the ribs are inevitably penalized as they appear skewed by the perspective.

The optical window fitted in the Plexiglas wall is 170 by 400 mm$^2$: a smaller window would have made unfeasible the visualization of the investigated ribbed domain. Rigid windows of IR-transparent material (e.g. in germanium or zinc selenide) of this size are not available: therefore a transparent polyethylene film is used. Since the channel operates above atmospheric pressure, the film tends to be deformed during the tests. A system of movable bars hinged to the Plexiglas smooth wall is exploited to minimize the film deflection, without impeding the optical access for the different camera positions. Maximum film deflection is estimated to be 3 mm (less than 2% of the smaller side of the window), and its influence is considered negligible for the development of the flow pattern. This is verified by performing a hot test with a full Plexiglas wall and recording the temperature of the heated plate via 4

K-type embedded thermocouples: discrepancies below the experimental uncertainties are found with respect to the case in which the plastic film is used.

An in-situ, pixel-by-pixel calibration is performed. This has several advantages with respect to the classic single-point calibration. In the latter, the object signal relative to a precise reference point of the test surface is associated to the temperature measured by an embedded thermocouple. If the thermocouple is located at the very reference point, then the calibration is virtually free from errors. However, covering the whole investigated surface with embedded thermocouples is unfeasible in the present case, especially because doing so would alter the conduction through the wall. So the calibration curve obtained for the reference point should be used for the entire surface. This entails possibly large errors, especially for areas viewed by the camera under different angles with respect to the reference point. Even larger inaccuracies can occur in areas which are not in focus; this is unavoidable when the test surface is far from being perpendicular to the optical axis. For the considered geometry, multiple surfaces of different orientation need to be imaged at the same time, and most of them under a non-optimal view angle (see Fig. 4.24). Therefore a pixel-wise calibration is preferred, which eliminates the need of embedding thermocouples in the investigated portion of the test surface, and takes into account the effects of variable angle of view and out-of-focus imaging. The calibration procedure is described in the following.

Using the heat exchanger upstream of the channel, the air is brought at a given temperature level (controlled by a thermocouple at the inlet section). The target surface is streamlined by the air flow until isothermal conditions are achieved. The wall temperature is checked by 4 K-type thermocouples inserted at 0.5 mm below the wet surface, at locations far enough from the investigated domain not to alter the heat conduction through the conductive wall. Once the isothermal condition is achieved within ±0.5 K, a thermogram of the surface is acquired. The procedure is repeated for several (seven to ten) temperature levels, and the data points are fitted with a second

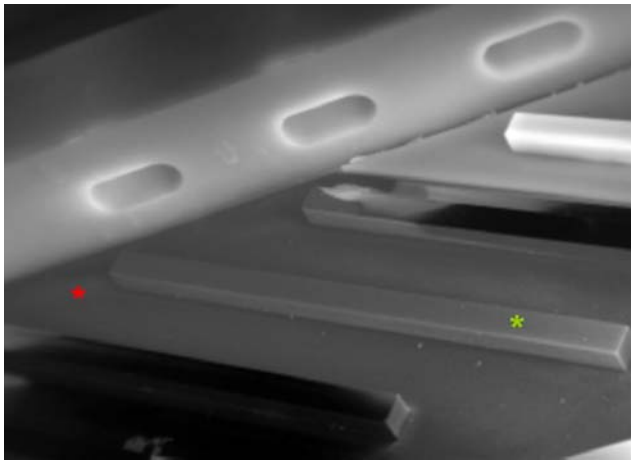

**Fig. 4.24** **Thermogram of the ribbed slab in isothermal condition. The skewed view angle prevent from having an optimal focus over the whole area of interest**

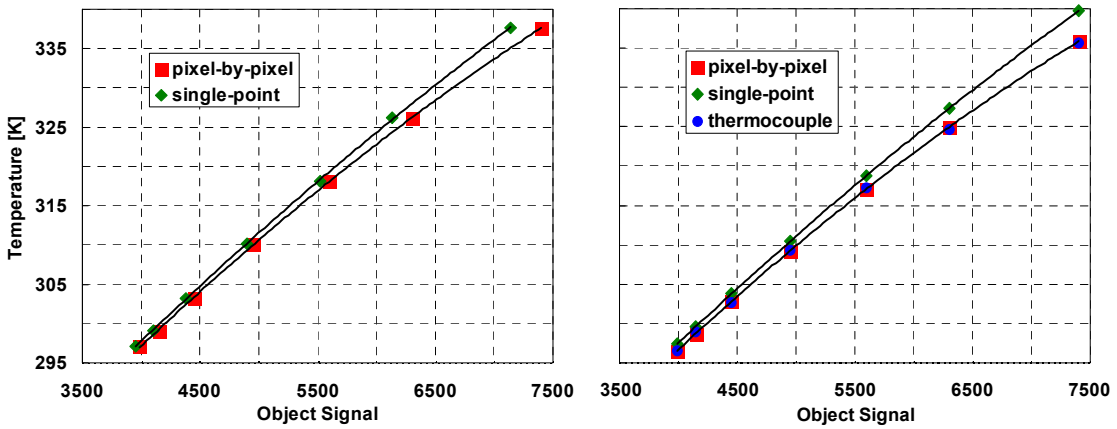


**Fig. 4.25** **Calibration of the IR camera. On the left: comparison between the calibration curve obtained by single-point approach and the curve obtained by pixel-wise approach on a point not in focus. On the right: crosscheck of the two approaches against local thermocouple values**

order polynomial. A calibration curve is obtained for each pixel, correlating the object signal recorded by the IR radiometer with the wall temperature.

When the FPA is kept almost parallel to the considered test surface, the calibration curves obtained with the single-point approach and the pixel-wise approach are indistinguishable. When using more skewed angles of view (needed for imaging the three-dimensional domain), the single-point calibration leads to errors in excess of 1 K in regions far from the reference point (which are inevitably out of focus). This is shown in Fig. 4.25, which presents a comparison of the two approaches applied to the thermogram in Fig. 4.24: the single-point calibration curve is displayed in Fig. 4.25 (left) and is obtained on the point marked by the green star in Fig. 4.24, which is in focus and corresponds to an embedded thermocouples inserted 0.5 mm below the surface. The calibration curve obtained with the pixel-wise approach is also shown in the same chart: it is obtained for the point marked by the red star in Fig. 4.24, which is also located in correspondence of an embedded thermocouple, and is not in focus. The two calibration curves differ significantly (especially at high temperatures). Figure Fig. 4.25 (right) displays a crosscheck between the values read by the thermocouple corresponding to the red star and the surface temperature values obtained applying both calibrations to the local object signal: in the temperature range of interest (305 to 320 K), the single-point approach gives errors larger than 1.5 K; the pixel-wise approach on the other hand leads to maximum discrepancies of 0.25 K, which are attributable to the imperfect isothermal condition of the slab during calibration.

When the calibration is completed, the heater is switched off and the heat flux is imposed via the Inconel foil, without moving the camera. Typical heat flux levels are of the order of 1500 $Wm^{-2}$, for wall surface temperatures ranging between 305 and 320 K. Once the steady state is reached (as verified by the thermocouples in the flow and within the slab), ten thermograms are grabbed within a few seconds and averaged, in order to reduce the noise due to ambient radiation.

During calibration the film is streamlined by the heated air, therefore the temperature of the polyethylene film is higher than during measurement. However the additional radiation emitted by the window is accounted for: in a separate experiment the film temperature is varied by means of a heat gun, while keeping constant the ribbed wall temperature; the variation of the object signal when looking at the wall (through the film) is correlated to the film temperature, controlled by four surface thermocouples, for different wall temperature levels. The relation between object signal and film temperature turns out to be highly linear, with a proportionality coefficient only slightly varying for different wall temperatures; this confirms that the transmissivity of the polyethylene film is practically constant within the considered temperature range.

The geometry of the ribbed wall does not allow acquiring a single thermogram of the whole investigated surface. Three separate infrared images are grabbed, which allow imaging with sufficient resolution the five streamlined faces of the rib: the three long rectangular faces (the tip and the two lateral sides) and the two small square faces. The object signal distribution over the investigated domain is reconstructed via a MATLAB® routine which performs:

- the projective transformation of the images
- the cropping of the different faces of the rib
- the determination of the calibration curves for each pixel of the thermogram
- the application of the calibration curves to obtain the temperature maps

The code is provided with a graphical user interface.

### 4.4.3 – Justification of the experimental strategy

In order to be fully adherent to the engine reality, the whole model should be made out of conductive material. However this would engender unacceptable costs of the material and very long manufacturing times, impeding any optical access. The choice of limiting the area of investigation to the central part of the ribbed wall is based on the assumption that the thermal pattern on the ribbed wall is not appreciably affected by the conduction through the rest of the channel walls (namely the opposite smooth wall, the mid-wall and the exit wall). This is verified by means of a finite-element analysis performed on a 2D model of the cavity discretized in about 7,800 elements (Fig. 4.26): a constant piecewise heat transfer coefficient distribution (derived from convective results presented in Chapter 6) is imposed along the streamlined walls, where also radiation is accounted for; uniform heat flux is imposed on the outer side of the cavity. A fully conductive (Inconel) and fully heated case is compared with a configuration where only the rib-roughened wall is conductive and heated, the remainder of the section being in Plexiglas: differences below 2% are found for the wall heat flux and below 3% for the temperature head along the ribbed wall,

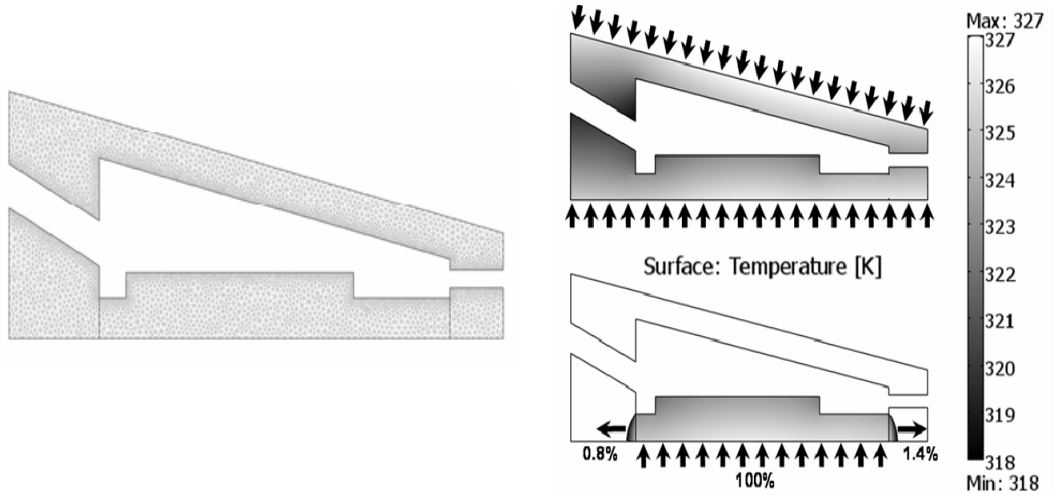


**Fig. 4.26** **2D FEM model of the heated cavity. Left: discretized domain. Right: resulting thermal distribution for the fully conductive, fully heated configuration (top) and for the configuration with only the ribbed wall conductive and heated (bottom)**

substantiating the present experimental approach. The total heat losses at the Inconel-Plexiglas interface are about 2%.

### 4.4.4 – Heat transfer evaluation

The heat transfer performance in conjugate regime is quantified in terms of non-dimensional temperature and Nusselt number. The former is defined as:

$$\Theta = \frac{A_0 k_f (T_w - T_f)}{Q_0 D_{mid}} \tag{4.15}$$

where $T_w$ is the wall temperature measured by IR thermography and $Q_0$ is the imposed power heat going through the conductive slab:

$$Q_0 = Q_{Joule} - Q_{cond} \tag{4.16}$$

$Q_{Joule}$ is the power produced by dissipating the current $I$ due to the potential $V$ (see Eq. 4.8) and $Q_{cond}$ is the conduction loss. $A_0$ is the area of the foil portion across which $V$ is established. $T_f$ is defined to be equal to the flow temperature in the inlet section (consistently with the convective case, section 4.3.5). The hydraulic diameter of the mid-wall slot is taken as reference length, as the jets impingements are the dominant feature for the aero-thermal performance.

The Nusselt number is written as:

$$Nu = \frac{q_w D_{mid}}{k_f (T_w - T_f)} \tag{4.17}$$

where $q_w$ is the local wall heat flux. Evaluating $q_w$ implies solving the conduction in the solid; this is done with a three-dimensional numerical model representing a single ribbed domain, by means of the finite element software COMSOL Multiphysics®: conduction is solved on an unstructured mesh of about 252,000 elements (Fig. 4.27). Further mesh refinement does not affect significantly the solution. To solve the problem directly, the following thermal boundary conditions are imposed as follow (Fig. 4.28):

- wall temperature along the ribbed surface (by interpolation of the experimental data using cubic Hermite splines)
- uniform heat flux along the outer side
- adiabatic wall condition along the lateral sides aligned with the *y*-axis
- periodic heat flux condition along the lateral sides virtually in contact with the contiguous domains

The direct approach (measured temperature imposed on the wet surface) does not appear as a viable solution in the present case, as the heat flux computed on the rib-roughened wall is dramatically sensitive to the imposed wall temperature. The unavoidable inaccuracies associated with the measurements induce large over- and under-shoots in the calculated derivative of the solid-wall temperature. As an example, Fig. 4.29 (top) displays the heat transfer coefficient distribution on the non-impingement side of the rib for the wall in ceramoplastic, as computed by the direct approach: non-physical negative values of wall heat flux appear over about one third of the considered surface. The problem is even more severe for the materials of higher thermal conductivity, as in these cases the temperature variation on the wet surface is smaller, and the incidence of the error is more important.

The problem is overcome by substituting the Dirichlet boundary condition with a Robin boundary condition: the conduction is solved iteratively and the false position method (Chapra and Canale (2005)) is applied. As illustrated in the diagram in Fig. 4.30, for each grid point of the wet surface two values of heat transfer coefficient are given, $h_1$ and $h_2$, one larger and one smaller than a reasonable estimation of $h$. The true value $h^*$ is therefore comprised between them, i.e.: $h_1 < h^* < h_2$. By FEM calculation two values of local wall temperature are obtained, $T_1$ and $T_2$. The experimental value of temperature $T^*$ will evidently satisfy $T_2 < T^* < T_1$. The guess of heat transfer coefficient is obtained using the formula of the secant:

$$h' = h_1 + \frac{(h_2 - h_1)}{(T_2 - T_1)}(T^* - T_1) \tag{4.18}$$

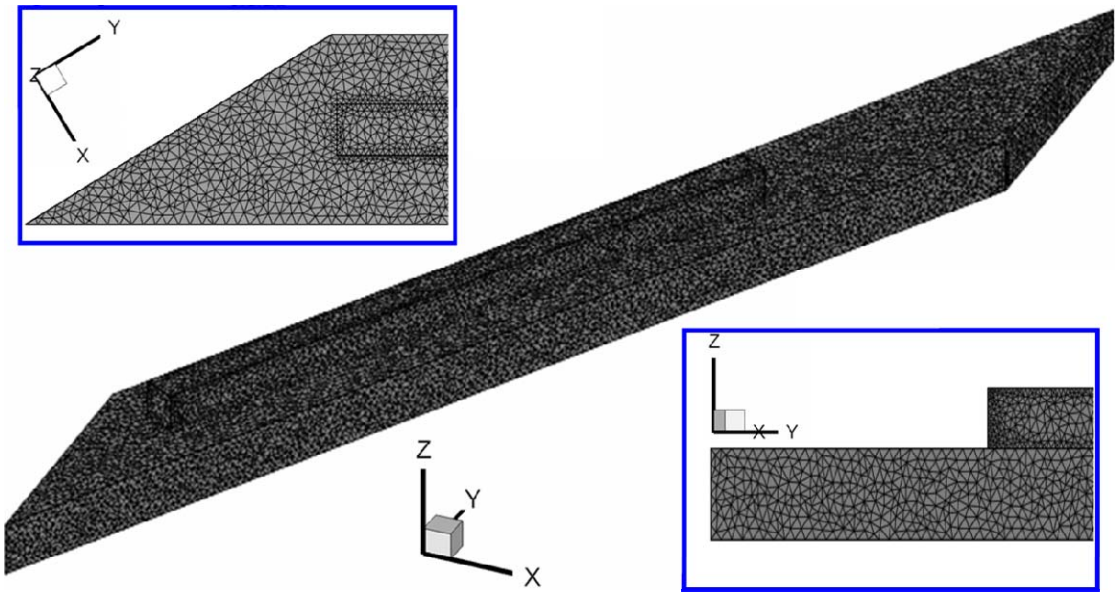


**Fig. 4.27** **Mesh of the numerical model for solving wall conduction. In the boxes: close-up view from the top and from the side**

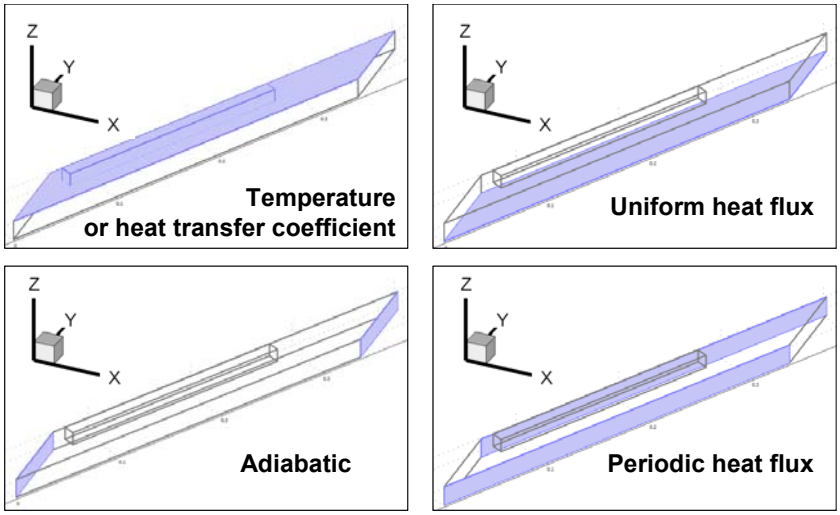


**Fig. 4.28** **Thermal boundary conditions imposed on the numerical domain**

Using $h'$ as an input, the surface temperature $T'$ is obtained by FEM calculation and compared with $T^*$: if $T' < T^*$, then the two extremal points become $h_1$ and $h'$; otherwise these will be $h_2$ and $h'$. The process is repeated until the computed temperature distribution and the target temperature (i.e. the measured temperature $T^*$) differ by a quantity smaller than a tolerance $\delta$ for each point of the surface. $\delta$ is taken as the average uncertainty associated with the measurements (i.e. 0.5 K, as detailed in

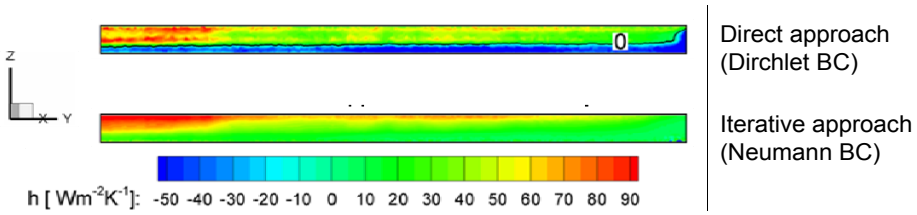


**Fig. 4.29** **Contours of heat transfer coefficient along the non-impingement side of the rib for the wall in ceramoplastic: direct (top) and iterative approach (bottom)**

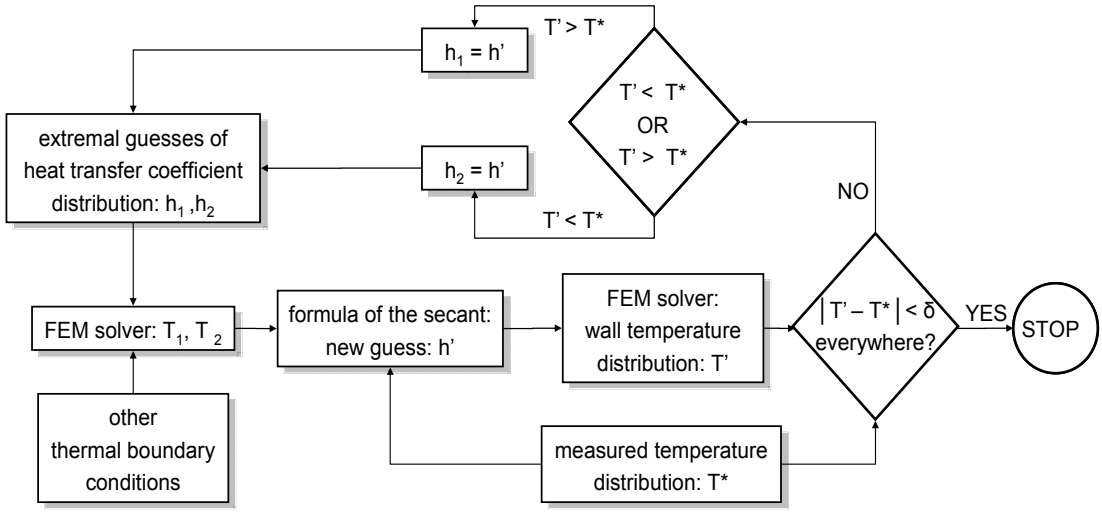


**Fig. 4.30** **Schematic of the iterative procedure for the evaluation of the heat transfer coefficient by application of the false position method**

the next paragraph). The condition for convergence is that the wall temperature must decrease monotonically with increasing heat transfer coefficient, which is physically sound. The heat transfer coefficient distribution computed with the iterative approach on the non-impingement side of the rib for the wall in ceramoplastic is reported in Fig. 4.29 (bottom): the contours are smoother, and most importantly the values of $h$ are strictly positive everywhere.

The proposed approach is similar to the scheme applied by Lin et al. (2001), who faced a transient conduction problem and iterated on the response time of the surface temperature. In the present case convergence is attained in about 10-20 iterations, depending on the starting guess for $h$ and on the material conductivity, requiring no more than 3 hours of CPU time on a single processor (2.1 GHz). The iterative procedure is implemented in MATLAB®, in a routine which calls the FEM solver, exploiting the COMSOL/MATLAB interface. This method is validated using as target $T^*$ the temperature distribution obtained numerically from imposing a synthetic map of heat transfer coefficient $h^*$ on the wet surface of the domain: starting from two

distributions of uniform heat transfer coefficient $h_1$ and $h_2$ as extremal guesses of $h$, convergence is attained (within the tolerance $\delta$ = 0.5 K) in 13 iterations, and the correct distribution of heat transfer coefficient $h^*$ is retrieved within a maximum error of 5%.

Since the outcome of the procedure is the local heat transfer coefficient, the actual definition of $Nu$, rather than Eq. 4.20, is the following:

$$Nu = \frac{hD_{mid}}{k_f} \tag{4.19}$$

### 4.4.5 – Uncertainty of the conjugate heat transfer measurements

As for the convective heat transfer measurements, the estimations are based on a 95% confidence interval and are determined following the approach of Kline and McClintock (1953) and Moffat (1988). However, when is felt that the mutual independency of the different sources of error is not clearly assessed, a more conservative estimation is given summing up the absolute values of the different errors. Details on the calculation of the uncertainty are given in Appendix A.

The uncertainty associated to the non-dimensional temperature mainly depends on the generated by Joule effect $Q_{Joule}$ is measured with an uncertainty of about ±1%. The conductive loss is less than $0.01Q_{Joule}$, so the uncertainty on $Q_0$ is conservatively assumed as ±0.02 $Q_{Joule}$. The main sources of error for the wall temperature measurements are the non perfect isothermal condition achieved during calibration and the uncertainty on the plastic film temperature. Uncertainties of ±0.15 K are associated to the temperature measurements by means of thermocouples. During calibration, the wall temperature non-uniformity varies ranges from ±0.3 to ±0.5 K, depending on the material used for the ribbed wall. Temperature variations of ±1 K are possible along the plastic film: given the influence of the window temperature, this may result in additional errors of ±0.2 K for the wall temperature. Overall the uncertainty on the wall temperature is estimated as 0.5 K. Given the wall temperature levels and the magnitude of the imposed heat flux, the relative experimental uncertainty on Θ ranges between 5% and 9%, depending on the surface temperature.

The uncertainty associated to the measurement of the Nusselt number is harder to compute, as the local heat flux is the result of a finite element calculation. If local temperature variations of the order of the uncertainty on the wall temperature uncertainty (±0.5 K) are added to the target temperature, these result in maximum variations of 12% of the computed local value of heat transfer coefficient. Considering an additional error of 5% related to the iterative procedure (as mentioned in the previous section), an uncertainty of 13% is assumed for the Nusselt number in conjugate regime.

The uncertainty on the value of the wall thermal conductivity used in the finite element calculations is estimated as ±0.1 $Wm^{-1}K^{-1}$ for Inconel 625 (which is a standard reference material) and ±0.2 $Wm^{-1}K^{-1}$ for the used grade of ceramoplastic (as

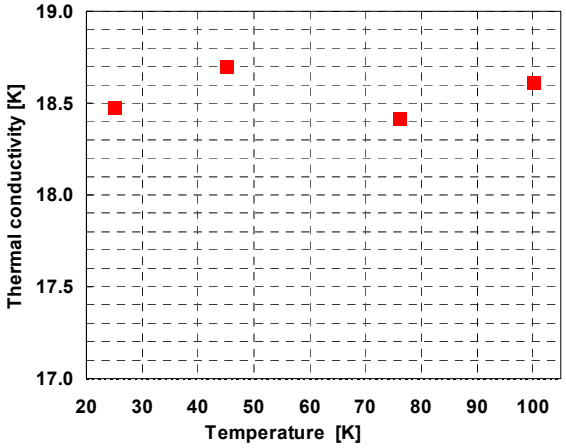


**Fig. 4.31** **Measured values of thermal conductivity for the slab of AISI 304 used in the conjugate heat transfer investigation. Analysis performed by the Metallurgy and Metallic Material Science Laboratory, University of Liege (Belgium)**

declared by the producer). Uncertainty on the conductivity of stainless steel is typically larger; to increase the accuracy a sample of the slab was analyzed by the Metallurgy and Metallic Material Science Laboratory of the University of Liege (Belgium). The applied methodology is based on the thermal excitation of the sample surface using a pulsed laser beam, and the subsequent measurement of the temperature response of the surface. The result of the analysis is displayed in Fig. 4.31. The value of 18.5 $Wm^{-1}K^{-1}$, obtained in the range of interest, is 10% higher than the standard value of 16.2 given by the producer. This put in evidence the need of accurately assessing the thermal properties of common materials when they are used for scientific investigation. The results provided by the University of Liege are considered accurate within ±0.2 $Wm^{-1}K^{-1}$. Overall the uncertainties on the conductivities of the utilized materials do not affect appreciably the results of the FEM solution.

## *4.5 – Additional measurement techniques*

### 4.5.1 – Pressure measurement

The pressure measurements are carried out by means of differential, variable reluctance pressure transducers Validyne® DP45 (Fig. 4.32, left) equipped with different membranes, according to the expected pressure range. The samples are acquired by means of a 16 bit A/D converter. When acquiring from the 34 pressure taps drilled in the channel slots, a Scanivalve system is used (Fig. 4.32, right). The transducers are calibrated periodically against a water manometer. The uncertainty associated to the pressure transducers is ±3 Pa.

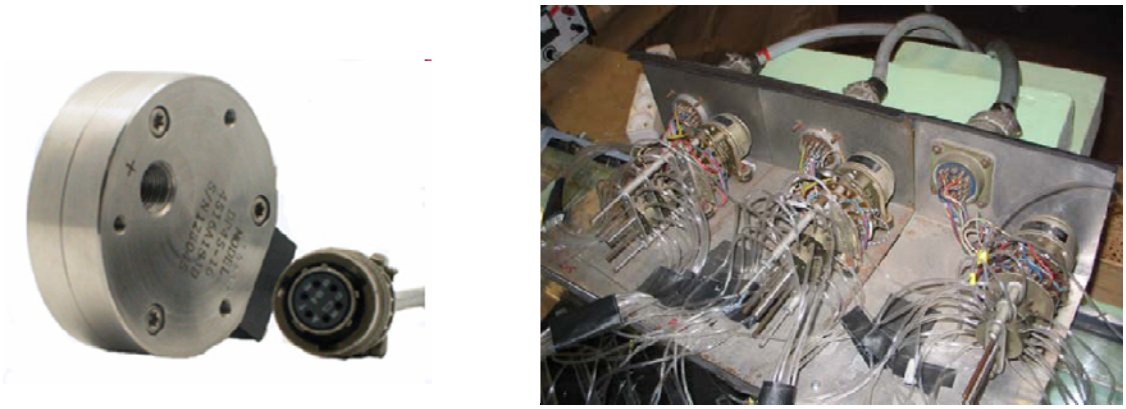

**Fig. 4.32** **Left: Validyne differential pressure transducer DP45. Right: Scanivalve switch system**

### 4.5.2 – Surface streamline flow visualizations

In the configurations not studied by PIV (i.e. the configuration without ribs and the three non-standard ribbed configurations) some insight in the flow field is gained by means of surface-streamline flow visualizations. Three visualization techniques are used: the ink dots technique, the wool tufts technique and the oil film technique. In these methods, a qualitative interpretation of the flow field is drawn from the observation of patterns generated by the flow streamlining the surfaces of the channel walls. The techniques employed here, along with many others, are reviewed by Merzkirch (1987).

The ink dots technique provides a permanent record of ink-traces that show surface-streamline direction and shape, and it is suited for low speed gas flow (Langston and Boyle (1982)). In the present case grids of ink dots are marked on sheets of graph paper which are attached to the internal sides of the channel. The ink giving the best results turns out to be the one from pens Staedtler®, type LumoColor Permanent. A film of solvent (methyl salicylate) is applied with an airbrush all over the dotted area. When air is blown in the model the solvent is subjected to wall shear stress and the ink dots streaks over the surface, giving an image of the surface-streamlines.

The wool tufts technique is also suitable for low-speed gas flows (Carbonaro (1994)). It does not provide a permanent record of the streamline direction, so a video-recording of the experiment is needed. Wool tufts are glued on the streamlined walls, and the direction of their fluttering is associated to the local flow direction. A violent agitation of the tufts or a tendency to lift from the surface may indicate a separate regime. The length of the tufts needs to be carefully chosen: too long tufts are too heavy to follow the stream; on the other hand too short tufts are too stiff to be guided by the flow.

The oil film technique is not suited for very low velocity flows (below 10 m/s) and indeed, in the frame of the present study, it is only used in the region of direct jet impingements. The oil mixture is obtained with a mix of talcum powder and titanium dioxide, emulsified with petrol and few droplets of lamp oil.

Figure 4.33 displays two snapshots obtained exploiting wool tufts technique on the ribbed wall of the standard configuration and ink dots technique on the non-impingement wall of the configuration without turbulators.

As the results are qualitative, there is no uncertainty evaluation associated to them. However the mean flow models deduced by flow visualizations are consistent with the thermal pattern displayed by liquid crystal thermography; the latter can actually be regarded as a powerful flow visualization tool for convective flows.

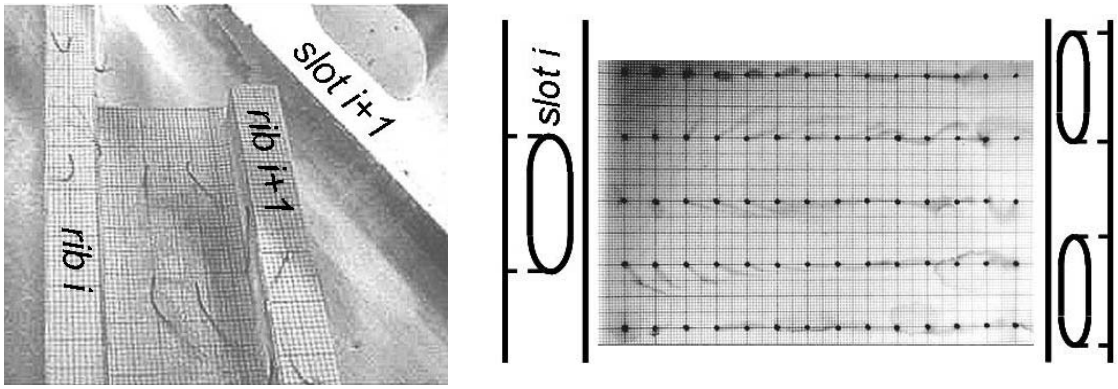


**Fig. 4.33** **Flow visualizations obtained by wool tufts glued on the ribbed wall of configuration *G3* (left) and by ink dots applied on the floor of the non-ribbed configuration (right)**

# Chapter 5 – Aerodynamic investigation

In the present chapter the results of the aerodynamic study of the cooling channel in object are reported.

The static pressure in the mid-wall slots and exit slots is presented for the standard ribbed configuration, along with the dynamic pressure (translated into velocity level) at the outlet of the cavity. The pressure drop across the test section and the influence of the rib insertion is assessed.

The results of the PIV campaign performed on the standard rib-roughened configuration are described for each measurement plane in terms of mean velocity and *rms*, which allows understanding and characterizing the main flow features.

Mean flow models are presented for the standard rib-roughened configuration, based on the PIV results; for the other studied geometries (configuration without ribs and configurations with shifted/tapered ribs) mean flow models are deduced from the surface-streamline flow visualizations.

As stated in Chapter 3, all experiments are carried out for a constant Reynolds number of 67500. As the regime is fully turbulent, no significant change is expected to take place for variations of Reynolds number within the range of practical interest.

## *5.1 – Results of the pressure measurements*

### 5.1.1 – Pressure distribution along the channel

Figure 5.1 displays the distribution of static pressure along the row of mid-wall slots and exit slots, as felt by the pressure taps drilled in each slot. It is reminded that the taps are drilled at half length of the slot. The measured static pressure $P_s$ (relative to ambient pressure $P_{amb}$) is normalized with the dynamic pressure at the inlet of the test section:

$$P_{norm} = \frac{P_s - P_{amb}}{\frac{\rho U_b^2}{2}} \tag{5.1}$$

Excluding the first two and the last two extremal slots, which are obviously affected by side-wall effects, the variation of static pressure along the row of mid-wall slots is below 4% of the average level, as anticipated in Chapter 3 (section 3.3). As for the row of exit slots, the mean value of the normalized static pressure is less than 5 Pa, with a seemingly random scatter of about ±6 Pa. As these values are of the order of the measurement uncertainty (±3 Pa), it is concluded that the static pressure in the exit slots, at the location where the taps are drilled, is negligibly different from the ambient

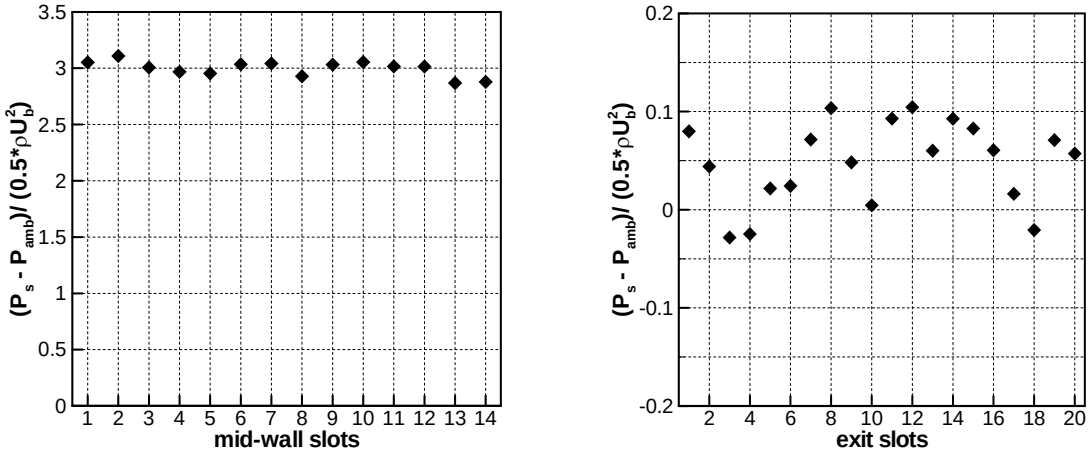


**Fig. 5.1** **Normalized static pressure along the row of mid-wall slots (left) and exit slots (right)**

pressure. It is clear that the pressure drop across the exit slots is concentrated at the entrance of the holes, and therefore the tap at mid-length is not feeling an appreciable static pressure difference with respect to the ambient.

### 5.1.2 – Pressure drop

In order to assess the aerodynamic performance of a cooling scheme, the pressure drop is to be evaluated. For channel flows, this is typically expressed in terms of the friction factor *f*, which is defined by the Darcy-Weisbach equation (Landau and Lifschitz (1987)):

$$\Delta P = f \frac{L}{D} \frac{\rho U^2}{2} \tag{5.2}$$

in which the pressure drop $\Delta P$ is related to the length-to-hydraulic diameter ratio and to the dynamic pressure. When the geometry is rib-roughened, in order to determine the penalty due to the obstacles insertion, the friction factor ratio $f/f_0$ is often computed, $f_0$ being the friction factor for the configuration without ribs.

In the present case the definition of friction factor is not obvious, since the considered configuration substantially differs from a conventional, tubular channel: in the present cavity, quantities such as the length and the diameter (with respect to the flow direction) cannot be identified unambiguously.

To the author's best knowledge, the only geometry in literature resembling the present one is the one studied by Taslim et al. (1998). To qualify the pressure drop, Taslim et al. defined a percentage of pressure recovery as follow:

$$PR = 100 \frac{\frac{\rho U_{exit}^2}{2}}{P_{\text{supply}} - P_{amb}} \tag{5.3}$$

where $U_{exit}$ is the average exit slot velocity, and $P_{supply}$ is the pressure in the settling chamber upstream of the test section. Taslim et al. investigated several rib arrangements at different Reynolds numbers. For the case most similar to the present, they found values of pressure recovery of 17% for the geometry without ribs, and only a minimum penalty due to the rib insertion ($PR$ = 15%). For the geometry analyzed in the present thesis the pressure recovery for a non-ribbed configuration is 37%, and is practically unchanged by rib insertion. The conclusion to be drawn is that, for this type of cooling scheme, the pressure drop is mainly concentrated across the mid-wall slots, and is virtually not affected by the rib insertion, at least in the considered range of geometrical parameters. The large dissimilarity of pressure recovery levels with respect to Taslim et al. seems to depend on the geometrical differences between the two studies. Indeed Taslim's Reynolds number at the mid-wall-slots exceeded 50000, against 18500 in the present case, although the inlet section Reynolds numbers are comparable (52000 for Taslim, 67500 here): for the same total mass flow, larger Reynolds number at the mid-wall slots corresponds to a smaller hydraulic diameter of the holes, and hence to higher pressure drop.

Another cooling scheme which bears some similarity with the present case is the one of Choi et al. (2008), who studied three chambers separated by two perforated inserts and followed by a cutback trailing edge with slot ejection. The authors measured the static pressure at several locations in the different chambers, and defined a local pressure coefficient:

$$C_P = \frac{P_s - P_{amb}}{\frac{\rho U_{exit}^2}{2}} \tag{5.4}$$

They defined the Reynolds number at the exit slots, and investigated the range 5000-30000; in the present case the exit slots Reynolds number is about 16000. For the case more comparable to the present ($Re$ = 20000), Choi et al. (2008) found chamber-averaged pressure coefficients of 1.5 in the first chamber, 0.7 in the second one and 0.2 in the third one. In the present configuration, no pressure taps are drilled in the trailing cavity itself; however, given the little variation of the static pressure readings along each row of slots, one can assume that a good estimation of the average static pressure in the trailing cavity is:

$$P_{s,avg} = \frac{P_{s,mid,avg} - P_{s,exit,avg}}{2} \approx \frac{P_{s,mid,avg} - P_{amb}}{2} \tag{5.5}$$

where $P_{s,mid,avg}$ and $P_{s,exit,avg}$ are the static pressure value averaged along the two row of

slots. Using this value of static pressure, the average pressure coefficient in the trailing cavity is $C_P$ = 0.65. Anyway, a direct comparison with Choi et al. (2008) is made difficult by the evident geometrical differences.

### 5.1.3 – Exit slots velocities

The dynamic pressure is measured at the centerline of the outlet section of each exit slot by means of a Prandtl tube: the corresponding velocity levels (normalized with the bulk velocity at the inlet of the test section) are plotted in Fig. 5.2 (left). Excluding again the two pair of extremal slots, the velocity variation along the row of exit slots is within 6% of the average level. Together with the static pressure distribution along the row of mid-wall slots, this result confirms that, from an aerodynamic standpoint, the central ribbed domains can be considered representative of most of the channel.

The velocity map obtained traversing the Prandtl probe at the outlet section of the 12$^{th}$ exit slot is presented in Fig. 5.3. The velocity maps for the 11$^{th}$ and 13$^{th}$ slot display differences well within the uncertainty, and are not shown. As one can see the profile shows good symmetry both in the *y*- and the *z*-directions. The mass flow calculated integrating the velocity over the slot section exceeds by only 2% the nominal value obtained assuming an equal distribution along the slots row. Therefore the reported velocity profile is considered representative of most of the exit slots, although the extremal slots will be affected by the effect of the side walls.

## *5.2 – Results of the PIV measurements*

The flow field in the standard rib-roughened configuration is characterized by means of PIV along the planes outlined in Chapter 4 (section 4.2.3). In the following,

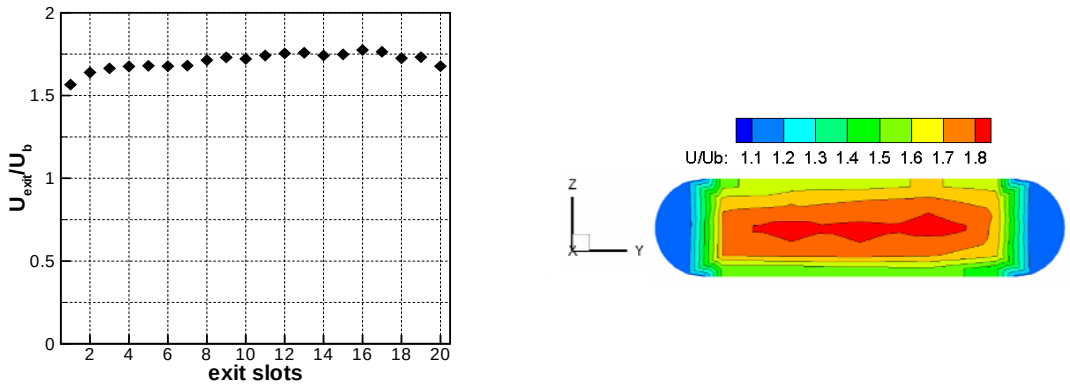


**Fig. 5.2** **Normalized velocity of the exit slots: centerline values along the row of slots (left) and velocity map at the outlet section of a central slot (right)**

the PIV results are presented in terms of mean velocity and *rms* of the velocity fluctuations, providing a description of the main flow features. This eventually allows reconstructing a three-dimensional mean flow model, which is presented in section 5.5. The link between the flow structures and the heat transfer will be drawn in Chapter 6.

As for the notation, $U$, $U'$, $U''$, $V$ and $W$ are the mean velocity components along the axes $x$, $x'$, $x''$, $y$ and $z$, respectively, while $u$, $u'$, $u''$, $v$ and $w$ are the correspondent velocity fluctuations. The *rms* of the velocity fluctuation $u_i$ is:

$$rms(u_i) = \sqrt{\overline{u_i^2}} \tag{5.7}$$

where the overbar indicates the ensemble average (i.e. average over the 1000 realizations of each sets).

As illustrated in Chapter 4, the PIV measurement planes are concentrated between the 6$^{th}$ and the 8$^{th}$ ribbed domain; index $i$ refers to the 7$^{th}$ rib and/or slot.

### 5.2.1 – Crossing-jets

The crossing jet issued by slot $i$ is characterized by means of PIV in planes $x'y$ and *xz_core_i* (refer to Fig. 4.2 for the nomenclature of the planes). Contour plots of ensamble-averaged in-plane velocity, streamlines and *rms* contours in plane $x'y$ are presented in Fig. 5.3. The contour values are normalized by the bulk flow velocity $U_b$ at the inlet of the test section (see Fig. 3.1). Both velocity levels and streamline paths highlight an important unbalance of the crossing jet: due to the 90° turning of the flow coming from the inlet channel, the mass flow is mainly concentrated in the right side of the slot span. The maxima of the *rms* correspond to the strong shear at the boundaries of the jet. Sources and sinks in the streamlines pattern suggest that the inter-slot area is characterized by strongly three-dimensional flow.

In order to better characterize the jet, profiles in the plane $x'y$ are extracted along a line at one rib height from the mid-wall (Fig. 5.4). The abscissa $Y$, which is aligned with the $y$-axis, is 0 at the left edge of slot $i$ and 1 at the right edge. The peak stream-wise velocity of the core is 50% higher than the average jet velocity obtained assuming the same uniform velocity in every slot (which is 5% higher than the bulk velocity at the inlet). Taking the maxima of *rms(u')* and *rms(v)* as boundaries of the jets, the effective span-wise dimension of the latter is quantified as 45% of the slot span. At both jet boundaries, *rms(u')* is about 30% higher than *rms(v)*.

Figure 5.5 shows a three-dimensional view of the mean velocity (contours and streamlines) in the two planes that are used to characterize the crossing jet, *xz_core_i* (vertical plane at $Y$/(slot span) = 0.75) and $x'y$. The flow issued by the mid-wall slot appears well aligned with the slot axis; the velocity magnitude is evenly distributed in $z$-direction. The streamlines pattern suggests that part of the jet produced by slot $i$ impinges on rib $i$ and enters the inter-rib region (i.e. the volume comprised in between rib $i$ and rib $i+1$). The rest of the mean streamlines partly impinges on rib $i-1$, and

partly streams over it and flows in *x*-direction (likely impinging on rib *i-2*). Above the jet, the flow is organized in a complex recirculation zone characterized by low in-plane velocity, where two different vortical structures can be identified.

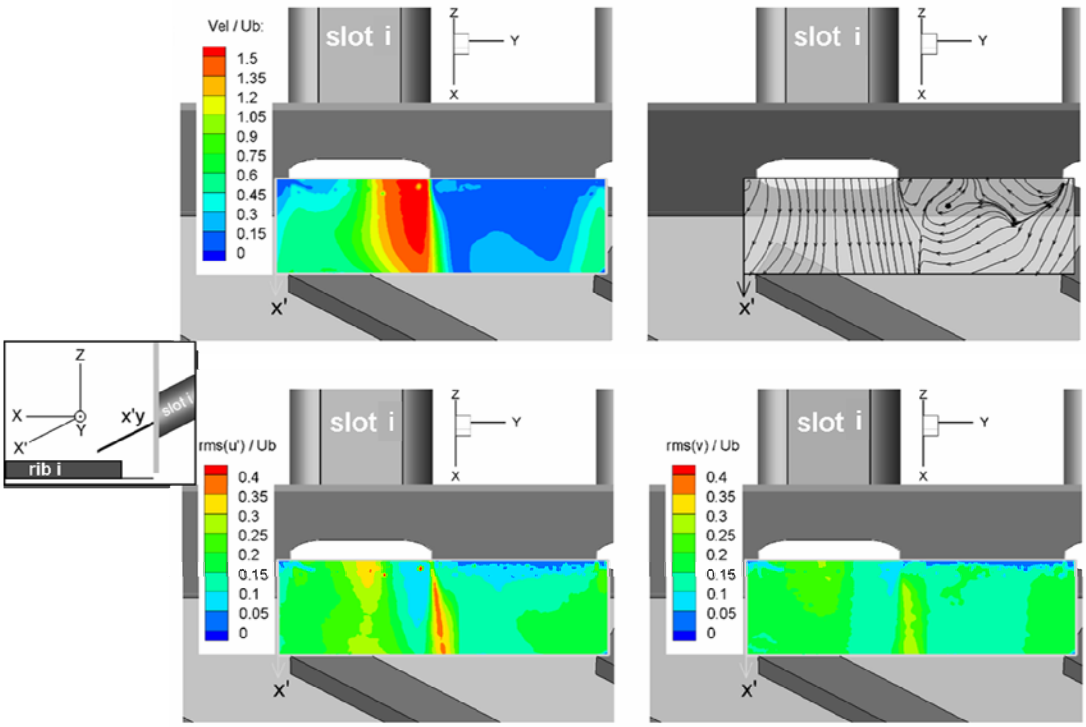


**Fig. 5.3** **Plane *x'y*: mean velocity (top left), streamlines (top right), *rms* of the velocity fluctuation along *x'* (bottom left) and along *y* (bottom right)**

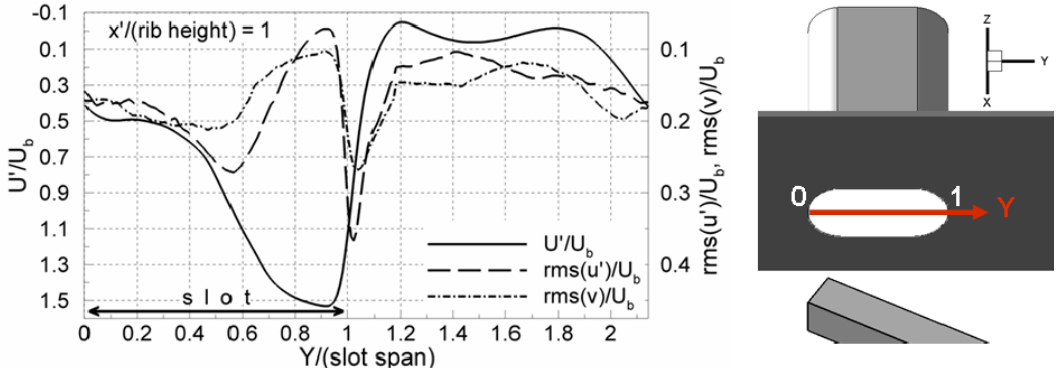


**Fig. 5.4** **Profiles of mean velocity and *rms* extracted on plane *x'y* at one rib height from the mid-wall**

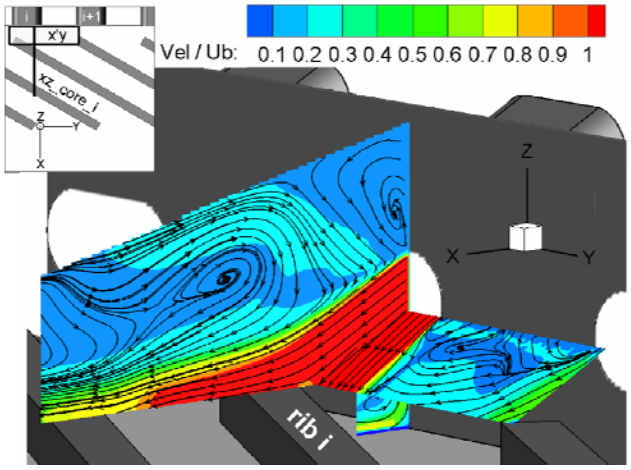


**Fig. 5.5** **3D view of planes *xz_core_i* and *x'y*, streamlines and mean velocity**

### 5.2.2 – Inter-rib area

In-plane mean velocities and streamlines on plane *xy1*, which is parallel to the floor of the ribbed wall with an offset of 0.2*e*, are depicted in Fig. 5.6. The projections of slot *i*, *i+1* and *i+2* are marked for reference. A strong impingement is highlighted by the streamlines pattern close to the upstream edge of rib *i*, corresponding to the location of the plane *xz_core_i* (marked in red in the figure). After impinging, part of the flow rebounds towards the mid-wall, part is guided along rib *i* and towards rib *i+1*. In correspondence of the projection of slots *i+1* and *i+2*, the deviation of the streamlines path suggests the existence of a second and third impingement, produced by the jets issued by slot *i+1* and *i+2* on rib *i*; these appear to deviate the flow towards rib *i+1*.

In order to identify the region of cross-plane velocity gradient, the continuity equation for incompressible flow is exploited:

$$\frac{\partial U}{\partial x}+\frac{\partial V}{\partial y}=-\frac{\partial W}{\partial z} \tag{5.8}$$

The left hand side can be calculated from the PIV results. It provides the magnitude of the wall-normal derivative, but not its direction. However, as the measurement plane is very close to the wall, both an increase of velocity approaching the wall and a decrease of velocity getting away from the wall can be discarded. Therefore, taking the positive *z*-axis as a reference, a negative value of $-\partial W/\partial z$ represents a downward "acceleration" (in the sense of velocity gradient), while a positive value represents an upward "deceleration". The result of this analysis is presented in Fig. 5.7: along rib *i*, three zones of downward deceleration of correspond to the three impingement areas of decreasing intensity previously identified from the observation of the mean flow path.

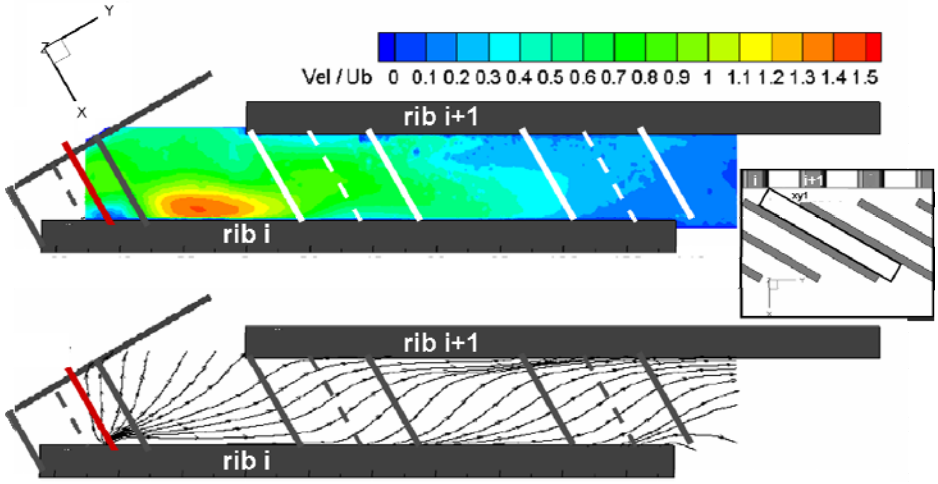


**Fig. 5.6** **Plane *xy1*: mean velocity contours (top) and streamlines (bottom). The projection of slot *i*, *i+1* and *i+2* (gray and white lines), as well as plane *xz_core_i* (red line) are marked for reference**

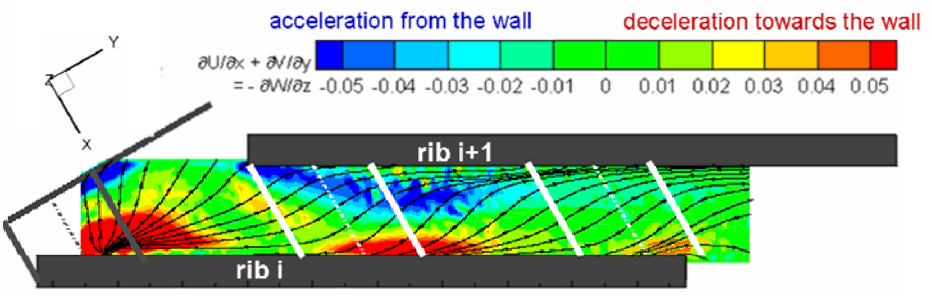


**Fig. 5.7** **Plane *xy1*: cross-plane velocity gradient close to the bottom wall**

In the center of the inter-rib domain a wide area of upward acceleration indicates that the flow directed against rib *i+1* is forced to lift off. Similarly, a region of intense upward acceleration adjacent to the mid-wall is related to the flow rebounded back after the first impingement, which hits the mid-wall and lifts off.

The flow just above the ribs is studied through the measurements performed along plane *xy2*, located 1.5 rib heights above the floor of the rib-roughened wall. Contour plots of mean in-plane velocity, streamline paths and *rms* over planes *xy2* and *x'y* are presented in Fig. 5.8. To better visualize the flow field, the geometrical periodicity is exploited and the velocity fields are duplicated in the *y*-direction. The rib guidance effect appears far less important above the turbulators: this volume is mainly dominated by the jets, with the streamlines almost aligned in the *x*-direction. High velocity fluctuations are observed in the jet core up to half of the rib length, and *rms(u)* presents values up to 60% higher than *rms(v)*.

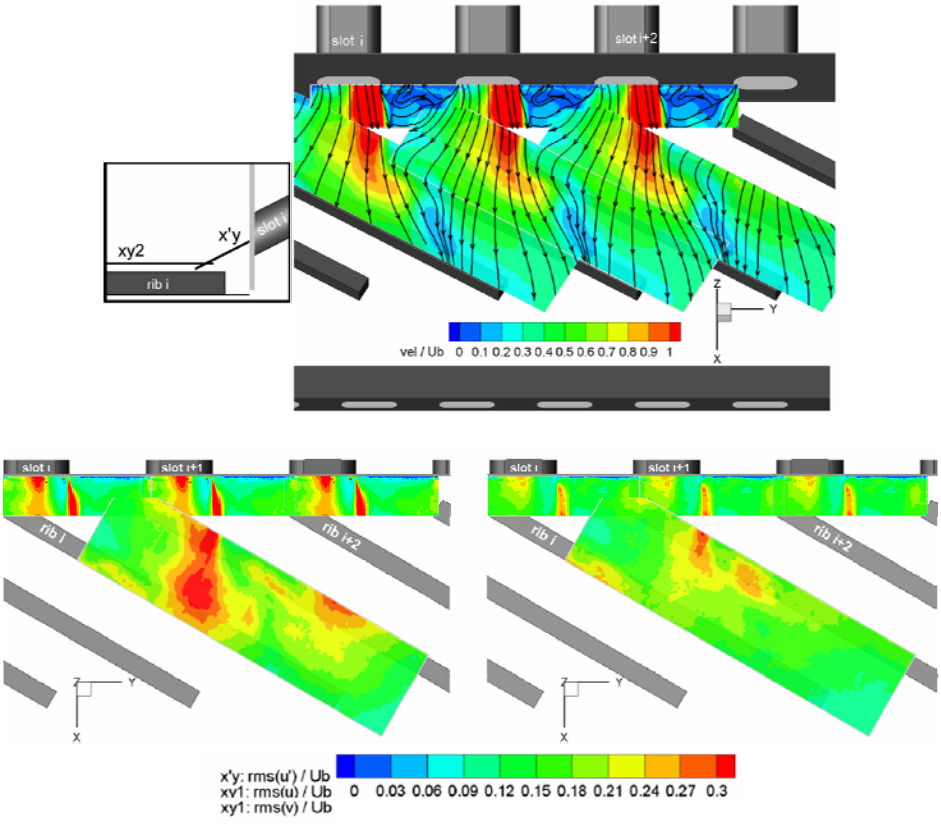


**Fig. 5.8** **Planes *x'y* and *xy2*: mean velocity and streamlines (top), *rms(u')* and *rms(u)* (bottom left), and *rms(v)* (bottom right)**

### 5.2.3 – Upward jet deflection

The results described so far suggest the existence of two upward flow motions originating from the complex jet-rib interaction. A characterization of such structures is obtained by means of PIV measurements conducted in the vertical plane in between two mid-wall slots. Fig 5.9 depicts contour levels of mean in-plane velocity and streamlines along plane *xz_mid_i_i+1*, and partly along *xy1*. The streamlines show that, after the first impingement on rib *i*, part of the jet bounces back towards the mid-wall and rolls up. A significant fraction of the flow constitutes an upward structure that reaches the smooth wall opposite to the rib-roughened wall. As previously deduced by observing the streamlines in *x'y* (Fig. 5.3), a large component of the velocity in between two slots is directed in the *z*-direction. At further distance from the mid-wall, the streamlines pattern indicates the presence of a second upward structure: as deduced from the results in plane *xy1* (Fig. 5.7), the flow lifts off from the inter-rib domain: the structure is sufficiently strong to reach the upper wall and to sustain a recirculation area which is bounded by the ribs, the smooth wall and the upward

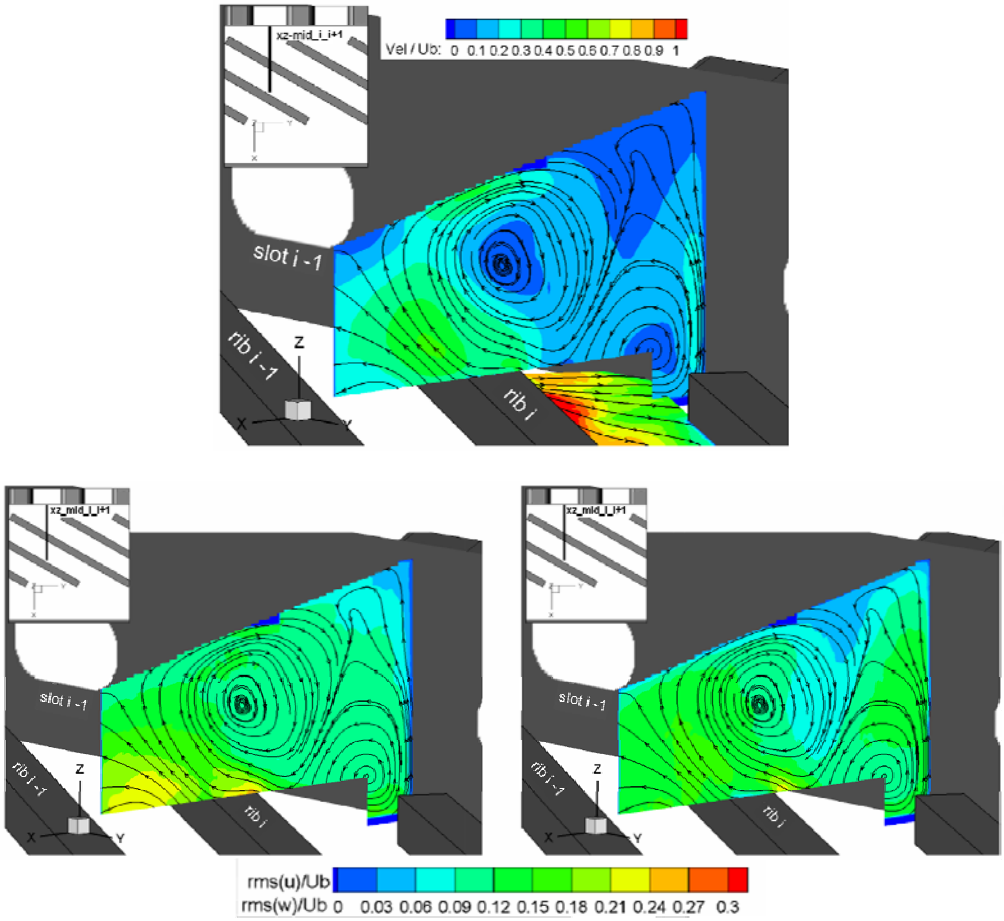


**Fig. 5.9** **Planes *xz_mid_i_i+1*: mean velocity and streamlines (top), *rms(u)* (bottom left) and *rms(w)* (bottom right)**

structure close to the mid-wall. The strength of this upward flow motion is also confirmed by relevant values of in-plane velocity fluctuations (Fig. 5.9, bottom).

### 5.2.4 – Interaction with the smooth wall

The impact of the upward flow motions previously described can be appreciated by the study of the flow close to the smooth wall. Figure 5.10 reports PIV results in *x"y*, a plane parallel to the smooth wall at a distance of 0.3*e*. Periodical impingement regions at the middle of the surface are clearly identified by source points in the streamlines pattern, as well as by the velocity gradient in wall-normal direction, highlighted in a similar manner as in Fig. 5.7. From those areas, the flow spreads in all directions and then leaves the surface along two different separation lines: one describes an arc just above the jet core and divides the successive areas of

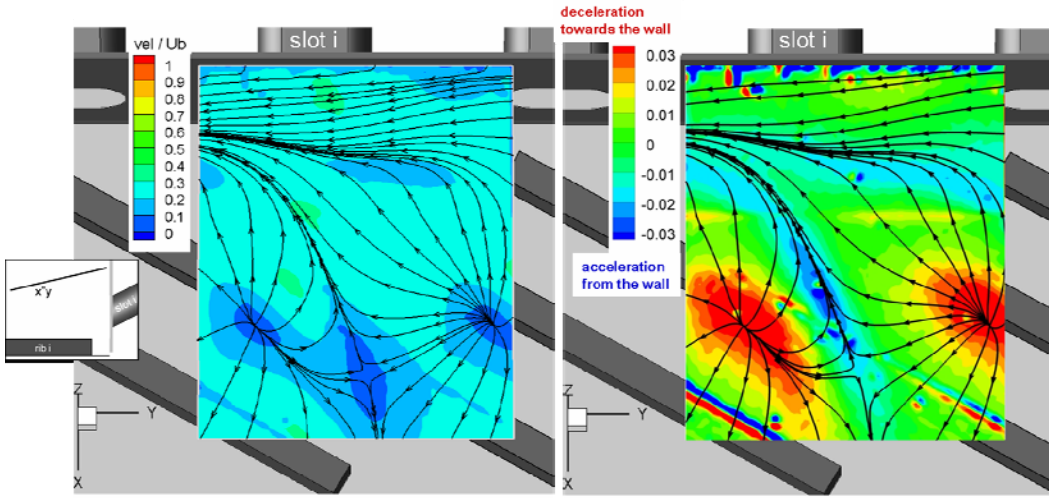


**Fig. 5.10** **Plane *x"y*: mean velocity and streamlines (left) and cross-plane acceleration (right)**

impingement (periodic in the *y*-direction); the other separation line is parallel to the mid-wall, and bounds the flow that comes from the upward structure close to the mid-wall. This recirculating flow, bounded by the mid-wall and the second separation line, appears directed in the negative *y*-direction; this is a secondary effect of the ribs guidance: the turbulators direct the flow towards one of the side-wall of the channel (i.e. the tip of the blade, referring to Fig. 3.1); since there is no net mass flow in the *y*-direction through the trailing cavity, to satisfy mass conservation part of the flow must have a negative component in the *y*-direction (i.e. towards the hub of the blade); unsurprisingly, this happens in a region of low momentum, i.e. above the row of crossing jets.

### 5.2.5 – Mean flow model

Figure 5.11 provides an overview of the PIV measurements. From this ensemble, a model for the mean flow in the rib-roughened trailing edge channel is deduced and depicted in Fig. 5.12.

Only part of the momentum in the *y*-direction present in the inlet channel is dissipated through the mid-wall slots, which results in a remarkable unbalance of momentum within the slot section: the jet core extends over less than half of the slot span. The crossing-jets effectively penetrate inside the cavity up to the far end of the turbulators; each jet impacts on the three ribs that are in front of each slot. Therefore three impingement areas can be defined along rib *i*: *Imp I*, *Imp II* and *Imp III*, produced by the jets issued by slot *i*, *i+1* and *i+2*, respectively.

The edge of rib *i* where *Imp I* is produced splits the jet in two: part is blocked by rib *i* and is directed against the floor, where it rebounds towards the mid-wall and towards rib *i+1*; part overtakes rib *i*, impinges on rib *i-1* and eventually (very weakly)

on rib *i-2*. The streamlines directed towards the mid-wall either rolls up under the jet itself, or lifts off to generate an upward structure *VS1* that reaches the smooth wall. The flow rebounded towards rib *i+1* is guided by the turbulators and passes under the jet produced by slot *i+1*, and eventually reaches rib *i+1*: the flow then separates from the floor and produces a second upward motion *VS2*, stronger than *VS1*, that impinges on the smooth wall. The second impingement *Imp II* contributes to deviate the inter-rib flow towards rib *i+1*. The effect of the third impingement *Imp III* is far less

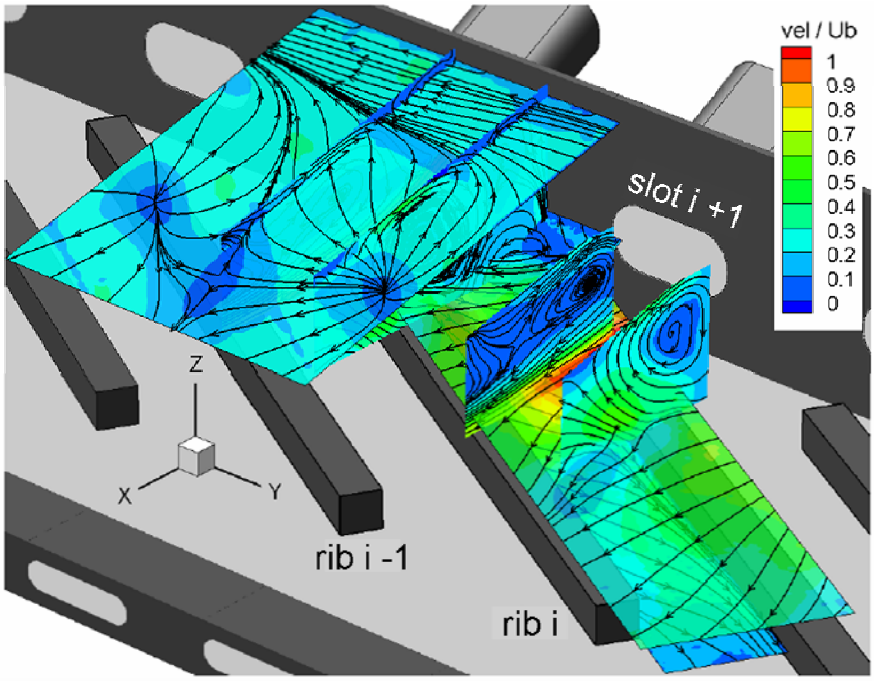


**Fig. 5.11** **Three-dimensional overview of the PIV measurements**

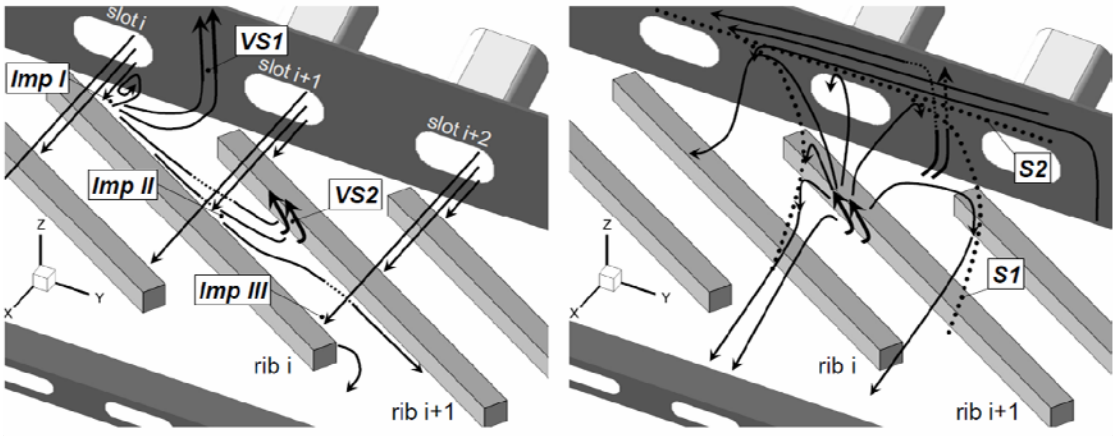


**Fig. 5.12** **Mean flow model in the rib-roughened trailing channel deduced from PIV measurements**

evident: it mainly produces a deviation of the flow towards the exit slots.

The vertical structure *VS1* impinges on the upper wall in between two mid-wall slots. Above the jets, close to the corner between the smooth wall and the mid-wall, the flow is organized in a recirculation structure mainly directed towards the blade hub (negative *y*-direction). The upward structure *VS2* produces an impingement on the smooth wall, approximately at half way between mid-wall and exit wall. From this point the flow spreads in all directions: part goes towards the trailing edge, while the remainder separates from the upper wall along two different separation lines: the first one (*S1*) divides the flow coming from similar upward structures *VS2*; the second one (*S2*) is parallel to the mid-wall, and divides the flow coming from *VS1* and *VS2*.

The present model attempts to describe the aerodynamical features of the channel in the area investigated by PIV, i.e. between the mid-wall and the far end of the turbulators. In this fraction of the cavity the flow appears dominated by jets and ribs, which share the same spacing in *y*-direction: therefore, periodicity from one ribbed domain to another is assumed. The periodical nature of the flow is also confirmed by planes *xz_core_i+1* and *xz_mid_i+1_i+2* (visible in Fig. 5.11), which display minor differences with respect to *xz_core_i* and *xz_mid_i_i+1*, respectively. No PIV measurements are taken in the part of the channel closer to the exit: the quality of the measurements in a horizontal plane would be severely affected by the vicinity of the walls on both sides. Here the flow, as suggested by surface-streamlines flow visualizations (see next section), is dominated by the influence of the exit slots, which have a dissimilar spacing than the mid-wall slots and the ribs (about 5*e* for the exit slots, 7.5*e* for the mid-wall slots); consequently the aerodynamic features in the vicinity of the exit wall follow a different periodicity. Without detailed velocity measurements, a line of demarcation between these two different spatial periodicities is difficult to identify. As it will be seen from the convective heat transfer results, it seems that the effect of the exit slots spacing is felt already before the far end of the ribs.

## *5.3 – Flow models from flow visualizations*

Qualitative flow models for the configurations not investigated by PIV (i.e. the non-ribbed geometry and the three ribbed geometries with shifted/tapered obstacles), are obtained via surface streamline flow visualizations.

In the configuration without ribs the crossing-jets impinge on the floor and spread laterally (Fig. 5.13); they interact with each other and create an upward motion that impacts on the opposite wall. Close to the exit wall, impingements are produced in between each pair of exit slots. The latter feature is also evident in the ribbed configurations, included the standard one, as confirmed by the heat transfer results (see Chapter 6 and 7).

In the configuration where the ribs are shifted by half a pitch in the *y*-direction (geometry *G2*), the jets first impinge on the bottom wall, and then reach the turbulator (Fig. 5.14). Only rib *i* is directly affected by the impingement. After the jet breakdown,

some streamlines are directed towards the mid-wall; unlike in *G1* though, the presence of rib *i+1* keeps them from reaching the wall, and no vertical structure is produced close to the mid-wall. A large part of the flow is deflected upwards by the rib (vertical structure *VS*) and impacts on the upper wall. The jet-rib interaction produces an unsteady, highly turbulent structure (*TS*) on the top side of the rib: low frequency bursting is observed from the oil streaks accumulated in that area. Among others, Chyu and Natarajan (1991) reported a similar mechanism for the flow around a wall-mounted cube studied with similar visualization techniques, and they argued that such unsteady phenomenon was crucial for the elevated local heat/mass transfer.

Configurations *G3* and *G4* are obtained by tapering the ribs of the standard configuration *G1* and in configuration *G2*, respectively. Flow visualizations performed

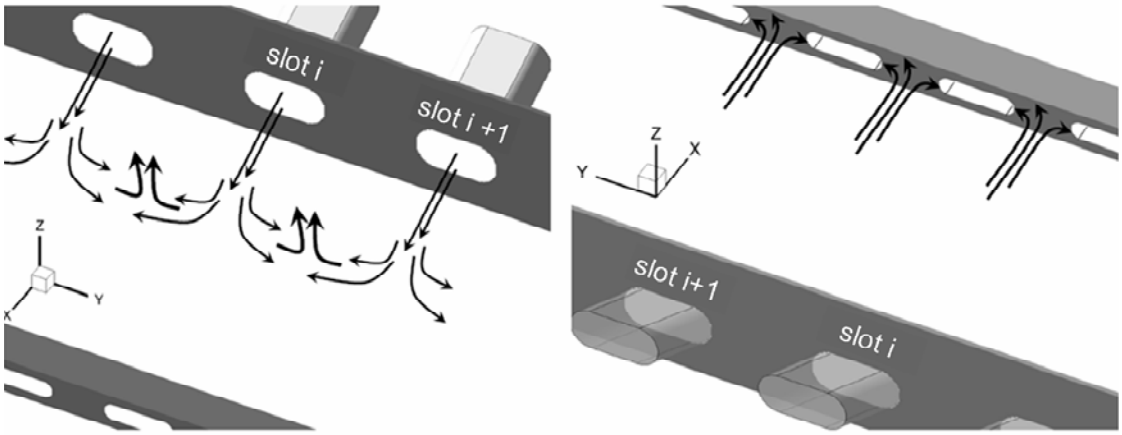


**Fig. 5.13** **Mean flow model for the non-ribbed configuration deduced from flow visualizations. Outlet view angle (left) and inlet view angle (right)**

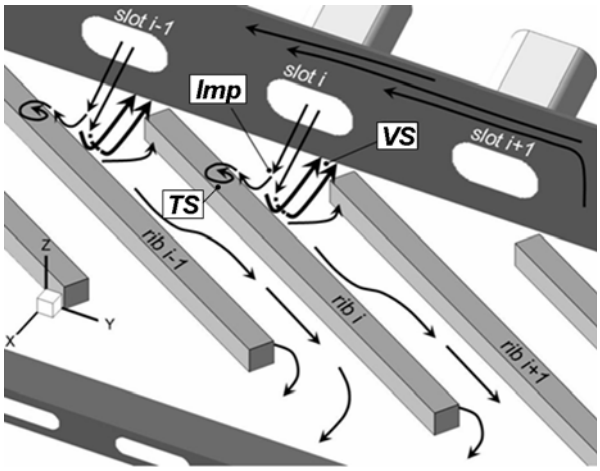


**Fig. 5.14** **Mean flow model for configuration *G2* deduced from flow visualizations**

on those geometries demonstrate that tapering the ribs does not alter dramatically the flow path. Nevertheless a significant difference is to be stressed in the region close to the exit wall, where the tapered ribs present the minimum height: the streamlines are not guided anymore by the obstacles, but leap over them and remain mainly aligned with the *x*-direction (Figs. 5.15). This flow feature is particularly significant in configuration *G3*, because all the three impingements striking each rib are able to overcome the obstacle.

The proposed flow models are consistent with the thermal pattern displayed by liquid crystals thermography presented in Chapter 6.

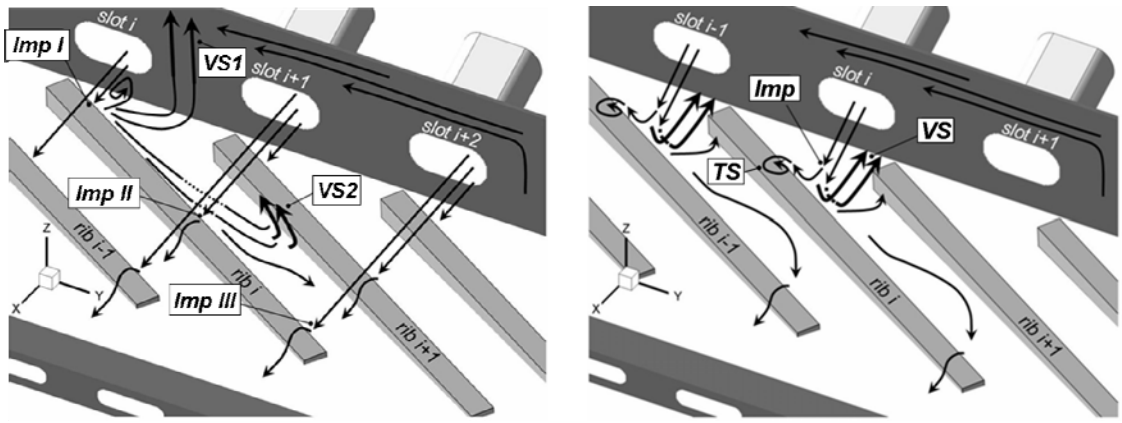


**Fig. 5.15** **Mean flow model for configuration *G3* and *G4* deduced from flow visualizations**

# Chapter 6 – Convective heat transfer investigation

The heat transfer distributions obtained in a purely convective regime (uniform heat flux at the solid-fluid interface) are presented in this section. The geometry without ribs is investigated and taken as baseline for evaluating the effect of the rib insertion; such configuration will be referred to as geometry *G0*. The standard rib-roughened geometry (*G1*) is analyzed in deeper detail, stressing the link between the thermal patterns and the flow features revealed by the PIV velocity measurements discussed in the previous chapter. The effect of tapering the obstacles and/or shifting them in the *y*-direction with respect to the mid-wall slots is assessed studying three additional configurations (*G2*, *G3* and *G4*). The high spatial resolution of the reported heat transfer coefficient distributions allows for a precise evaluation of the local cooling performance. On the other hand, area-averaging the thermal fields eases the comparison of the global performance among the different geometrical arrangements.

As for the aerodynamic measurements, the Reynolds number is equal to the engine-representative value of 67500 for all experiments. No significant variation in the heat transfer patterns are expected as the Reynolds number varies within the range of practical interest. Taslim et al (1998), who investigated a similar geometry, reported area-averaged Nusselt number values in the range $Re$ = 30000 – 50000: the trend fits remarkably well the curve $Nu/Re^{0.8}$ (see their Fig. 2), as expected for convective heat transfer in turbulent internal flows.

## *6.1 – Configuration without ribs*

Contour plots of the Nusselt number (Eq. 4.4) for configuration *G0* are shown in Fig. 6.1. The target surfaces, for this as for the geometries presented successively, are downstream of slot $i$ and slot $i+1$, in the central area of the test section ($i$ = 7).

The thermal pattern on the wall towards which the slots are inclined clearly reveals the location of the impingements: the scrubbing action of the jets has a strong and extensive effect on the heat transfer. The footprint of these impingements is highly non-symmetric with respect to the slot axis, indicating an unbalancing of the jets in the *y*-direction, as demonstrated in the previous chapter for the rib-roughened configuration. Further away from the mid-wall the thermal pattern realigns with the *x*-direction. The heat transfer progressively decreases approaching the exit wall, except for periodical semi-circular patterns of higher Nusselt number in between each pair of exit slots (made visible with the different scale used in the close-up in Fig. 6.1, top). These are due to the flow impinging on the exit wall, in accordance with the flow model presented in Chapter 5: when the coolant reaches the trailing edge of the cavity,

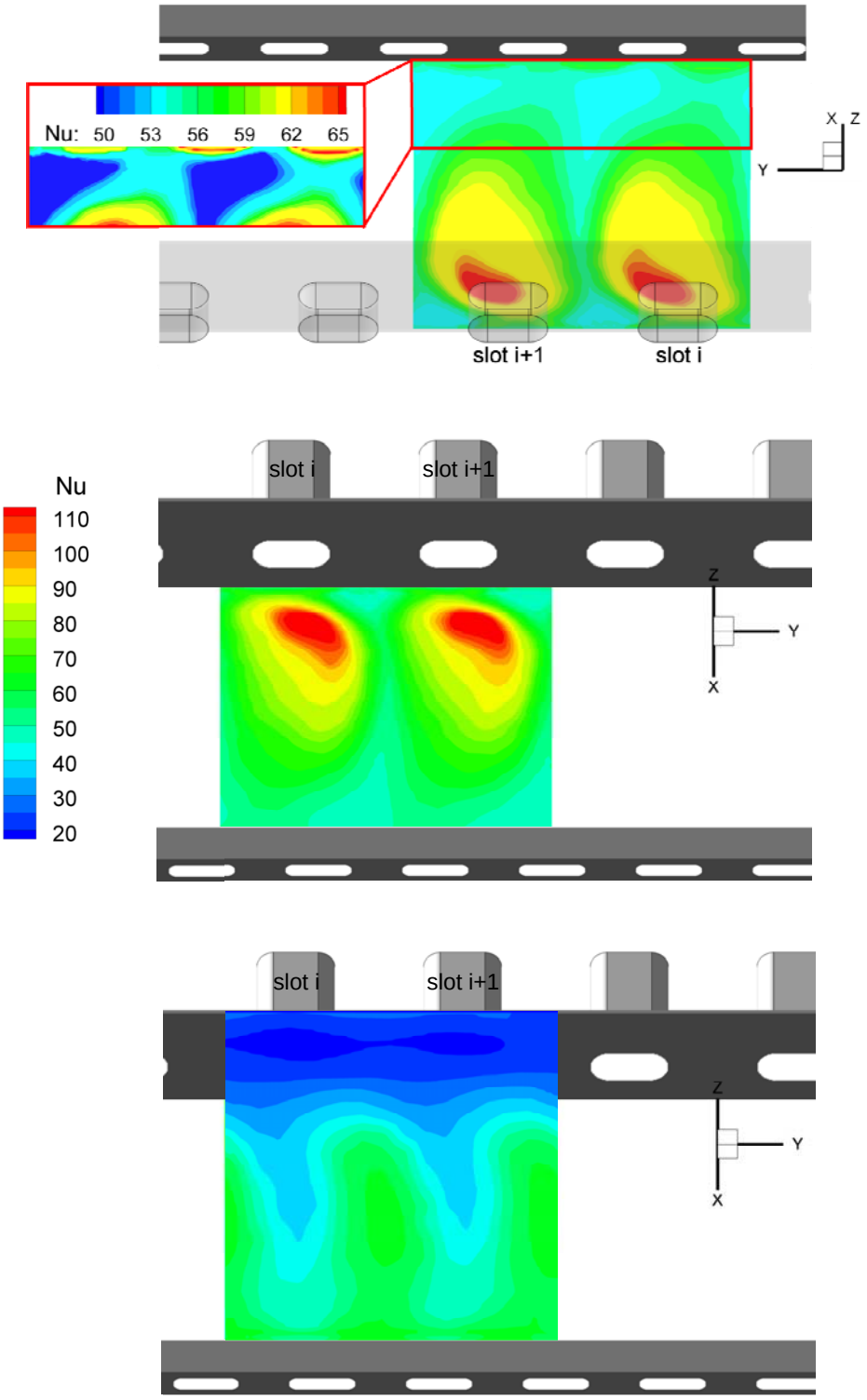


**Fig. 6.1** **Nusselt number distribution for configuration *G0*. Top: impingement wall viewed from the inlet. Center: impingement wall viewed from the outlet. Bottom: non-impingement wall viewed from the outlet**

it impacts on the exit wall and effectively enhances the heat transfer in the adjacent portion of the floor. The area-averaged Nusselt number on the smooth floor is $Nu$ = 67.9.

On the inclined wall (opposite to the one where the jets are directed) low Nusselt number levels in the vicinity of the mid-wall suggest the presence of a large low velocity area in the region above the jets. Periodical, bean-shaped high heat transfer regions show that the crossing jets, after the direct impingement, rebound and hit also this surface (as indicated by the model deduced form surface flow visualization). Comparing the Nusselt number values, the area-averaged value is $Nu$ = 41.9, i.e. 38% lower than on the opposite wall. Indeed, the jets loose large part of their momentum and cooling capability in impinging on the wall of direct impact. The location of the upper wall impingements with respect to the slots confirms the important $y$-component of the crossing jets, detected by PIV in the rib-roughened geometry: clearly such feature is proper of the crossing jets, independently from the presence of the ribs.

## *6.2 – Standard rib-roughened configuration*

Contour plots of the enhancement factor (*EF*) on the rib-roughened wall and on the opposite smooth wall are shown in Fig. 6.2 for the ribbed configuration *G1*. The *EF* is defined as the ratio between the local Nusselt number for the ribbed geometry and the area-averaged Nusselt number evaluated on the same wall for the non-ribbed geometry. Experimental data on the inter-rib floor are available only between rib *i-1* and rib *i* (i.e. between the $6^{th}$ and the $7^{th}$ obstacles). To better visualize the global thermal pattern, the contour plots on the floor are duplicated periodically along the contiguous domain (i.e. between rib *i* and rib *i+1*). Despite the geometrical periodicity of slots and ribs, the matching between the duplicated floor and the adjacent rib side is not smooth approaching the far end of the obstacle (see top frame of Fig. 6.2). This is due to the influence of the exit slots' spacing, which gains importance moving towards the trailing edge: as discussed in section 5.2.5, their different spatial periodicity plays a role in the second part of the cavity, and becomes dominant in the vicinity of the exit wall.

The main feature of the Nusselt number distribution in configuration *G1* is the high heat transfer associated to the jet issued from slot *i* and directly impinging on the edge of the correspondent rib. Two other relatively high heat transfer regions are detected along the same turbulator, as put in evidence by the two *EF* profiles extracted along rib *i* (Fig. 6.3): one profile is extracted on the floor between rib *i* and rib *i+1*, at 0.3*e* from the former (red line in figure); the other is extracted on the top side of the obstacle itself, at 0.3*e* from the edge facing the jets (blue line in figure). Downstream of the peak corresponding to the first impingement, the *EF* trend shows two other local maxima (which on the floor look more like two plateaux), one around mid-length and the other near the far end of the obstacle: they are due to the second and third impingement respectively (corresponding to the jets issued from slots *i+1* and *i+2*).

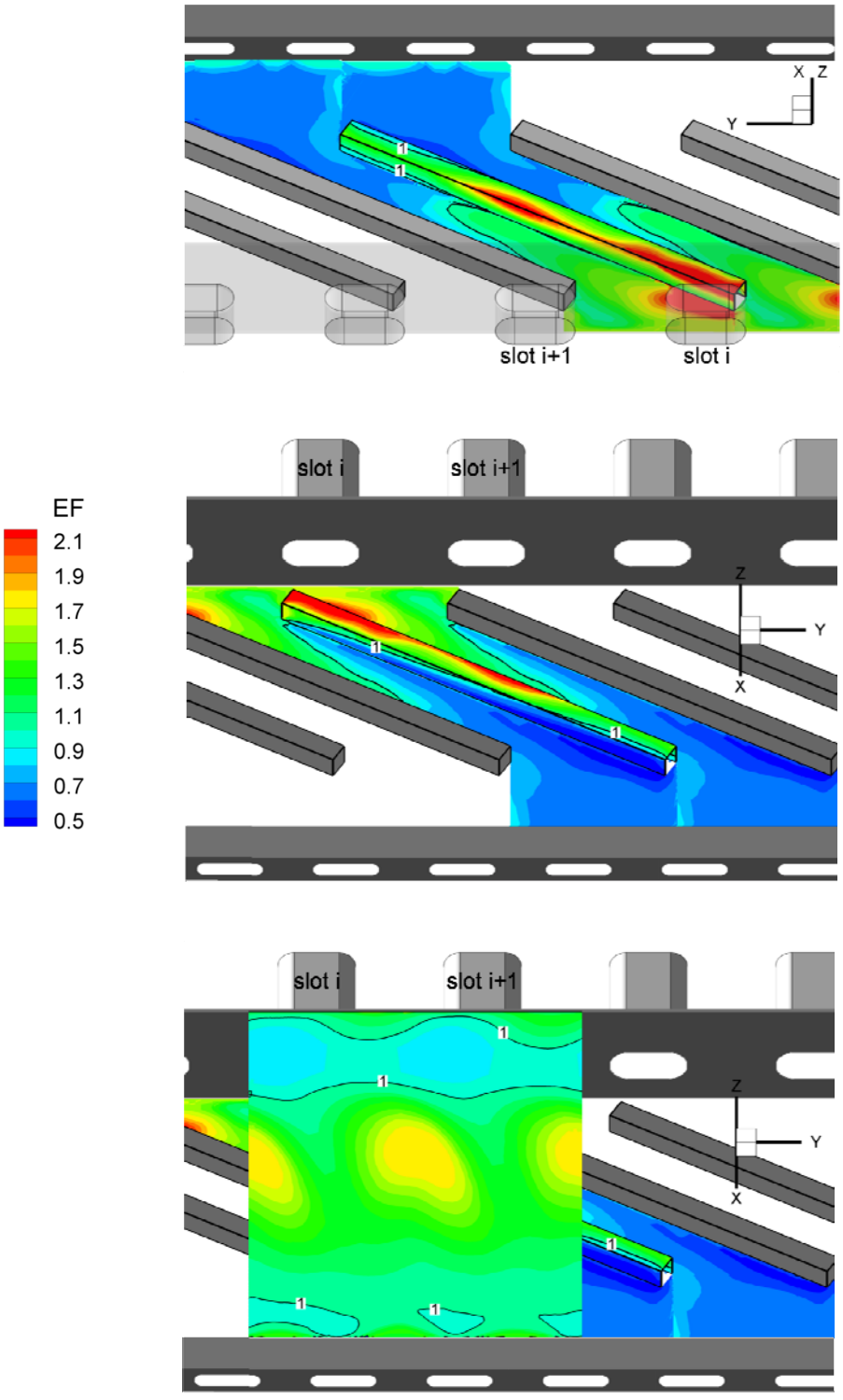


**Fig. 6.2** **Enhancement factor distribution for configuration *G1*. Top: impingement wall viewed from the inlet. Center: impingement wall viewed from the outlet. Bottom: non-impingement wall viewed from the outlet**

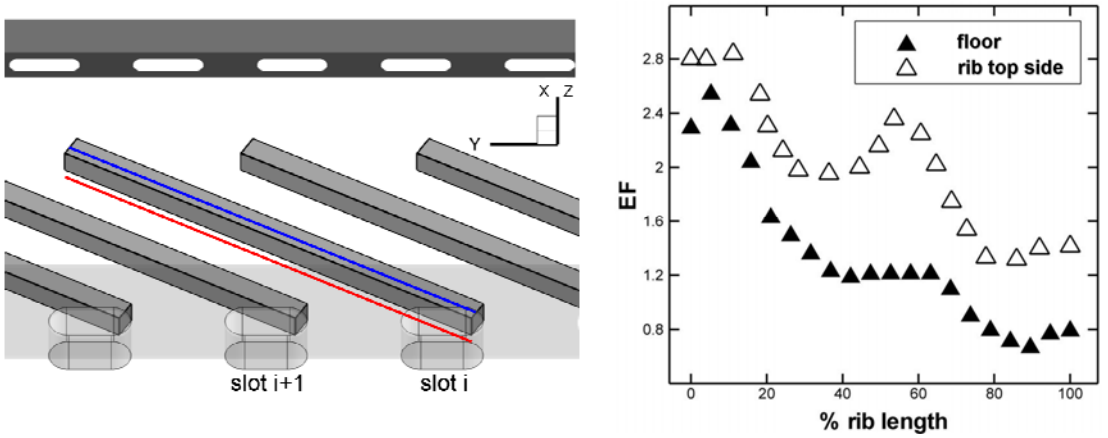


**Fig. 6.3** **Profiles of *EF* along the rib highlighting the effect of the three impingements in configuration *G1*. Left: location of the profiles. Right: extracted values**

Compared to the first impingement, the second and third one appear by far less effective, since the corresponding jets have lost most of their momentum in the previous impingements. The heat transfer levels are remarkably higher on the turbulator than on the floor; this is consistent with the flow model, in which the crossing jets impinge directly on the top edge of the turbulators. Close to the downstream edge of the obstacle, the rib side facing the exit slots and the adjacent floor appear poorly cooled: here the presence of the rib itself prevents the flow from effectively cooling this portion of the surface. Near the trailing edge periodical patterns of higher Nusselt number are present between each pair of exit slots. As seen for the non-ribbed configuration, this feature is interpreted as a consequence of the impingements on the exit wall between each pair of exit slots.

In order to stress the impact of the flow features on the heat transfer, in Fig. 6.4 the *EF* contours (solid lines) are superimposed to the streamlines and to the map of wall-normal velocity gradient (colour contours) for the inter-rib floor. The velocity fields are evaluated at 0.2*e* from the surface (plane *xy1*) as described in Chapter 5. Along rib *i* three zones of vertical deceleration towards the floor indicate three impingement areas of decreasing extension and strength, coinciding with the heat transfer peaks. In the centre of the inter-rib domain an area of out-of-plane acceleration away from the floor reveal an upward deflection of the flow (structure *VS2*, see Fig. 5.12). Consistently, the *EF* diminishes across this area of vertical motion, indicating a less effective cooling of the wall surface as the flow approaches rib *i+1*.

Along the smooth wall opposite to the rib-roughened one, the footprints of the *y*-periodic impingements are visible (Fig. 6.2, bottom). However, comparing the thermal patterns with those obtained in the configuration without ribs (Fig. 6.1, bottom), the periodical peaks of heat transfer coefficient present a different shape and position. The semi-circular patterns of high heat transfer are evident in the vicinity of the exit wall. To support the comparison, a local-to- local *EF* map is plotted in Fig. 6.5: the contours

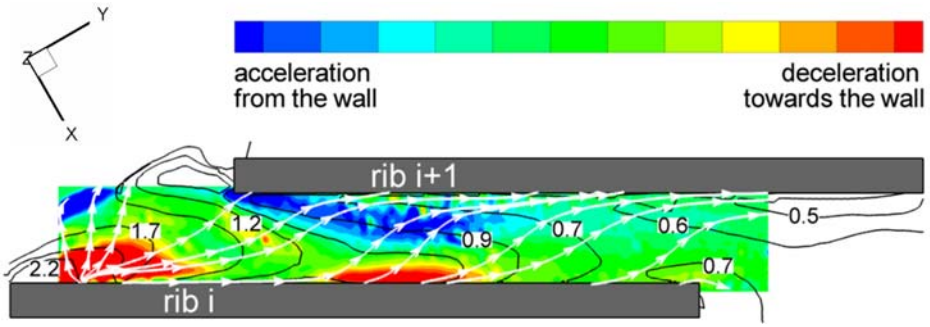


**Fig. 6.4** **Streamlines (white), wall-normal acceleration (colour contours) and *EF* distribution (labeled black contour lines) on the inter-rib floor for geometry *G1***

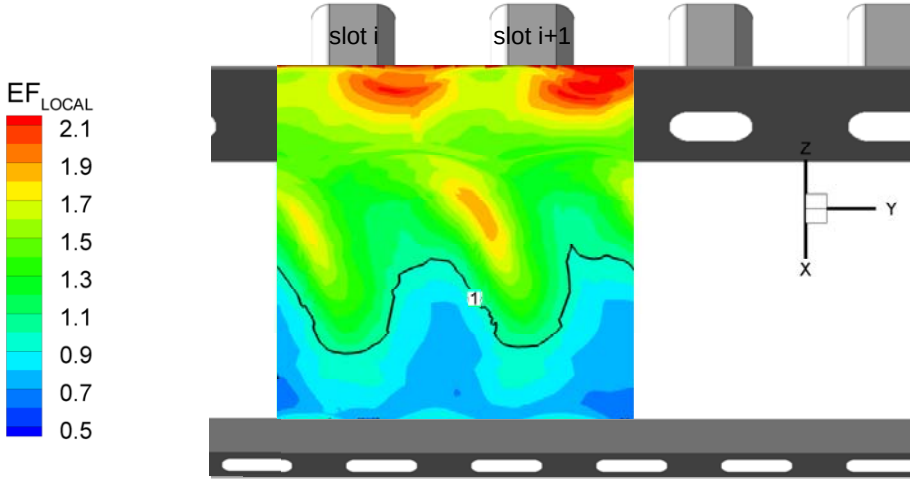


**Fig. 6.5** **Local-to-local enhancement factor distribution on the smooth wall for configuration *G1***

are obtained dividing the local Nusselt number by the corresponding value for the smooth geometry. The presence of the turbulators influences the intensity and direction of the upward flow motion *VS2*. According to the flow model deduced from PIV measurements, when the crossing jets impinge on the non-ribbed floor, they directly rebound towards the upper wall; on the other hand, in presence of the turbulators a more complex flow pattern is observed: the blockage of the turbulators forces the lift off of the streamlines, which gain a higher vertical component with respect to the non-ribbed configuration. This results in a more localized, but more effective scrubbing on the opposite wall. The vertical structure *VS1* also contributes to improve the heat transfer, impinging in an area as critical as the corner between the smooth wall and the mid-wall. Moreover, the guidance of the ribs moves the impingement regions closer to the mid-wall, reducing the extent of the low velocity area above the crossing-jets, which is also beneficial for the wall cooling. As a matter

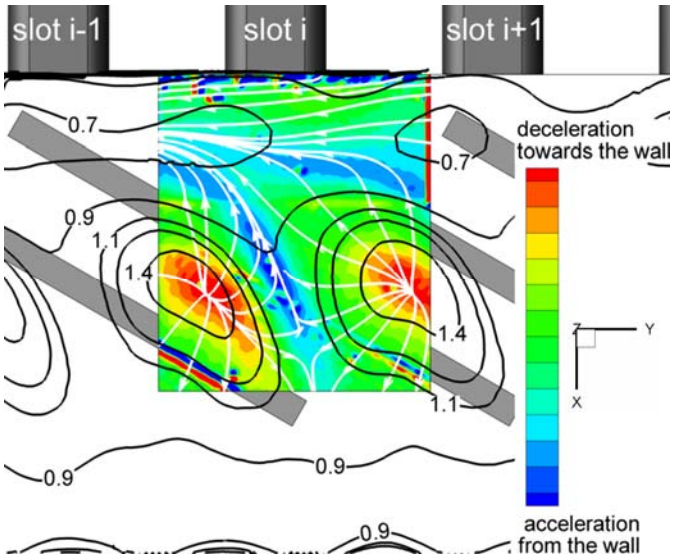


**Fig. 6.6** **Streamlines (white), wall-normal acceleration (colour contours) and *EF* distribution (black labeled lines) on the smooth wall for geometry *G1***

of fact, the area-averaged Nusselt number over this surface increases by 16% with respect to the non-ribbed geometry. All these features (shifting and intensification of the rebounded impingement, additional impingements close to the mid-wall and general improvement of the cooling action) are clearly visible in Fig. 6.5.

As done above for the inter-rib floor, the aero-thermal coupling on the opposite smooth wall is highlighted by superimposing the *EF* contours (solid lines) to the streamlines and to the map of wall-normal acceleration (color contours); the velocity field is evaluated at 0.3*e* from the surface (plane *x"y*), as described in Chapter 5. In the areas of maximum heat transfer, i.e. where the structure *VS2* impinges on the wall, the flow experiences a deceleration (in the sense of negative velocity gradient) approaching the wall. Similar conditions are visible around the impingement of the vertical structure *VS1* (far less intense than *VS2*). Conversely, the zones where the flow accelerates away from the wall correspond to the separation lines *S1* and *S2* (see again Chapter 5, section 5.2.5).

## *6.3 – Modified rib-roughened configurations*

### 6.3.1 – Configuration with shifted ribs

The geometry *G2* is derived from the standard ribbed configuration *G1*, applying to the ribs a shift in the *y*-direction equal to half of their pitch (Fig. 6.7). Such geometrical variation is studied in order to explore the effect of altering the jet rib-interaction, which proves to be a crucial flow feature in geometry *G1*.

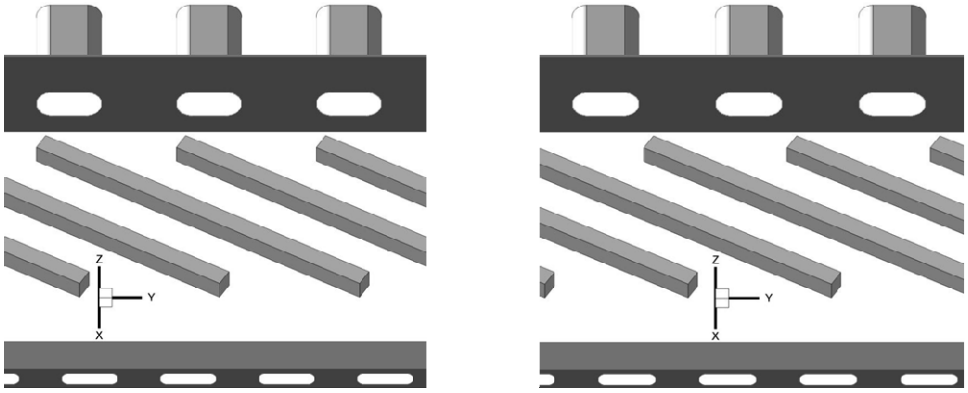


**Fig. 6.7** **Standard ribbed geometry *G1* (left), compared with geometry *G2* (right) with ribs shifted by half pitch in *y*-direction**

Figure 6.8 displays contour plots of the enhancement factor on the ribbed wall and on the opposite smooth wall for geometry *G2*. As deduced from flow visualization (section 5.3), only one impingement is produced on the rib-roughened wall. According to the inferred flow model, the jet issued by slot *i* impacts first on the floor, and then on rib *i*. The high level of heat transfer on the lateral and top side of the turbulator are attributed to the unsteady, highly turbulent flow structure (*TS* in Fig. 5.14) created by the jet-rib interaction. The impingement on the opposite smooth wall, due to the rebound of the jet against the ribbed wall, is more intense than in *G1*, with Nusselt number peaks almost 40% higher. This is due to the different nature of the vertical structure *VS* with respect to the structure *VS2* found in *G1*: *VS2* is the result of a double deflection of the flow by the ribs, and the coolant reaches the upper wall after loosing most of its momentum; in *G2* the jet, after impinging on the bottom wall, is directly forced to lift and produces a more effective scrubbing action when hitting the smooth wall. On the other hand in geometry *G2* no vertical structure impinges close to the mid-wall.

The above considerations are reinforced looking at the local Nusselt number ratio presented in Fig. 6.9 for the inter-rib floor and for the opposite smooth wall: this is obtained dividing the local Nusselt number in configuration *G2* by the correspondent level in *G1* (of course for the inter-rib floor a half-pitch-shift is applied to superimpose the two areas). On the floor, *G1* performs better along the side of rib *i* which faces the jets, because of the three impingements produced on the obstacle. On the opposite smooth wall the different location of the impingements is evidenced by the alternating patterns, favourable to one or the other geometry; moreover *G1* performs better close to the mid-wall, where it benefits from the vertical structure *VS1* (absent in *G2*). Looking at the semicircular patterns associated to the impingements in between the exit slots, it appears that, with respect to configuration *G1*, those impingements affects more the smooth wall and less the ribbed wall. A possible explanation is the following: the stronger upward flow motion in *G2* results in a higher momentum of the streamlines reaching the trailing edge in the vicinity of the smooth wall, while a

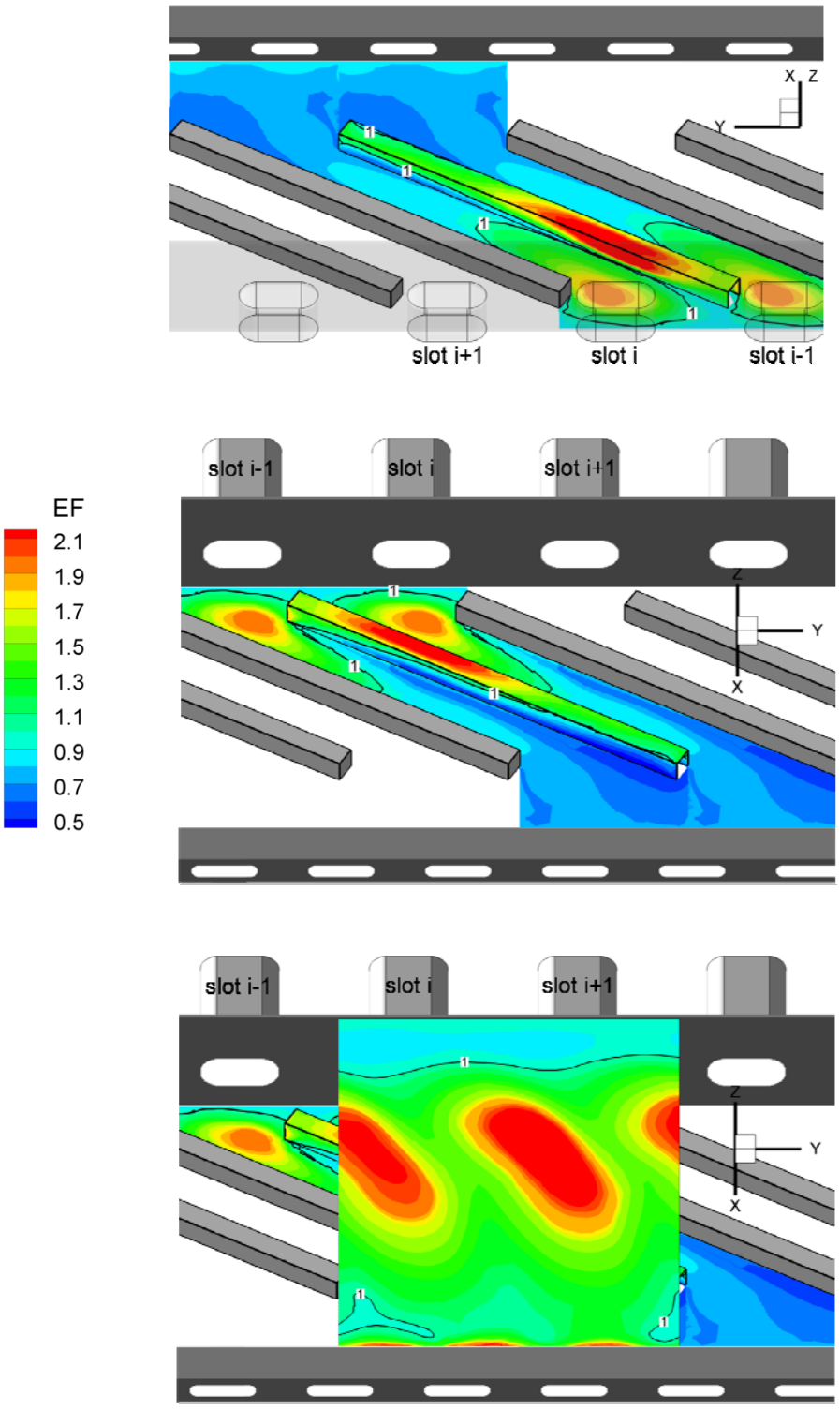


**Fig. 6.8** **Enhancement factor distribution for configuration *G2*. Top: impingement wall viewed from the inlet. Center: impingement wall viewed from the outlet. Bottom: non-impingement wall viewed from the outlet**

relative deficit is experienced at the opposite ribbed wall. However there is no conclusive proof of such reasoning, due to the lack of quantitative aerodynamic information in this area.

### 6.3.2 – Configurations with tapered ribs

Configurations *G3* and *G4* are obtained from *G1* and *G2* respectively, by tapering the obstacles with an angle of about 2.3° (Fig. 6.10). This results in a reduction of the rib height by a factor five at the far end of the turbulator. These two geometries are considered in order to investigate the possible benefit of reducing the rib blockage where the channel has the minimum flow section, i.e. close to the trailing edge slots.

Figure 6.11 shows contour plots of *EF* on the rib-roughened wall and on the

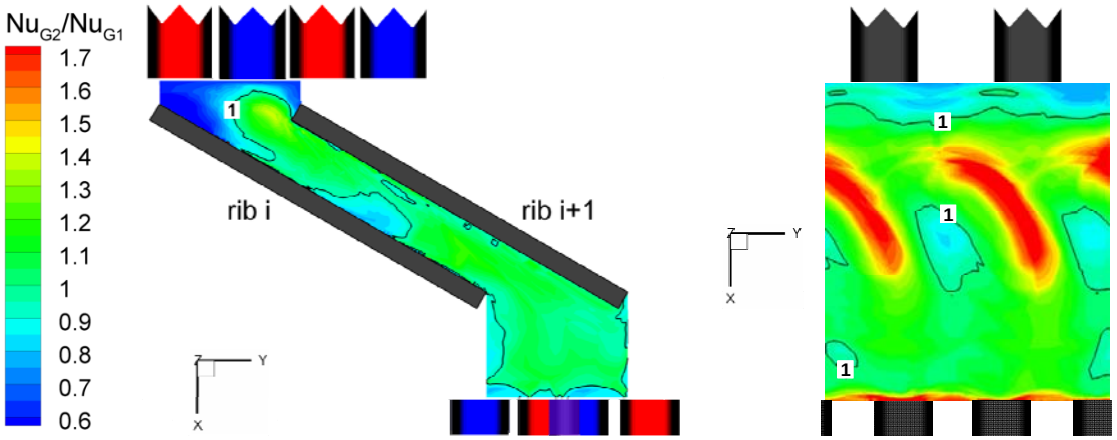


**Fig. 6.9** **Local Nusselt number ration *G2*/*G1* on the inter-rib floor (left) and on the opposite smooth wall (right). On the left, the slots in *G1* are red and the ones in *G2* are blue**

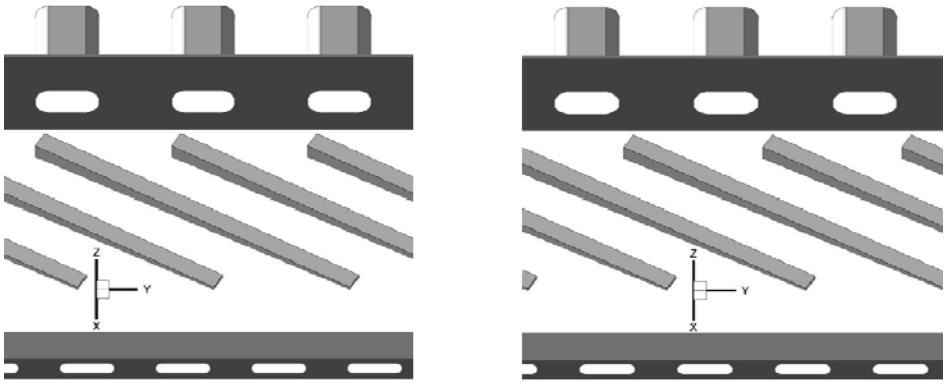


**Fig. 6.10** **Geometry *G3* (left) and *G4* (right), obtained from *G1* and *G2* respectively. by tapering the ribs**

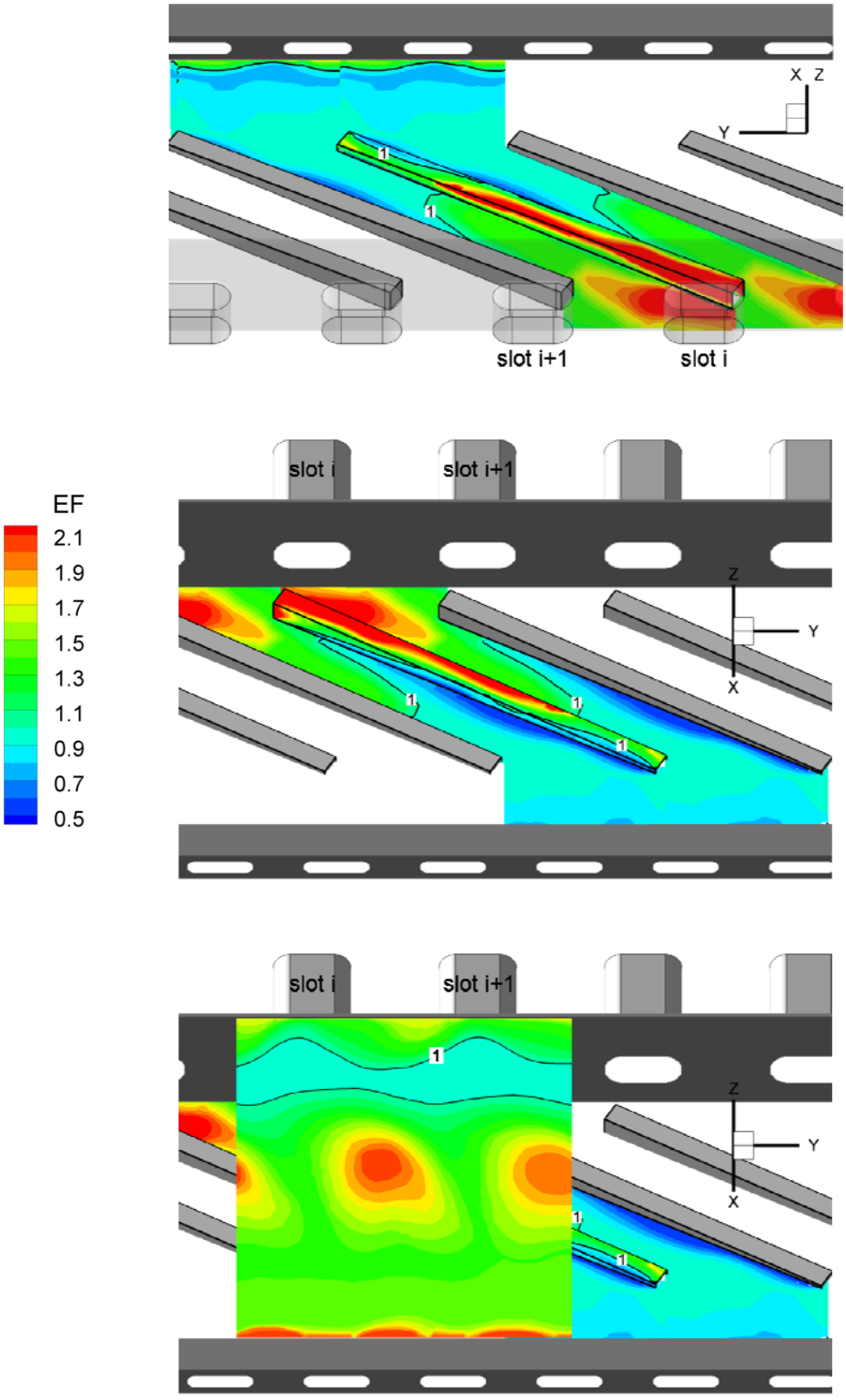


**Fig. 6.11** **Enhancement factor distribution for configuration *G3*. Top: impingement wall viewed from the inlet. Center: impingement wall viewed from the outlet. Bottom: non-impingement wall viewed from the outlet**

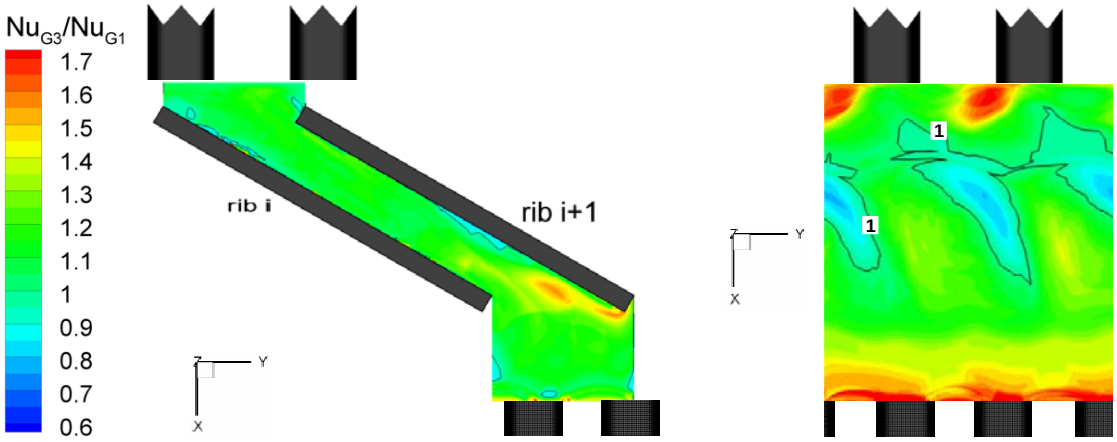


**Fig. 6.12** **Local Nusselt number ration *G3/G1* on the inter-rib floor (left) and on the opposite smooth wall (right).**

opposite smooth wall for geometry *G3*. In comparison with configuration *G1*, similar thermal patterns and comparable Nusselt number levels are found over a large portion of these surfaces. However a substantial improvement in terms of cooling performance is found on the rib-roughened wall near the far end of the rib, both on the floor and on the surface of the turbulator facing the exit slots. This is due to the fact that, as shown earlier, in geometry *G1* the presence of the obstacle itself prevents the flow from effectively cooling this part of the cavity; hence the benefit of tapering the obstacle: the reduced rib height allows a large part of the streamlines issued from slots *i+1* and *i+2* to stream over the turbulators and reach the floor, enhancing the heat extraction. This is clearly visible from Fig. 6.12, displaying the *G3/G1* Nusselt number ratio. It also appears that the exit wall impingements are more effective in the tapered configuration. This can be explained reasoning on the evolution of the flow temperature in the two geometries: in configuration *G1* most of the flow reaches the far end of the cavity area after three impingements, therefore extracting much heat and experiencing a consequent temperature raise; on the other hand, in configuration *G3* a large part of the flow that reaches the exit wall comes directly from the crossing-jets, passing over the tapered ribs; therefore the coolant has lower temperature and higher cooling capability when it arrives at the trailing edge. However, without proper investigation of the flow temperature across the cavity, this remains our best interpretation. Another possible explanation is that, as the tapered obstacles provide a weaker guidance in *y*-direction, the flow is more jet-dominated and maintains a higher *x*-component when impacting on the exit wall.

Considering the smooth wall, the Nusselt number ratio *G3*/*G1* indicates that in the tapered configuration the vertical structure *VS1* is significantly stronger and its influence more extensive. A possible explanation is that the flow recirculation above the jets directed in negative *y*-direction, which in *G1* interferes with *VS1* (see for example Fig. 5.9), is less intense in *G3* due to the reduced guidance of the tapered ribs in positive *y*-direction. Approaching the exit wall, the enhanced Nusselt number levels

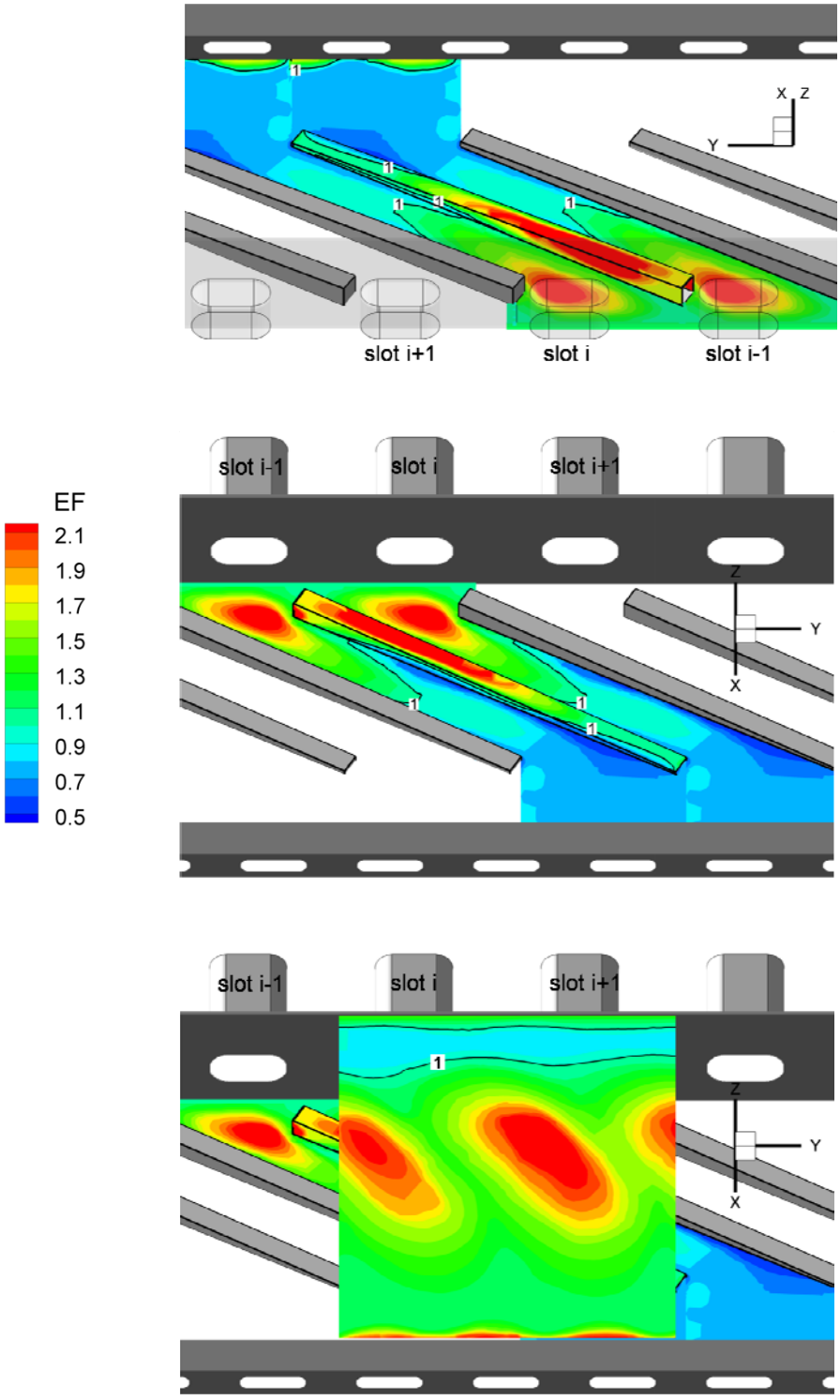


**Fig. 6.13** **Enhancement factor distribution for configuration *G4*. Top: impingement wall viewed from the inlet. Center: impingement wall viewed from the outlet. Bottom: non-impingement wall viewed from the outlet**

suggest that the streamlines leaping over the ribs reach the upper wall and participate to the heat extraction.

Figure 6.13 displays contour plots of the enhancement factor on the rib-roughened wall and on the opposite smooth wall for geometry *G4*, which is obtained from configuration *G2* by tapering the ribs in the same way it is done for *G3*. As expected, thermal patterns and heat transfer levels are comparable to those relative to *G2*. As in configuration *G3*, tapering the ribs proves to be a useful remedy for reducing the hot spot near the far edge of the obstacles. However the improvement with respect to the non-tapered configuration is less important than in *G3*. Indeed, the flow in the configurations with shifted turbulators (*G2* and *G4*) is less affected by the presence of the ribs, as just one impingement is produced on each of them (and only after the impact on the floor). Therefore the improvement in the second half of the cavity due to the tapering is less significant. The gain in the areas of impingement in between the exit slots can be explained by arguments similar to those proposed earlier when describing the thermal performance of *G3*.

## *6.4 – Area-averaged heat transfer performance*

Table 6.1 summarizes the heat transfer results in terms of area-averaged enhancement factor computed over the investigated walls for the four considered ribbed configurations. A breakdown of the target surfaces helps to discriminate the contribution of each portion of the channel.

Interestingly, in the standard ribbed configuration *G1* the rib insertion is not beneficial for the inter-rib floor: *EF* is smaller than 1. As put in evidence by the local heat transfer measurements, the presence of the obstacles is actually detrimental for the heat transfer over large part of this surface. The obstacles are instead indirectly responsible for improving the cooling of the opposite smooth wall, as they strengthen the upward flow motion that produces impingements on this surface. Besides, the turbulators increase the area of heat transfer, and they exhibit themselves high values of Nusselt number.

| **Enhancement Factor** | ***G1*** | ***G2*** | ***G3*** | ***G4*** |
|---|---|---|---|---|
| All surfaces | 1.14 | 1.20 | 1.36 | 1.28 |
| Smooth wall | 1.19 | 1.40 | 1.40 | 1.43 |
| Rib-roughened wall | 1.05 | 1.04 | 1.29 | 1.16 |
| Inter-rib floor | 0.92 | 0.91 | 1.15 | 1.03 |
| Rib surface | 1.29 | 1.28 | 1.64 | 1.52 |
| Top side | 1.61 | 1.62 | 1.78 | 1.66 |
| Inlet side | 1.50 | 1.37 | 2.04 | 1.68 |
| Exit side | 0.75 | 0.86 | 1.01 | 1.08 |

**Tab. 6.1** **Area-averaged enhancement factor over the target surfaces for the four studied ribbed configurations**

As for the modified ribbed geometries, the gain obtained on the smooth wall by shifting and/or tapering the ribs is striking. It appears that there is room for optimizing the relative rib-slot alignment: exploiting the capacity of the rebounded jet of cooling down the opposite smooth wall, significant enhancement of the heat transfer is achieved. It is clear that also tapering the turbulators is beneficial for the heat transfer: as a matter of fact, without reducing the rib height in this area, the blockage ratio associated to the obstacles (rib height/local channel height) attains values in excess of 30%, which is known to be detrimental for the thermal performance also in conventional cooling geometries. Globally, *G3* is the configuration with the highest overall enhancement factor.

# Chapter 7 – Conjugate heat transfer investigation

The present chapter is devoted to the presentation and discussion of the heat transfer results obtained in conjugate (conductive-convective) regime. The analysis is focused on the rib-roughened wall of the standard geometry (referred to as configuration *G1* in Chapter 6). The thermal performance is assessed in terms of non-dimensional wall temperature and Nusselt number. Additionally, the ribs are characterized by means of performance parameters borrowed from extended surface heat transfer: fin effectiveness and fin efficiency. Three materials of different thermal properties are used for the heat transfer wall: stainless steel, Inconel and ceramoplastic. For material grades and their values of thermal conductivities, see Tab. 3.1 in Chapter 3.

As stated in Chapter 2, in order to obtain results which are truly representative of the engine reality, is necessary that, beside *Re* and *Pr*, also *K* (solid-to-fluid thermal conductivity ratio) is kept constant between engine conditions and laboratory environment. The Reynolds number adopted in the experiments is representative of a modern cooling scheme. The Prandtl number is essentially a property of the cooling fluid, which in the experiments is air as in most aeronautical applications. As for the conductivity ratio, a realistic value for a cooled blade is compared in Tab. 7.1 with those obtained in the present experiments. The actual engine value is estimated assuming Nimonic 105 at 1250 K as blade material and air at 1050 K as coolant. Using Inconel 625 near ambient temperature, the value of *K* matches satisfactorily engine conditions. Stainless steel and ceramoplastic are used as terms of comparison to assess the effect of the conductivity ratio on the thermal boundary conditions, and in turn on the heat transfer rate.

The presented results are obtained on rib *i* and the neighboring floor, i.e. the two halves of the adjacent inter-rib domains (between the obstacles *i-1*/*i* and *i*/*i+1*). The index *i* corresponds to the $7^{th}$ rib.

## *7.1 – Local heat transfer performance*

### 7.1.1 – Non-dimensional temperature distribution

Contour plots of the non-dimensional temperature Θ (see Eq. 4.15) along the rib-roughened wall are displayed in Fig. 7.1 and 7.2 for the three investigated materials, from two opposite angles of view.

The pattern is dominated by a well cooled area resulting from the first impingement on rib *i*. Comparing the temperature trend for the different materials, the effect of the

| Environment | Solid | Fluid | Conductivity ratio *K* [-] |
|---|---|---|---|
| Engine | Nimonic 105 @1250 K | Air @1050K | 375 |
| Laboratory | Stainless steel @320K | Air @300K | 600 |
| Laboratory | Inconel @320K | Air @300K | 388 |
| Laboratory | Ceramoplastic @320K | Air @300K | 44 |

**Tab. 7.1** **Thermal conductivity ratio of the materials used for the ribbed wall**

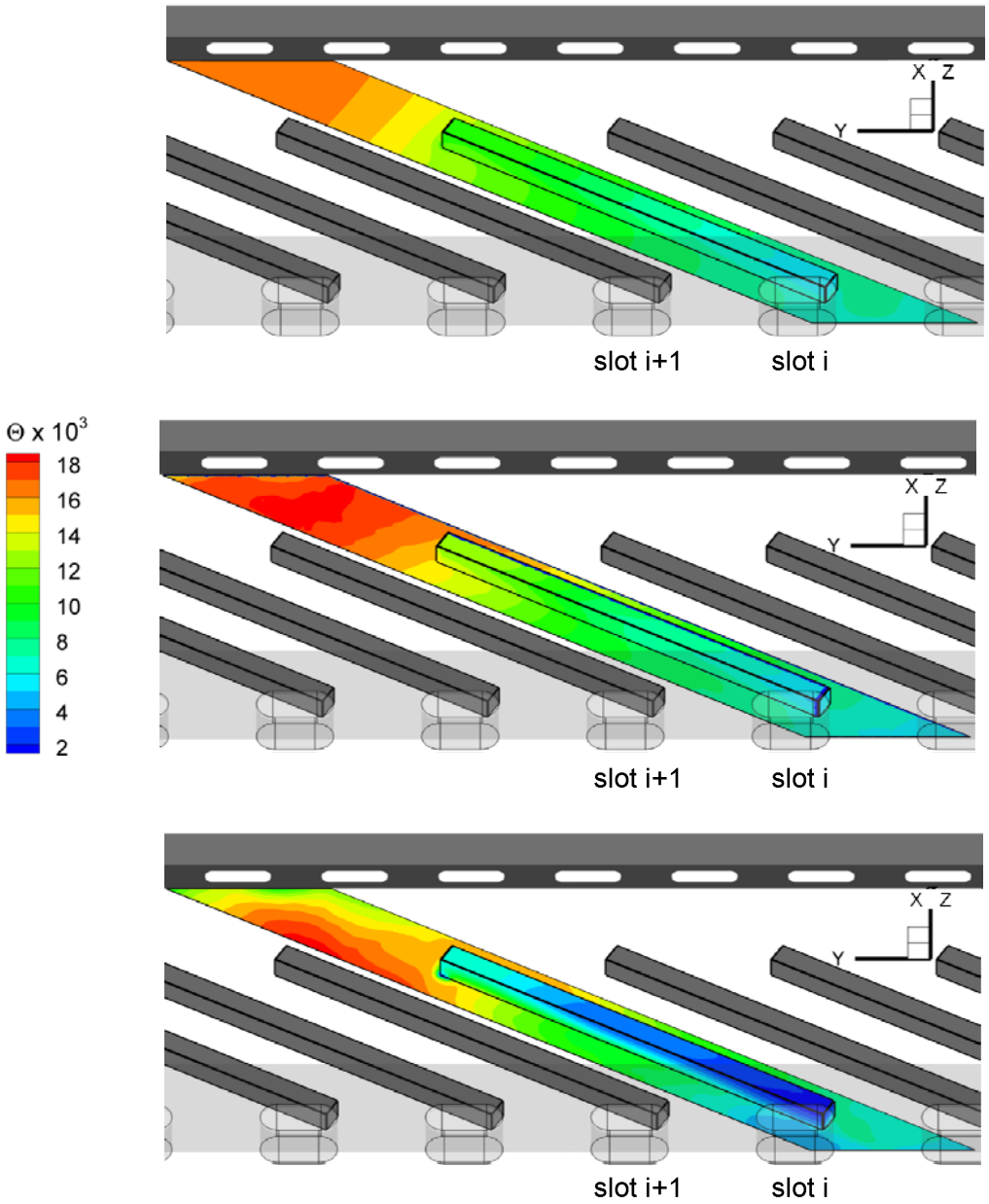


**Fig. 7.1** **Non-dimensional temperature distribution in conjugate regime, inlet view angle: stainless steel (top), Inconel (middle), ceramoplastic (bottom)**

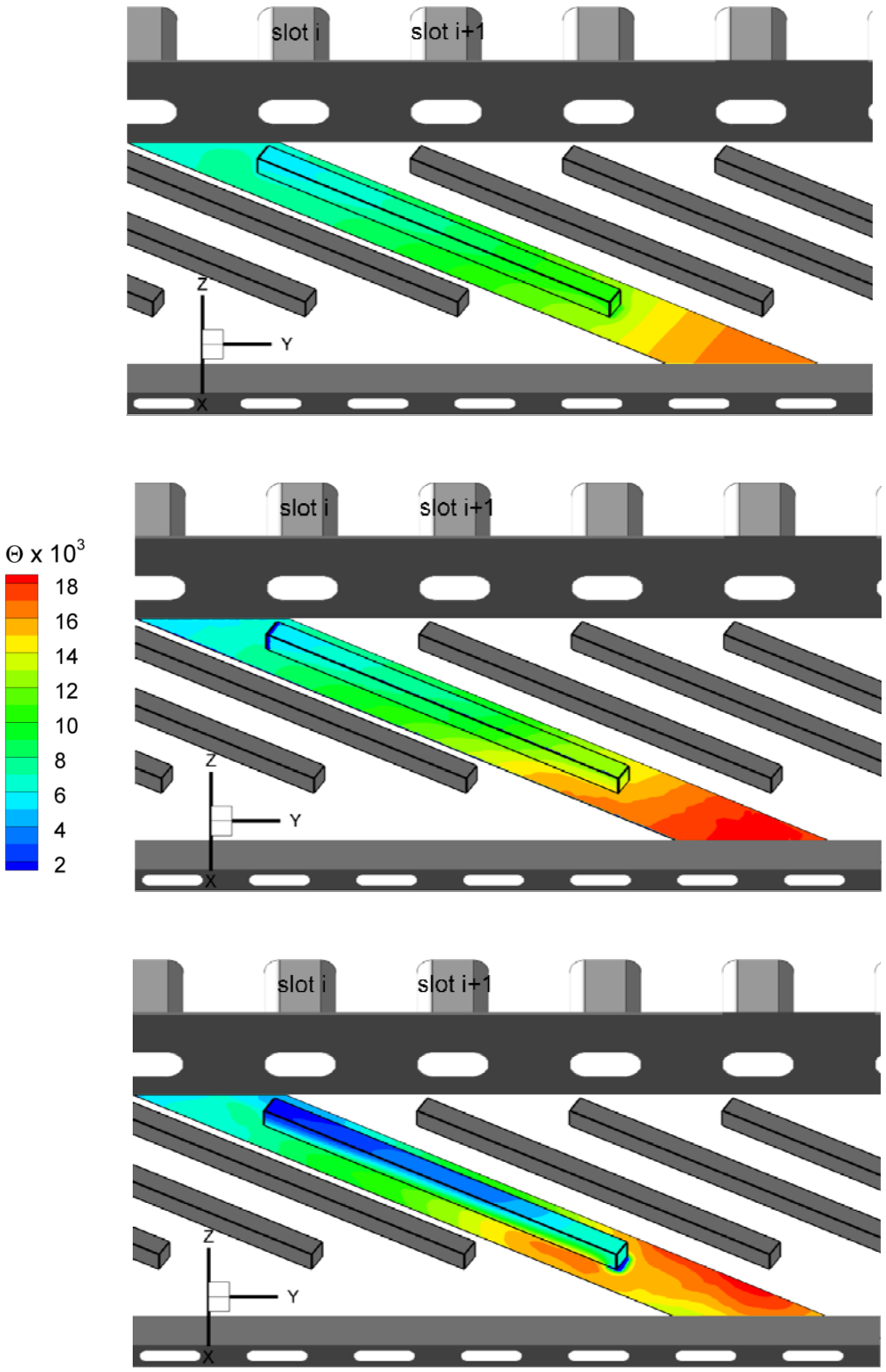


**Fig. 7.2** **Non-dimensional temperature distribution in conjugate regime, outlet view angle: stainless steel (top), Inconel (middle), ceramoplastic (bottom)**

conductivity clearly appears: the ceramoplastic exhibits strong local temperature gradients due to the high thermal resistance, while for the stainless steel the temperature variation is much milder and practically aligned with the rib. The temperature gradient along the streamlined surface for the different materials is most clearly shown in Fig. 7.3: a profile of non-dimensional temperature is extracted along the top side of rib *i*, at a distance of 0.3*e* from the impingement side (the abscissa increases with *y*-axis). For the stainless steel the peaks due to the impinging jets are smeared out. Conversely the ceramoplastic shows the footprint of the three impingements. Moreover the temperature level for the ceramoplastic is globally lower, because of the strong temperature drop across the rib thickness. The steep wall temperature gradients displayed by the ceramoplastic model highlight areas of inefficient cooling, as the region downstream the rib end close to the exit wall: here the presence of the rib itself prevents the flow from effectively cooling this portion of the channel, as already mentioned in Chapter 6.

In Fig. 7.1 and 7.2 one might notice that, in the second half of the channel with respect to the *x*-direction, the thermal pattern along the ribbed wall does not show periodicity in the *y*-direction. This is due to the fact that, as discussed in section 5.2.5 and section 6.2, approaching the exit wall the flow is largely affected by the position of the exit slots, which have a different spacing with respect to the mid-wall slots.

As for the non-dimensional wall temperature, a direct comparison with the purely convective heat transfer mode, presented in Chapter 6, is not feasible: the convective results are obtained imposing a uniform heat flux at the solid-fluid interface; therefore the definition of $\Theta$ for those data would not be consistent with the present one (in which the reference heat flux is the one imposed at the back-side of the wall, Eq. 4.15). However an insightful comparison can be drawn on a different basis. Let us perform a numerical experiment: the heat transfer coefficient distribution obtained in a purely convective regime is applied as Robin boundary condition to the ribbed surface of the FEM model described in section 4.4.3; the conductivity of the material is set equal to the one of Inconel 625, so the conductivity ratio is engine-representative;

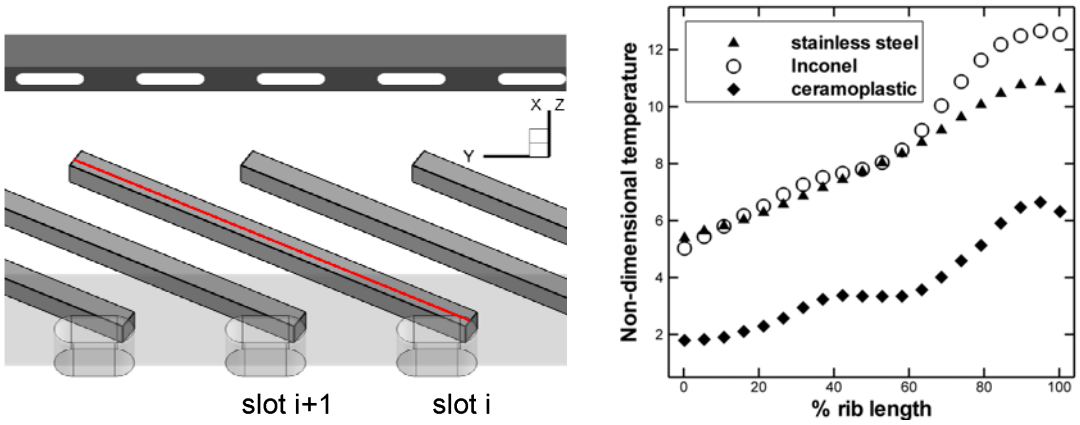


**Fig. 7.3** **Profile of non-dimensional wall temperature extracted along the top of the rib. Left: location of the profile. Right: extracted values**

a uniform heat flux equal to the level imposed in the experiments is applied at the backside, and the conduction equation is solved. The resulting temperature field is then used to evaluate the non-dimensional temperature. This pseudo-conjugate scenario corresponds to what is often applied in industrial design, when the heat transfer coefficient is considered invariant to thermal boundary conditions and correlations/simulations developed in purely convective environment are applied (although conjugate computations are not uncommon in today's industry design practice). One obtains for this case a non-dimensional temperature distribution Θ' based on Eq. 4.15. The difference between the resulting Θ' levels and the measured Θ levels reflects the misestimation of the thermal levels if the through-wall conduction is neglected. Direct comparison is presented in Fig. 7.4 in terms of $\Delta\Theta = \Theta' - \Theta$. Differences as high as 0.0025 (far beyond the uncertainty) are found. If rescaled to engine levels, assuming realistic heat flux of 700 to 1000 $kWm^{-2}$ at the external side of the airfoil, such deviations correspond to 26 to 33 K of misestimation. The largest wall temperature underestimation occurs in correspondence of the hot spot close to the far

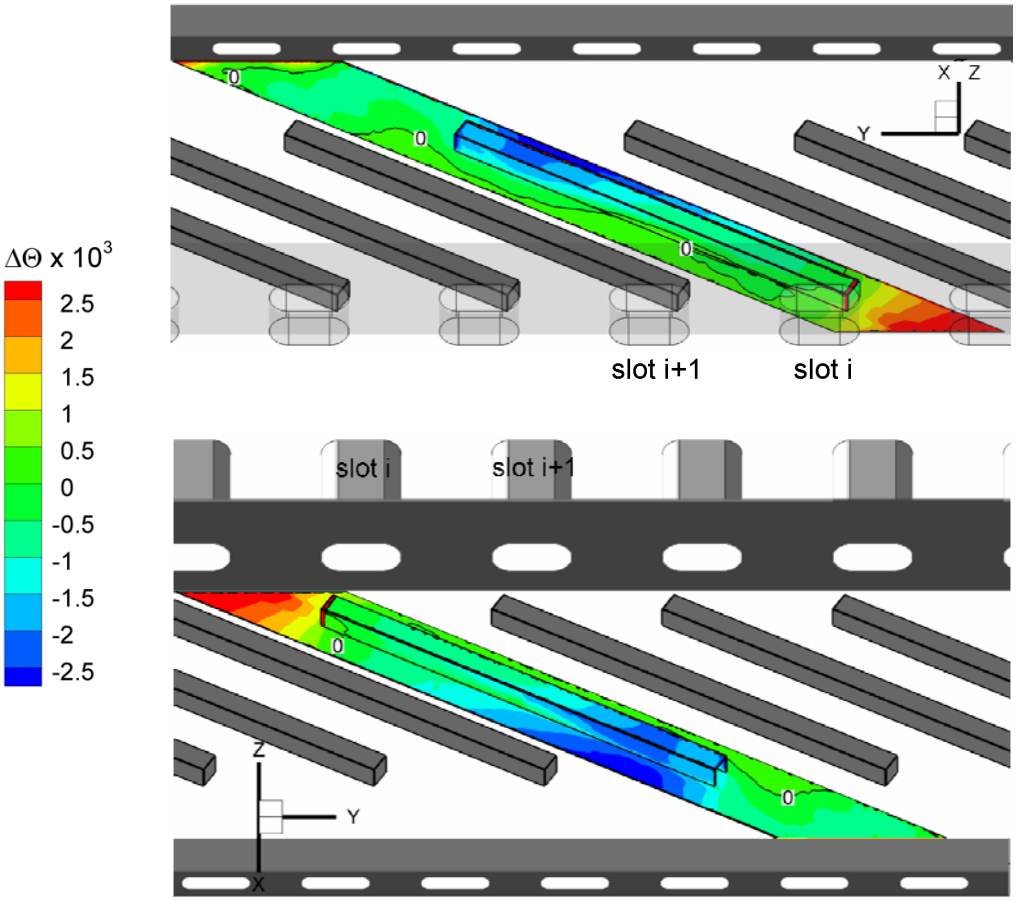


**Fig. 7.4** **Difference of non-dimensional wall temperature between conjugate case and pseudo-conjugate case: inlet view angle (top) and outlet view angle (bottom)**

edge of rib *i*. It is acknowledged that the thermal lifetime of a blade can be halved by a metal temperature increase of 30 K, considering low cycle fatigue. Considering thermal creep, the same reduction in life is provoked by a raise of only 15 K (Ireland (2010)). The large influence of thermal boundary conditions on the heat transfer levels is a consequence of the choice of the reference temperature, which here is taken equal to the inlet flow temperature. However, this is common practice in jet-impingement studies, as a local bulk flow temperature is hard to define unambiguously; the implicit assumption is that such boundary condition effect is often negligible, while the present example shows how significant this effect can be.

Figures 7.5 and 7.6 show cuts of the ribbed wall along planes perpendicular to the floor. Non-dimensional temperature contours and heat flux lines for the different materials are displayed, as computed via the finite element analysis described in section 4.4.3. In Fig. 7.5 the section is perpendicular to the long edge of the turbulator, and located about the first jet impingement area. In Fig. 7.6 the cut is parallel to the long edge of the rib, and divides the obstacle in two. To ease the representation, the non-dimensional temperature is plotted in normalized form as:

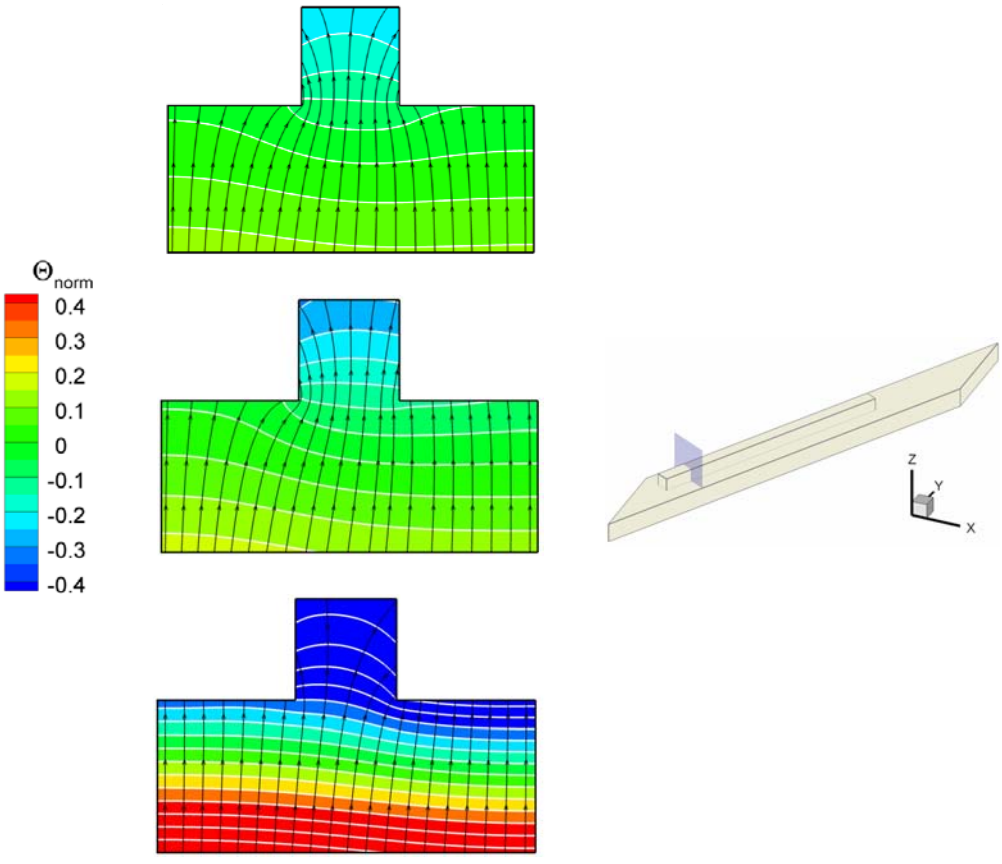


**Fig. 7.5** **Contours of non-dimensional temperature and heat flux lines on a section normal to the ribbed wall and to the long edge of the rib: stainless steel (top), Inconel (middle) and ceramoplastic (bottom). On the right, the location of the cutting plane**

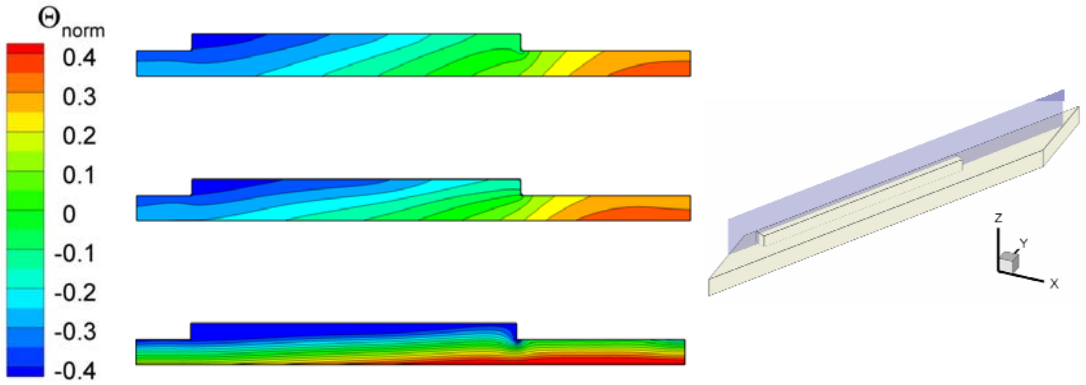


**Fig. 7.6** **Contours of non-dimensional temperature on a section normal to the ribbed wall and parallel to the long edge of the rib: stainless steel (top), Inconel (middle) and ceramoplastic (bottom). On the right, the location of the cutting plane**

$$\Theta_{norm} = \frac{\Theta - \Theta_{avg}}{\Theta_{avg}} \tag{7.1}$$

where $\Theta_{avg}$ is the average non-dimensional wall temperature over the considered section. In Fig. 7.5 the fin effect of the rib (i.e. its capacity of extracting heat from the adjacent wall regions) appears to be strong for the stainless steel; the impingement produces only a slight dissymmetry between impingement side and non-impingement side. The less conductive materials display much higher thermal unbalance, because the thermal resistance contrasts the equalizing effect of the heat conduction. Figure 7.6 demonstrates that in the ceramoplastic slab the temperature gradient across the wall thickness is much stronger than the gradient along the rib length; vice versa, for stainless steel and Inconel the temperature drop across the thickness is comparable to the temperature difference along the rib length.

### 7.1.2 – Nusselt number distribution

Figures 7.7 and 7.8 show the Nusselt number distributions obtained along the rib-roughened wall for the three considered materials. The footprints of the two stronger impingements produced on the rib are evident in all the configurations except for the stainless steel, where lateral conduction smoothes out the thermal spots. With lower thermal conductivity (Inconel, ceramoplastic) the unbalance in heat transfer coefficient between the top of the rib and the side facing the exit becomes apparent.

The direct comparison between the purely convective case and the conjugate configuration with the Inconel wall (for which all the non-dimensional parameters are

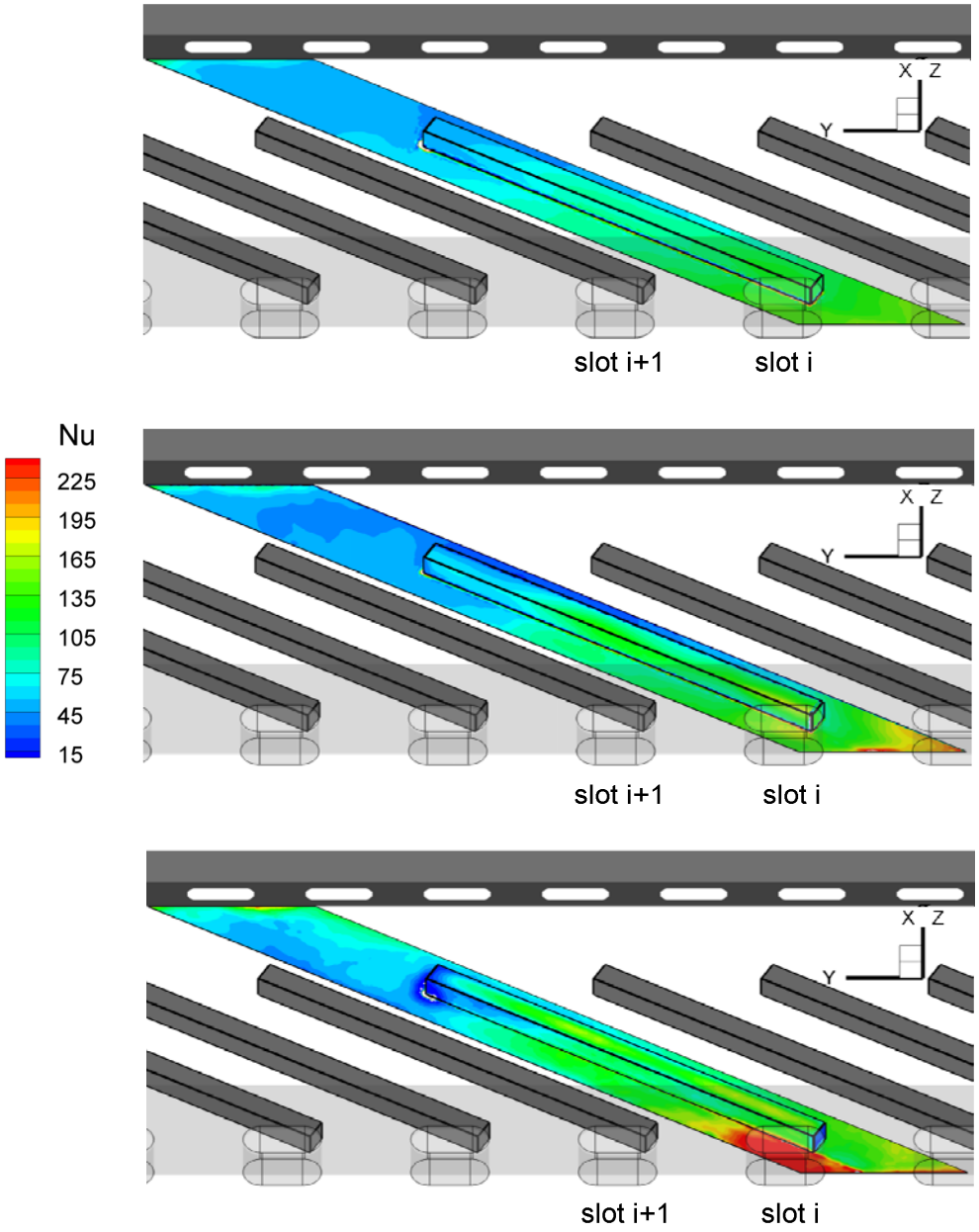


**Fig. 7.7** **Nusselt number distribution in conjugate regime, inlet view angle: stainless steel (top), Inconel (middle), ceramoplastic (bottom)**

engine-representative) is presented in Fig. 7.9, which displays the relative Nusselt number difference in percentage:

$$\Delta Nu = \frac{Nu_{conv} - Nu_{inc}}{Nu_{inc}} \cdot 100 \tag{7.2}$$

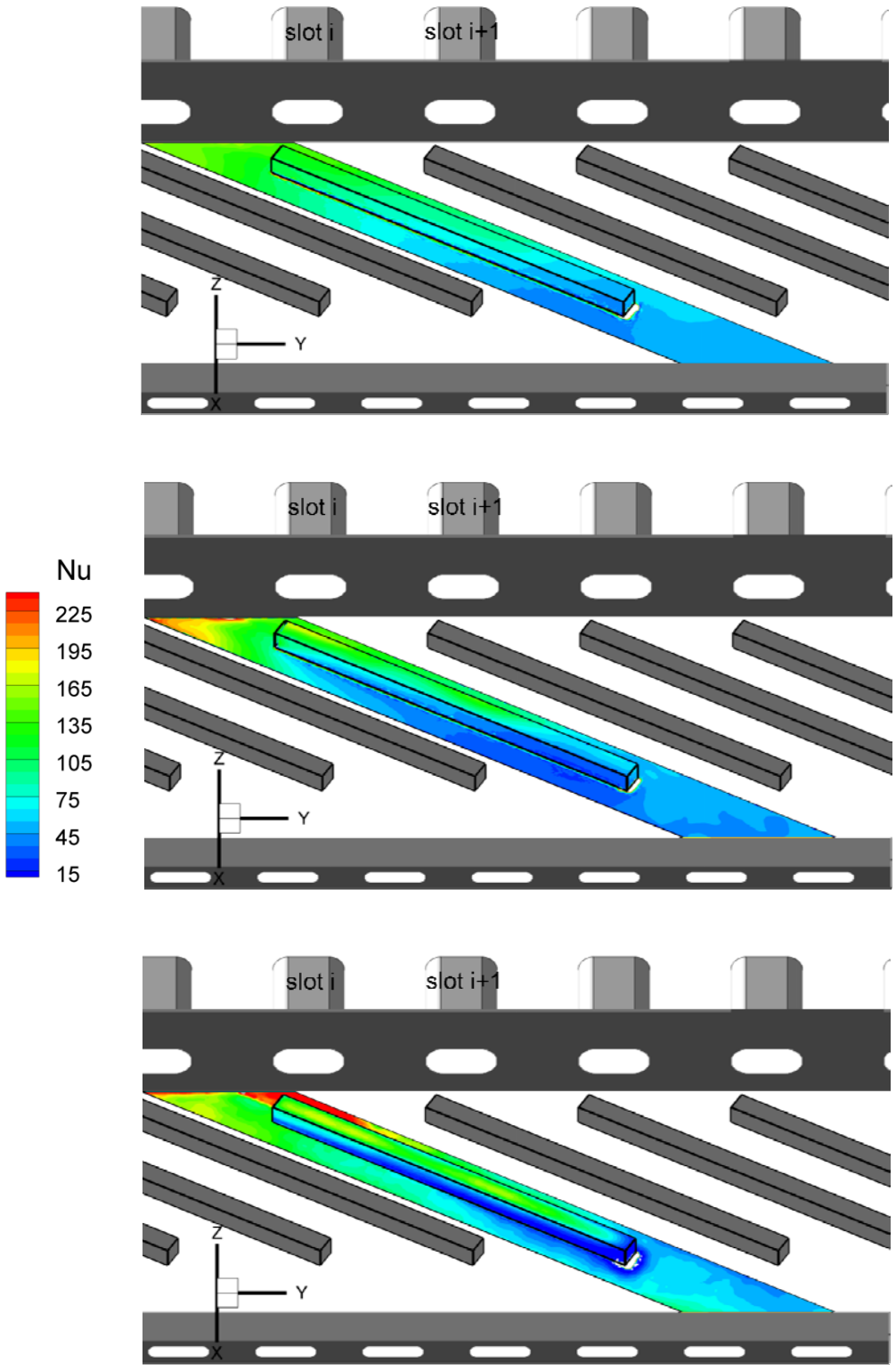


**Fig. 7.8** **Nusselt number distribution in conjugate regime, outlet view angle: stainless steel (top), Inconel (middle), ceramoplastic (bottom)**

The results of the experiments performed in pure convection are off by up to 30% with respect to the conjugate ones; in particular the minimum Nusselt number level, downstream the far end of the rib, is largely overestimated if lateral conduction is neglected. This is consistent with the underestimation of metal temperature in the same area reported in Fig. 7.4. The global area-averaged Nusselt number obtained in convective regime is 25% lower than in the conjugate one.

Overall, assuming a convective regime with uniform heat flux on the ribbed surface leads to a conservative underestimation of the area-average heat transfer rate with respect to the more realistic conjugate regime. However, neglecting the lateral conduction also results in an overestimation of the minimum Nusselt number, and therefore to a dangerous underestimation of the maximum temperature on the investigated surface.

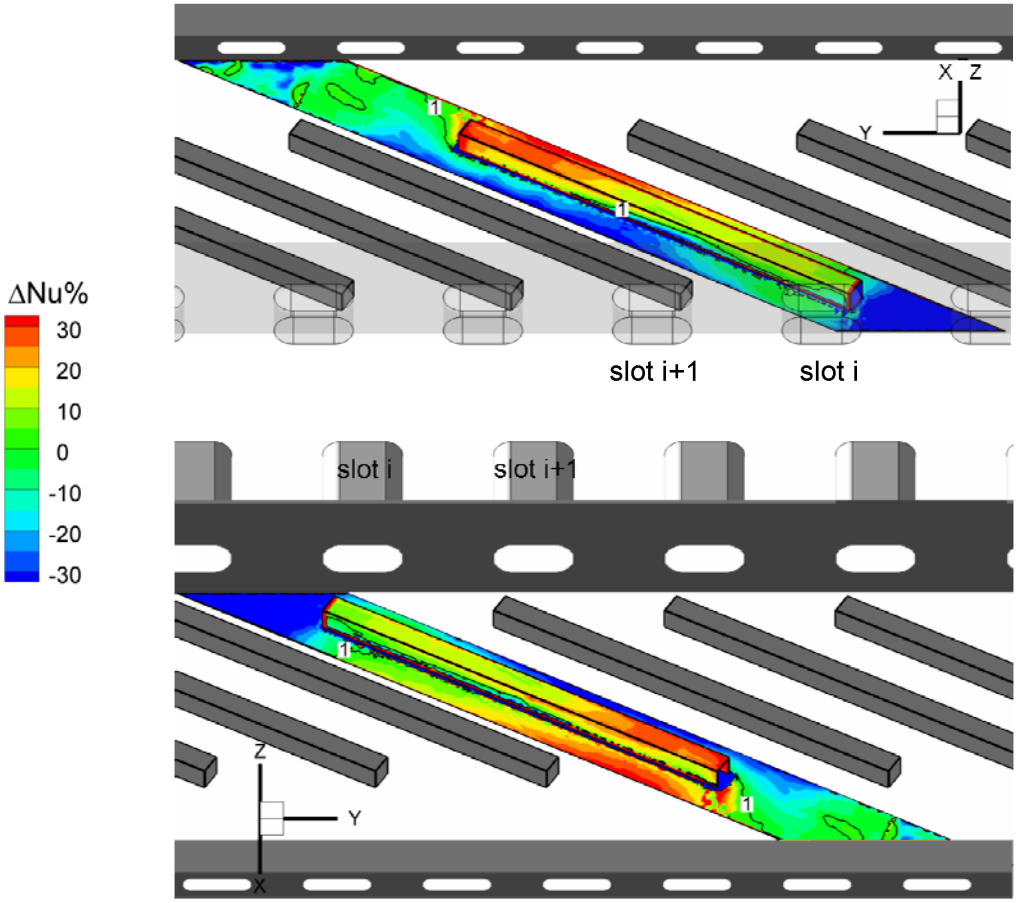


**Fig. 7.9** **Relative difference of non-dimensional wall temperature between conjugate case and pseudo-conjugate case: inlet view angle (top) and outlet view angle (bottom)**

## *7.2 – Global heat transfer performance*

In the following section the global thermal performance of the rib-roughened walls, machined out of the three different materials, is assessed.

In the chart displayed in Fig. 7.10, area-average Nusselt numbers are reported for the different materials and for each investigated surface; the results obtained in purely convective regime are also shown. Overall, the ceramoplastic wall appears to be the one characterized by the highest heat transfer levels. The superior heat transfer levels achieved globally by the less conductive materials are consistent with the theory of convective heat transfer from non-isothermal surfaces (see Kays et al. (2004), Dorfman (2009)). As pointed out by Dorfman (2009), when a non-isothermal surface is exposed to convection, the heat transfer coefficient is higher if the wall temperature increases in the flow direction. This is the case in the present cooling scheme: due to the early location of the main jet impingement, the wall temperature globally raises as the exit wall is approached; among the conjugate cases, a lower solid conductivity produces a higher thermal unbalance, hence a stronger positive temperature gradient in the flow direction, and so higher Nusselt number.

If engine-representative values are assumed for the coolant temperature ($T_f$) and for the external power input to the blade ($Q_0$), the present experimental approach allows evaluating directly the metal temperature in real conditions. Figure 7.11 displays the temperature levels for the three investigated materials, supposing a power input of 1000 $kWm^{-2}$ and a coolant temperature at the channel inlet equal to 1050 K. The chart presents average and maximum values, calculated both along the wet surface and in the complete volume of the rib-roughened wall. Unsurprisingly, the trend of area-average temperature reflects what seen above for the Nusselt number: lower conductivity materials perform better in terms of wall surface heat transfer rate. However, the opposite is true for the temperature peaks on the streamlined surface: as seen in the preceding section, higher thermal resistance determines larger thermal unbalances, and therefore more dangerous hot spots. A low thermal conductivity is

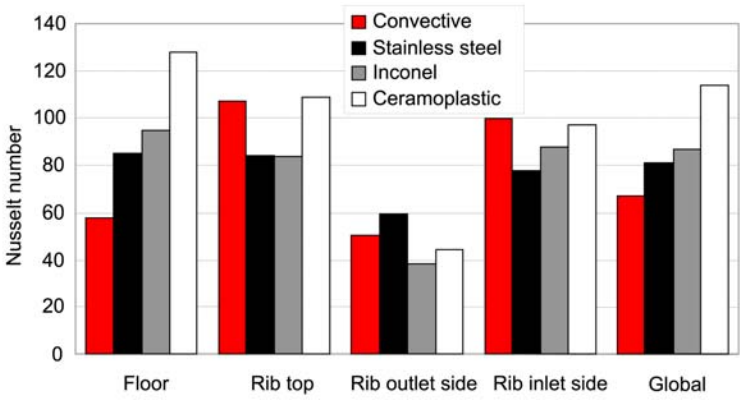


**Fig. 7.10** **Area-averaged Nusselt numbers for the various investigated surfaces and thermal boundary conditions**

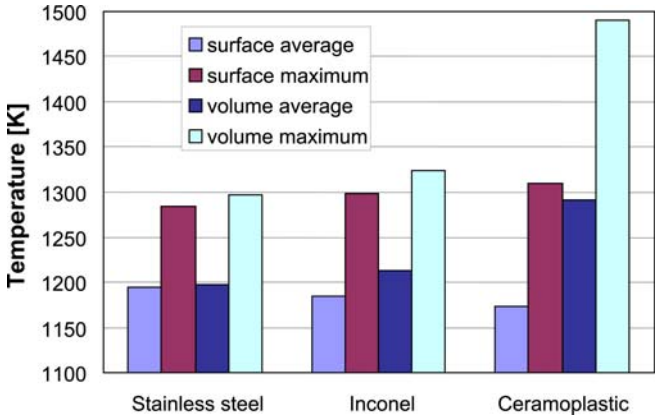


**Fig. 7.11** **Metal temperature at engine conditions, extrapolated from the conjugate heat transfer results for the three investigated materials**

unfavorable also in terms of volume-average: the strong thermal gradient across the wall thickness (see Figs. 7.5 and 7.6) implies that the temperature rapidly reaches alarming levels. This is most clearly shown by the trend for the maximum temperatures in the whole volume (which are in all cases attained at the backside of the wall): choosing materials of very low $k$ is evidently inappropriate.

## *7.3 – Performance of the ribs regarded as cooling fins*

### 7.3.1 – Extended surface heat transfer

In its essence, a rib is a body that extends from the heat transfer surface, aiming at improving the cooling of the component it stems from: in this sense it can be regarded as a cooling fin. In this section the performance of the ribs of the studied cooling configuration will be assessed using concepts borrowed from *extended surface heat transfer*. For more details about this branch of the heat transfer study, the reader is referred to classical heat transfer texts (as Incropera et al. (2006)) and to more specific reviews, as Kraus et al. (2001). Extended surface heat transfer finds its typical application in electronics, in which the approach to thermal management has developed differently, and somehow complementarily, with respect to turbomachinery.

In gas turbine cooling, most of the coolant flows are turbulent: in such a regime there is room for large enhancement of heat transfer coefficient by altering the flow field, through devices that break the boundary layer (ribs and dimples), accelerate the flow by blockage effect (ribs and pins), and in general augment the turbulence transport coefficients. Besides, the turbulators increase the surface area for convective heat transfer; but this is not the primary objective of enhancement (Arik and Bunker (2006)). The focus on the increase of the convective heat transfer coefficient might explain why the turbomachinery community has long overlooked the conjugate heat

transfer problem, as demonstrated by the fact that the largest part of the numerical and experimental studies available in literature are devoted to the study of cooling schemes in purely convective mode.

On the other hand, in electronics packaging cooling, most of the flows are transitional, and heat sinks are the primary choice for thermal management (Arik and Bunker (2006)). Heat sinks absorb and dissipate heat from an object using thermal contact: they increase the area of the transfer surface and the volume of material through which the heat is dissipated, entailing a temperature drop of the object. As the thermal conductivity is increased, the heat transfer performance is enhanced (Ma and Peterson (2002)). Cooling fins in electronics mostly serve as heat sinks.

The present conjugate heat transfer study allows to assess the performance of the ribs regarded as cooling fins, using performance indicators such as fin efficiency and fin effectiveness. This approach, though unconventional for the turbomachinery community, does shed some light on the issue of the influence of thermal conductivity, and confirms some of the conclusions drawn in the previous section.

### 7.3.2 – Fin performance indicators

Let us consider a fin extending from a flat surface (so-called primary surface). The classic cooling fin analysis is based on simplifying assumptions first stated by Harper and Brown (1922) and later extended by Murray (1938) and Gardner (1945), known as the Murray-Gardner assumptions. They are reported here for reference:

1. Steady state regime
2. Homogeneous and temperature-invariant material properties
3. Uniform convective heat transfer coefficient on the fin side
4. Uniform fluid temperature
5. Small fin thickness compared with its height and length, and consequent one-dimensional conduction
6. Uniform fin base temperature
7. No contact resistance between fin base and primary surface
8. No heat sources within the fin itself
9. Adiabatic tip of the fin
10. Heat transfer from the fin proportional to the temperature excess between the fin and the surrounding medium

Such assumptions allow deducing simple analytical expressions for indicators of fin performance, which prove to be useful in guiding design choices of thermal management. However many of these assumptions are non-realistic, especially in forced convection cooling, (e.g. assumption # 3, 5 and 9).

The most commonly used fin performance indicator is the fin efficiency $\eta$, introduced by Harper and Brown (1922): it is defined as the ratio of heat transferred by a fin to the amount of heat transferred by the same fin, if its temperature was uniform and equal to the base temperature (or, equivalently, it the fin was infinitely conductive):

$$\eta = \frac{Q_{fin}}{Q_{fin,id}} \tag{7.3}$$

Figure 7.12 illustrates the concept. The isothermal fin is and ideal condition: if the entire fin was operating at the base temperature, then the fin-to-fluid temperature excess would be maximum, and so would be the extracted heat. By definition $\eta$ varies between 0 and 1.

A less popular but possibly more useful indicator is the fin effectiveness $\varepsilon$ introduced by Gardner (1945): it is defined as the ratio of the heat transferred by a fin to the amount of heat that would be transferred by the primary surface without the fin attached (Fig. 7.13):

$$\varepsilon = \frac{Q_{fin}}{Q_{base}} \tag{7.4}$$

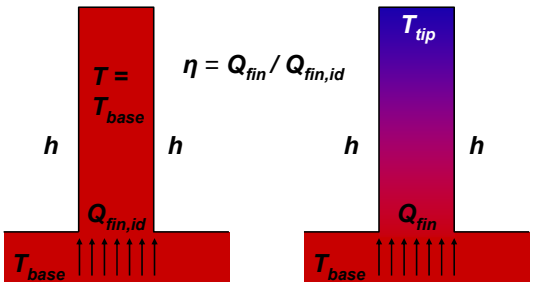


**Fig. 7.12** **Definition of fin efficiency. Left: ideal isothermal fin. Right: real fin**

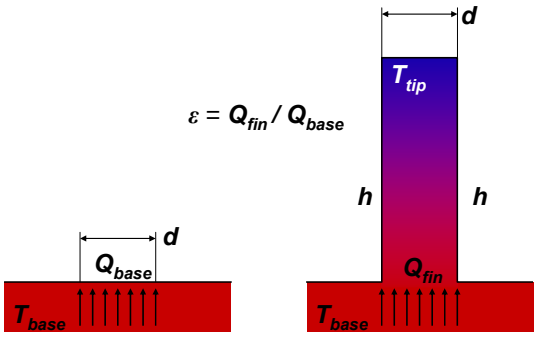


**Fig. 7.13** **Definition of fin effectiveness. Left: primary surface without fin. Right: finned surface**

Fin effectiveness should be larger than 1, otherwise the fin would have an insulating effect. Indeed, economic considerations may indicate that $\varepsilon$ must be considerably greater than unity for the presence of the fin to be justified (Kraus et al. (2001)).

In the ribbed domain considered in the present study, most of the Murray-Gardner assumptions are not valid. However, as the whole thermal pattern within the rib-roughened wall is available, both fin efficiency and fin effectiveness can be directly computed without the use of relations relying on those assumptions. $Q_{fin}$ is obtained integrating the wall heat flux over the surface of the obstacle. As for the fin efficiency, $Q_{fin,id}$ is computed as follows:

$$Q_{fin,id} = A_{rib} h_{avg} \left( T_{base} - T_f \right) \tag{7.5}$$

where $A_{rib}$ is the total wet surface area of the rib, $h_{avg}$ is the heat transfer coefficient averaged over the rib surface, $T_{base}$ is the temperature at the base of the rib, and $T_f$ is the reference fluid temperature. $T_{base}$ is computed by averaging over a section that cuts the rib at the level of the floor. In the expression of the fin effectiveness, $Q_{base}$ should be obtained performing heat transfer measurements in the configuration without ribs, for the same regime as for the ribbed configuration. However, conjugate heat transfer measurements have not been performed in the non-ribbed geometry. Therefore it is simply assumed that the heat transferred by the primary surface without the rib is equal to the heat flux imposed on the backside, multiplied by an area equal to the base section of the rib:

$$Q_{base} = q_0 A_{base} \tag{7.6}$$

The assumption is physically sound, as the effect of wall conduction is much weaker for a flat plate. An analogous approach is followed by Willockx (2009).

Figure 7.14 shows the rib performance in terms of fin efficiency and fin effectiveness for the three investigated materials. As one can see both indicators confirm that the high conductive materials are preferable. Actually, the fin effectiveness for the ceramoplastic hardly exceeds unity: this would suggest that, considering only the benefit of the obstacle as heat sink, inserting the rib might not be worthy for such a low conductivity material. Similar conclusions can be drawn observing the distribution of heat extracted by the wall surfaces for the different employed material, displayed in Fig. 7.15: the lower the material conductivity, the smaller the relative rib contribution to the heat extraction.

Of course, care must be taken when applying fin performance analysis to characterize ribbed cooling channels: the performance indicators for extended surface are conceived to qualify cooling systems which are much different from airfoil cooling cavities. In electronics packaging cooling, which is the primary field of application of these concepts, it is generally assumed that the presence of the fins does not alter the heat transfer coefficient. The parameters to be optimized are the fin height, shape (i.e. the cross-section variation with height) and conductivity. The designer has a certain freedom in this sense, being limited essentially by the need of minimizing the weight

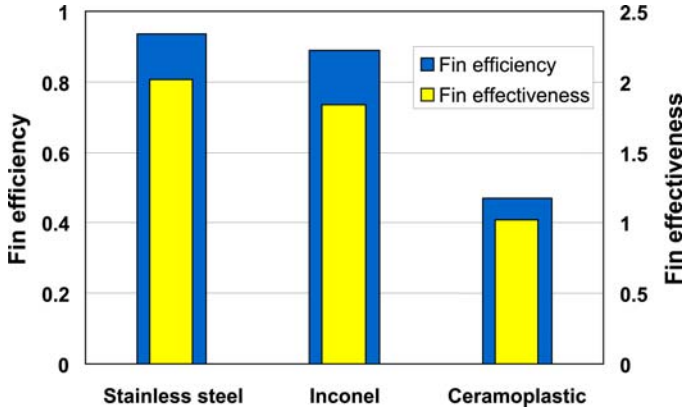


**Fig. 7.14** **Fin efficiency and fin effectives of the investigated rib for the three employed materials**

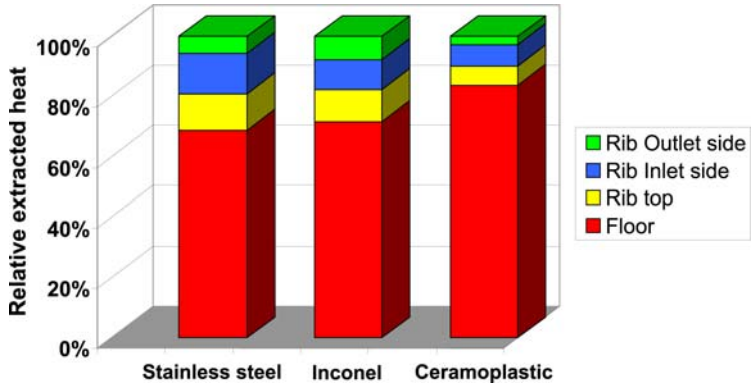


**Fig. 7.15** **Relative contribution of the various heat transfer surfaces to the extracted heat for the three investigated materials**

and volume of the component. In turbomachinery on the other hand, the internal cooling system designer faces a very different problem: the height of the turbulators is strongly limited by the pressure losses that large obstacles would produce; as matter of fact, ribs are very short compared to classic cooling fins. Most importantly, in blade cooling the insertion of the protrusions is instrumental for enhancing the heat transfer coefficient. Finally, the conductivity of the ribs is necessarily the same as the rest of the airfoil (the possibility of using inserts of different materials is not considered here) therefore is a consequence of the selection of the blade material; the latter choice in turn is forced by the requirement that the airfoil must withstand certain mechanical and thermal stresses.

All the above notwithstanding, the qualitative indication is still valid: lower conductivity materials performs better, both from the standpoint of the minimizing the metal temperature (see section 7.2), and from the standpoint of maximizing the usefulness of the ribs. The turbulators are anyway instrumental in increasing the

convective transfer as they act on the velocity field, but make a poorer job as heat sinks if less conductive materials are employed. No need to say, the high conductivity recommendation is also gainful in the sense of reducing the detrimental temperature gradients.

# Chapter 8 – Conclusions

An internal cooling scheme representative of a channel located in the trailing edge area of a turbine airfoil has been investigated experimentally. The cooling scheme is a combination of impingement cooling and internal forced convection cooling. The study addresses both the flow field and the heat transfer, as only the simultaneous examination of both aspects can lead to a true understanding of the cooling performance.

The distinctive characteristics of the tested geometry are:

- the trapezoidal cross-section
- the flow path, in which the coolant crosses the channel transversally, entering from a first row of slots along one wall and exiting from a second row of slots along the opposite wall
- the jet impingements produced by the flow issued from the inlet slots
- the inclined ribs mounted on the wall where the jets impinge

Analyzing such a non-academic configuration, the large amount of information available in literature concerning friction coefficients, flow features and heat transfer patterns can hardly serve for comparison. The only previous case resembling the present scheme was studied by Taslim et al. (1998), who however did not look at the flow field, and reported only average values of heat transfer levels on the ribs.

The Reynolds number, defined at the inlet of the test section, is equal to $Re$ = 67500, representative of today's engine development technology. The regular spacing of inlet slots and ribs results in a spatially periodic aero-thermal behavior over most of the channel. Maximum variations of 4% in inlet jets static pressure and 6% in exit jets velocity are found. Therefore the experimental efforts have been focused on the central part of the cavity, which is considered representative of most of the cooling scheme.

The main achievements are summarized and briefly discussed below. The goals stated in Chapter 1, i.e. the characterization of the flow field, the evaluation of the convective heat transfer performance and its dependence on the wall conduction, have been achieved. Firstly, it has been demonstrated that, in such a complex configuration, a detailed analysis of the aero-thermal field is needed both to understand the aero-thermal performance and to improve the cooling capabilities of a given scheme. Furthermore, it has been confirmed that the ribs contribute majorly to the heat transfer, although they also cause the appearances of hot spots on their surface and along the adjacent floor. Finally, it has been shown that the thermal levels associated to the realistic thermal boundary conditions (determined by the conjugate heat transfer regime) differ significantly with respect to the purely convective case (with uniform heat flux imposed on the rib-roughened surface).

## *8.1 – Aerodynamic investigation*

The pressure drop across the test section is mainly attributed to the perforated wall separating inlet cavity and trailing edge cavity; no appreciable pressure penalty is generated by the rib insertion. This conclusion is clearly limited to the studied arrangement of the turbulators: a consistently larger blockage would produce undoubtedly higher aerodynamic losses. However it is clear that the classic friction factor definition is not meaningful in the present geometry, which differs substantially from a conventional, tubular channel.

A thorough investigation of the flow field has been performed. The main flow structures have been identified and characterized by means of particle image velocimetry, allowing to deduce a model of the mean flow. Each jet impinges on the three ribs in front of the slot, and the jet-rib interaction produces two upward deflections in each inter-rib domain, resulting in secondary impingement on the opposite smooth wall. The guidance of the inclined ribs drives the bulk of the coolant towards the tip of the blade; this is balanced by a recirculation of low momentum flow directed towards the blade hub, streaming above the row of crossing-jets. The velocity field is completely three-dimensional and several measurements plane with different orientations were needed to qualify all the main flow features.

## *8.2 – Convective heat transfer investigation*

Distributions of heat transfer coefficient (non-dimensionalized as Nusselt number) are obtained by liquid crystals thermography on the rib-roughened surface as well as on the opposite smooth wall with a purely convective regime (uniform heat flux imposed at the solid-fluid interface). It is widely acknowledged that the surface of the obstacles contributes significantly to the total heat extraction from a rib-roughened wall, and that the heat transfer level on the turbulators is significantly higher than elsewhere in the cooling channel. However practical difficulties often prevent measuring heat transfer coefficients on the rib themselves. To the author best knowledge, the level of detail of the Nusselt number maps reported in the present effort on the surface of the turbulators is matched in open literature only by Çakan (2000).

The thermal patterns on the channel walls show footprints of the flow features detected by velocimetry: impingements on the rib and along the adjacent floor, lift-off of the rebounded jets and secondary impingements and separation lines on the opposite smooth wall. The heat transfer enhancement on the smooth wall, due to the presence of the obstacles on the ribbed wall, is remarkable. Globally the top side of the rib shows the highest Nusselt number among the investigated surfaces. However, the presence of the turbulators determines an alarming hot spot in the area of the floor close to the far end of the rib: the latter prevents the fluid from efficiently cooling this portion of the wall; as matter of fact, the area-averaged heat transfer coefficient on the

inter-rib floor is higher in the configuration without ribs. However the insertion of the ribs enhances the global heat transfer coefficient (averaged on all surfaces) by 14%. Interestingly, a large part of this gain is achieved on the smooth wall opposite to the rib-roughened wall, where the heat transfer coefficient is enhanced by almost 20%.

The identified aero-thermal features suggest a certain margin for improvement of the aero-thermal performance by varying one or more geometrical parameters. Given the complexity of the geometry, the possible matrix of cases is enormous. Instead of exploring tens of possibilities (with unavoidable loss of detail in the description), the analysis has focused on three additional configurations which appeared promising, obtained tapering and/or shifting the ribs with respect to the slots position. Both expedients prove to be useful in reducing the extent and intensity of the aforementioned hot spot in the vicinity of the rib. Moreover such geometrical modifications, altering the jet-rib interaction and the consequent upward flow motion, result beneficial also for the cooling of the opposite smooth wall. The heat transfer results on the modified geometries are consistent with the qualitative mean flow models deduced from surface streamlines flow visualizations. The highest improvement is obtained by tapering the ribs: this reduces the blockage in the region of the channel of minimum cross-section, and an enhancement of about 20% is achieved with respect to the standard rib-roughened configuration. The smooth wall opposite to the ribbed one is the area where the largest improvement is realized, the heat transfer coefficient being enhanced by 20%

## *8.3 – Conjugate heat transfer investigation*

The thermal behavior of the ribbed wall has also been investigated for the conjugate heat transfer regime in order to study the effect of the wall conduction on the thermal levels. Matching the solid-to-fluid thermal conductivity ratio found in an engine provides the correct thermal boundary conditions, independently from the choice of the reference fluid temperature, and gives full similarity between the laboratory model and the engine reality. In this regard, it has been shown that if Ni-based super-alloys are used for the wall experiencing conjugate heat transfer in laboratory tests, the conductivity ratio naturally matches the one observed in engine conditions, no matter the temperature level of the tests.

Infrared thermography coupled to a finite element analysis is used to retrieve not only the wall temperature, but also the whole thermal pattern through the considered rib-roughened wall. An iterative routine is applied to reduce the sensitivity of the computed heat flux from the unavoidable measurement errors. Highly spatially resolved distributions of non-dimensional temperature and Nusselt number are obtained on the rib-roughened wall of the cooling channel, including the rib surface. A dimensional analysis shows that both Nusselt number and non-dimensional wall temperature are appropriate descriptors of the phenomenon, provided that Reynolds number, Prandtl number and solid-to-fluid thermal conductivity ratio are engine-representative, as it is the case here. Nusselt number levels in purely convective

regime are off by up to 30% locally and 25% globally with respect to the conjugate results. If the heat transfer coefficient distribution obtained with uniform heat flux is applied in a conduction calculation, the wall temperature is largely misestimated with respect to the conjugate results: the maximum surface temperature is underestimated by 26 to 33 K at engine conditions, which would lead to an overestimation of the blade life by more than 100%.

When decreasing the wall thermal conductivity, the overall heat transfer coefficient on the ribbed surface increases, since the streamwise temperature gradient along the wet surface is augmented. However this amplifies local temperature gradients which are detrimental for the component integrity. Moreover, temperature peaks both on the cooled surface and within the wall are higher if less conductive materials are employed. The thermal performance of the rib is additionally assessed by means of parameters classically used for extended surface heat transfer: both fin efficiency and fin effectiveness suggest that the turbulators are more proficient if more conductive materials are employed.

## *8.4 – Recommendations for further investigations*

The conjugate heat transfer analysis has shown the decisive impact of the thermal boundary conditions on the convective heat transfer levels. In fact, the performed study can be considered fully realistic only if the imposed uniform heat flux at the outer side of the wall (i.e. the external surface of the blade) is a realistic representation of the engine reality. Indeed the external heat transfer coefficient varies less abruptly on the external side of the blade than along the internal cooling channel surface. However, coupling the three heat transfer processes of external convection, through-wall conduction and internal convection is the natural development of the present investigation: the effect of streamlining the outer side of the conductive ribbed wall with high temperature flow is to be studied.

An analysis of the impact of wall conduction and thermal boundary conditions concerns quite fundamental questions in heat transfer. A more canonical (and less complex) geometry would lead to more general conclusions. In the author's opinion, a ribbed channel of rectangular cross section, having one wall provided with ribs normal to the floor would be a good test case. The effect of wall conduction would be even more decisive if bleed holes were added on the inter-rib floor.

As the cooling scheme in object can be employed in rotor blades as well as in vanes, the effects of rotations are worth investigating. The flow field, already very complex, would be altered by the secondary flows and the (de)stabilizing effect induced by the Coriolis and centrifugal buoyancy forces, affecting in turn the heat transfer.

From the experimental standpoint, the strongly three-dimensional nature of the flow causes considerable difficulties in performing standard 2D-PIV due to strong out-of-plane velocities. Stereoscopic PIV on the other hand proved to be a suitable tool for investigating complex flows in internal cooling channels (Chanteloup et al. (2002)).

As for the numerical methods for prediction, the *k-l* model has shown reasonable agreement with the present experiments (see Armellini et al. (2010) and Coletti et al. (2008) listed in Appendix B). However, topological differences in the flow and local mispredictions of the Nusselt number up to 50% have been found. Reynolds stress models have proven to be significantly more successful than two-equation models in situations relevant for internal blade cooling as wall heat transfer and swirling/rotating flows (Younis (2010)), with a relatively modest increase in computational cost. The present results represent a realistic test case for the assessment of the performance of such models with respect to eddy viscosity models.

# References


Acharya S., Saha K., Segura D. (2010) Internal Cooling of Turbine Blades: Geometry and Rotation Effect. In: Internal Cooling in Turbomachinery. VKI Lecture Series, von Karman Institute for Fluid Dynamics, Rhode-St-Genèse, Belgium

Adrian, R.J. (1991) Particle-Imaging Techniques for Experimental Fluid Mechanics. Annual Review of Fluid Mechanics 23:261-304

Agostini F., Arts T. (2005) Conjugate Heat Transfer Investigation of a Rib-Roughened Cooling Channel. ASME Paper GT-2005-68166, ASME Turbo Expo 2005, Reno, Nevada, USA

Akino N., Kunugi T., Ichimiya K., Mitsushiro K., Ueda M. (1989) Improved Liquid-Crystal Thermometry Excluding Human Color Sensation 111:558-565

Anderson A., Moffat R.J (1992) The Adiabatic Heat Transfer Coefficient and the Superposition Kernel Function: Part I – Data for Arrays of Flatpacks for Different Flow Conditions. Journal of Electronic Packaging 11:14-21.

Arik M., Bunker R. S. (2006) Electronics Packaging Cooling: Technologies From Gas Turbine Engine Cooling. Journal of Electronic Packaging 128:215-225

Armellini A. (2007) Aero-thermal Investigation of a Rib-Roughened Trailing Edge Channel With Crossing-Jets. VKI DC Report, von Karman Institute for Fluid Dynamics, Rhode-St-Genèse, Belgium

Astarita T., Cardone G., Carlomagno G.M., Meola C. (2000) A Survey on Infrared Thermography for Convective Heat Transfer Measurements. Optics & Laser Technology 32:593-610

Ballal D.R., Zelina J. (2004) Progress in Aero-engine Technology (1939-2003)" Journal of Aircraft 41:43-50

Batchelder K., Moffat R.J. (1997) Towards a Method for Measuring Heat Transfer in Complex 3-D Flows. Technical Report TSD-108, Stanford University, California, USA.

Baughn J.W., Takahashi R.K., Hoffman M.A., McKillop, A.A. (1985) Local Heat Transfer Coefficient Measurements Using an Electrically Heated Thin Gold-Coated Sheet. Journal of Heat Transfer 107:953-959

Bendat J.S., Piersol A.G. (1986) Random Data: Analysis and Measurements Procedures. Wiley, New York

Bertier N., Courbet B., Dutoya D., Vuillot F., (2004) Large-Eddy Simulation of a Subsonic Flow over a Cavity on General Unstructured Grids. AIAA Paper 2004-0679, 42nd AIAA Aerospace Sciences Meeting & Exhibit, Reno, Nevada, USA

Buchlin, J.-M. (2009) Convective heat transfer and infrared thermography (IRTh). Journal of Applied Fluid Mechanics 3:55-62

Buckingham E. (1914) On Physically Similar Systems; Illustrations of the Use of Dimensional Equations. Physical Review 4:345-376

Bunker R.S., Metzger D.E. (1990) Local Heat Transfer in Internally Cooled Turbine Airfoil Leading Edge Regions – Part I: Impingement Cooling Without Film Coolant Extraction. Journal of Turbomachinery 112:451-458.

Bunker R.S. (2004) Latticework (Vortex) Cooling Effectiveness Part 1: Stationary Channel Experiments. ASME Paper GT-2004-54157, ASME Turbo Expo 2004, Vienna, Austria

Bunker R.S. (2006) Cooling Design Analysis. In: The gas turbine handbook, US Department of Energy, National Energy Technology Laboratory, USA

Çakan M (2000) Aero-thermal investigation of fixed Rib-roughened internal cooling passages. Ph.D. dissertation, von Karman Institute for Fluid Dynamics and Université Catholique de Louvain, Belgium

Camci C., Kim K., Hippensteele S.A., (1992) A New Hue Capturing Technique for the Quantitative Interpretation of Liquid Crystal Images Used in Convective Heat Transfer Studies. Journal of Turbomachinery 114:765-775

Carbonaro M. (1994) Flow Visualizations. In: Measurement Techniques in Fluid Dynamics. VKI Lecture Series, von Karman Institute for Fluid Dynamics, Rhode-St-Genèse, Belgium

Casarsa L., Arts T. (2005) Experimental Investigation of the Aerothermal Performance of a High Blockage Rib-Roughened Cooling Channel. Journal of Turbomachinery 127:580-588

Castleman K.R. (1995) Digital Image Processing. 2nd edition, Prentice Hall

Cervenka M. (2000) Trent 800 Breakdown With Pressure and Temperature Considerations. Rolls-Royce Group plc, Derby, UK

Chambers A.C., Gillespie D.R.H., Ireland P.T., Dailey G.M. (2003) A Novel Transient Liquid Crystal Technique to Determine Heat Transfer Coefficient Distributions and Adiabatic Wall Temperature in a Three-Temperature Problem. Journal of Turbomachinery 125:538-546

Chandra P.R., Han J.-C., Lau S.C. (1988) Effect of Rib Angle on Local Heat/Mass Transfer Distribution in a Two-Pass Rib-Roughened Channel. Journal of Turbomachinery 110:233-241

Chanteloup D., Juaned Y., Bölcs A. (2002) Combined 3-D Flow and Heat Transfer Measurements in a 2-Pass Internal Coolant Passage of Gas Turbine Airfoils. Journal of Turbomachinery 120:368-375

Chapra S., Canale R. (2005) Numerical Methods for Engineers. 5th ed., McGraw-Hill, New York.

Chevalier P., Courbet B., Dutoya D., Klotz P., Ruiz E., Troyes J., Villedieu P. (2005) CEDRE: Development and Validation of a Multiphysics Computational Software. 1st European Conference for Aerospace Sciences (EUCASS), Moscow, Russia

Choi J., Mhetras S., Han J-C., Lau S. C., Rudolph R. (2008) Film Cooling and Heat Transfer on Two Cutback Trailing Edge Models With Internal Perforated Blockages. Journal of Heat Transfer 130:012201 (13 pages)

Chyu M.-K. Natarajan V. (1996). Local Heat/Mass Transfer Distributions on the Surface of a Wall-Mounted Cube. Journal of Heat Transfer 113:851-857

Collings P., Hird M. (1997) Introduction to Liquid Crystals, Taylor & Francis Inc., Philadelphia

Dano B.P., Liburdy J.A., Kanokjaruvijit K. (2005) Flow Characteristics and Heat Transfer Performances of a Semi-Confined Impinging Array of Jets: Effect of Nozzle Geometry. International Journal of Heat and Mass Transfer 48:691-701

Dorfman A. (2009) Conjugate Problems in Convective Heat Transfer. Taylor & Francis, New York

Ekkad S.V., Huang Y., Han J.-C. (2000) Impingement Heat Transfer Measurements Under an Array of Inclined Jets. AIAA Journal of Thermophysics and Heat Transfer 14:286-288

Fabry E. (1998) Development of 3D Stereoscopic Holographic Particle Image Velocimetry With a View to Applications in Turbomachinery Field. Ph.D. dissertation, von Karman Institute for Fluid Dynamics and Université Catholique de Louvain, Belgium

Facchinetti E. (2008) Heat Transfer Investigation in Turbine Blade Trailing Edge Internal Cooling Channel. VKI STP Report, von Karman Institute for Fluid Dynamics, Rhode-St-Genèse, Belgium

Faghri M., Sparrow E.M. (1980) Simultaneous Wall and Fluid Axial Conduction in Laminar Pipe-Flow Heat Transfer. Journal of Heat Transfer 102:58-63

Farina D.J., Hacker J.M., Moffat R.J., Eaton J.K. (1994) Illuminant Invariant Calibration of Thermochromic Liquid Crystals. Experimental Thermal and Fluid Science 9:1-12

Fedorov A.G., Viskanta R. (2000) Three Dimensional Conjugate Heat Transfer in the Microchannel Heat Sink for Electronic Packaging. International Journal of Heat and Mass Transfer 43:399-415

Fedrizzi R., Arts T. (2004) Investigation of the Conjugate Conductive-Convective Thermal Behavior of a Rib-Roughened Internal Cooling Channel. ASME Paper GT2004-53046, ASME Turbo Expo 2004, Vienna, Austria

Fergason, J. (1966) Cholesteric Structure – I. Molecular Crystals 1:293–307

Fergason J. (1968) Liquid Crystals in Nondestructive Testing. Applied Optics 7:1729–1737

Fiala N.J., Jaswal I., Ames F.E. (2010) Letterbox Trailing Edge Heat Transfer: Effects of Blowing Rate, Reynolds Number, and External Turbulence on Heat Transfer and Film Cooling Effectiveness. Journal of Turbomachinery 132:011017 (10 pages)

Florschuetz L.W., Berry R.A., Metzger D.E. (1980) Periodic Streamwise Variations of Heat Transfer Coefficients for Inline and Staggered Arrays of Circular Jets With Crossflow of Spent Air. Journal of Heat Transfer 102:132-137

Foucaut J.M., Carlier J., Stanislas M. (2004) Measurement Science and Technology 15:1046- 1058

Gardner K. A. (1945) Efficiency of Extended Surfaces. Journal of Heat Transfer 67:621-631

Gaussorgues G. (1994) Infrared thermography. Chapman & Hall, London

Gillespie D.R.H., Wang Z., Ireland P.T., Kohler S.T. (1998) Full Surface Local Heat Transfer Coefficient Measurements in a Model of an Integrally Cast Impingement Cooling Geometry. J. of Turbomachinery 120:92-99

Gillespie D.R.H., Ireland P.T., Dailey G.M. (2000) Detailed Flow and Heat Transfer Coefficient Measurements in a Model of an Internal Cooling Geometry Employing Orthogonal Intersecting Channels. ASME Paper 2000-GT-653, ASME Turbo Expo 2000, Munich, Germany

Hallcrest Ltd. (1991) Handbook of Thermochromic Liquid Crystal Technology. United Kingdom

Han B., Goldstein, R. J. (2001) Jet-Impingement Heat Transfer in Gas Turbine Systems, Annals of the New York Academy of Sciences, 934:147–161

Han J.-C. (1984) Heat Transfer and Friction in Channels With Two Opposite Rib-Roughened Walls. Journal of Heat Transfer 106:774-781

Han J.-C., Dutta S., Ekkad, S.V. (2000). Gas Turbine Heat Transfer and Cooling Technology. Taylor and Francis, New York

Han J.-C., Glicksman L.R., Rohsenow W.M. (1978) An Investigation of Heat Transfer and Friction for Rib-Roughened Surfaces. International Journal of Heat and Mass Transfer 21:1143:11156

Harper D. R., Brown W.B. (1922) Mathematical Equations for Heat Conduction in the Fins of Air-Cooled Engines. NACA Report No. 158

Heselhaus A. (1998) A Hybrid Coupling Scheme and Stability Analysis for Coupled Solid/Fluid Turbine Blade Temperature Calculations. ASME Paper 98-GT-88, ASME Turbo Expo, Stockholm 1998, Sweden

Hoefler F., Schueren S., von Wolfersdorf J., Naik, S. (2010) Heat Transfer Characteristics of an Oblique Jet Impingement Configuration in a Passage with Ribbed Surfaces, ASME Paper GT2010-22288, ASME Turbo Expo 2010, Glasgow, UK

Iaccarino G., Ooi A., Durbin P.A., Behnia M. (2002) Conjugate Heat Transfer Prediction in Two-Dimensional Ribbed Passages. International Journal of Heat and Fluid Flow 23:340-345

Iacovides H., Jackson D.C., Kelemenis G., Launder B.E. (2001) Flow and Heat Transfer in a Rotating U-Bend With 45° Ribs. International Journal of Heat and Fluid Flow 22:308-314

Iacovides H., Launder B.E. (2007) Internal Blade Cooling: the Cinderella of Computational and Experimental Fluid Dynamics Research in Gas Turbines. Proceedings of IMechE- Part A: Journal of Power and Energy 221:265-290

Incropera F.P., Dewitt D.P., Bergman T.L., Lavine A. (2006) Fundamentals of Heat Transfer. 6th ed., John Wiley & Sons, New York

Ireland P.T., Jones T.V. (2000) Liquid Crystal Measurements of Heat Transfer and Surface Shear Stress. Measurement Science and Technology 11:969-986

Ireland, P.T. (2010) Aerothermal Performance of Blade Cooling Systems. In: Internal Cooling in Turbomachinery. In: Internal Cooling in Turbomachinery. VKI Lecture Series, von Karman Institute for Fluid Dynamics, Rhode-St-Genèse, Belgium

Kaye, G.W.C., Laby T.H. (1995) Tables of Physical and Chemical Constants. Longman Sc. & Tech., New York

Kays W., Crawford M., Weigand B. (2004) Convective Heat and Mass Transfer. 4th ed., McGraw-Hill, New York.

Keane R.D., Adrian R.J. (1990) Optimization of Particle Image Velocimeters. I. Double Pulsed Systems. Measurements Science and Technology 1:1202-1215

Kiml R., Mochizuki S., Murata, A. (2001) Effects of Rib Arrangements on Heat Transfer and Flow Behaviour in a Rectangular Rib-Roughened Passage: Application to Cooling of Gas Turbine Blade Trailing Edge. Journal of Turbomachinery 123:675-681

Kline S.J., McClintok F.A. (1953) Describing Uncertainties in Single Sample Experiments. Mechanical Engineering Journal 75:3-8.

Koff B.L. (1991) Spanning the Globe with Jet Propulsion. AIAA Annual Meeting, Arlington, Virginia

Korotky G.J., Taslim M.E. (1998) Rib Heat Transfer Coefficient Measurements in a Rib-Roughened Square Passage. Journal of Turbomachinery 120:376-385

Kraus A. D., Aziz A., Welty J. (2001) Extended Surface Heat Transfer. the ed., John Wiley & Sons, New York

Landau L.D., Lifschitz E.M., (200) Fluid Mechanics. 2nd ed. Volume 6 of Course of Theoretical Physics

Langston L. S., Boyle M.T (1982) A New Surface-streamline Flow-visualization Technique, Journal of Fluid Mechanics 125:53-57

Lakshminarayana B. (1996) Fluid Dynamics and Heat Transfer of Turbomachinery. John Wiley & Son, New York

Ligrani P., Mahmood G.I. (2003) Spatially Resolved Heat Transfer and Friction Factors in a Rectangular Channel With 45-Deg Angled Crossed-Rib Turbulators. Journal of Turbomachinery 125:575-584

Lin M., Wang T. (2001) A Transient Liquid Crystal Method Using a 3-D Inverse Transient Conduction Scheme. International Journal of Heat and Mass Transfer 45:3491-3501

Liou T.-M., Hwang J.-J (1992) Turbulent Heat Transfer Augmentation and Friction in Periodic Fully Developed Channel Flows, Journal of Heat Transfer 114:56-64

Liou T.-M., Hwang J.-J (1993) Effect of Ridge Shapes on Turbulent Heat Transfer and Friction in a Rectangular Channel. International Journal of Heat and Mass Transfer 36:931-940

Liou T.-M., Chen S.-H. (1998) Turbulent Heat and Fluid Flow in a Passage Disturbed by Detached Perforated Ribs of Different Heights. International Journal of Heat and Mass Transfer 41:1795-1806

Luikov A.V., Aleksashenko V.A., Aleksashenko A.A (1971) Analytical Methods of Solution of Conjugated Problems in Convective Heat Transfer. International Journal of Heat and Mass Transfer 14:1047-1056

Ma H.B., Peterson G.P. (2002) The Influence of the Thermal Conductivity on the Heat Transfer Performance in a Heat Sink Journal of Electronic Packaging 124:164-169

Martini P., Schulz A. Bauer H.-J. (2006) Film Cooling Effectiveness and Heat Transfer on the Trailing Edge Cutback of Gas Turbine Airfoils With Various Internal Cooling Designs Journal of Turbomachinery 128:196-205

Martiny M. (1999) Wärmeübergang in effusionsgekühlten Flammrohrwänden. Ph.D. dissertation, University of Karlsruhe, Germany

Merzkirch W. (1987) Flow visualization. 2nd ed., Academic Press, New York.

Metzger D.E., Chyu M.-K., Bunker R.S. (1988) The Contribution of On-Rib Heat Transfer Coefficients to Total Heat Transfer from Rib-Roughened Surfaces. In: Transport Phenomena in Rotating Machinery, J. H. Kim (ed.), Hemisphere Publishing, Washington D.C.

Meynart R. (1979) Flow Velocity Measurement by a Speckle Method. Proceedings of the 2nd European Congress on Optics Applied to Metrology, Strasbourg, France

Moffat R.J. (1988) Describing the Uncertainties in Experimental Results. Experimental Thermal and Fluid Science 1:3-17

Moffat R.J. (1998) What's new in convective heat transfer? International Journal of Heat and Fluid Flow 19:90-101

Montenay A., Paté L., Duboué J.M. (2000) Conjugate Heat Transfer Analysis of an Engine Internal Cavity. ASME Paper 2000-GT-282, ASME Turbo Expo 2000, Munich, Germany

Mori S., Sakakibara M., Tanimoto A. (1974) Steady Heat Transfer to Laminar Flow in Circular Tube with Conduction in the Tube Wall. Heat Transfer-Japanese Research 3:37-46

Murray W.M. (1938) Heat Dissipation Through an Annular Disk or Fin of Uniform Thickness. Journal of Applied Mechanics 60:A-78.

O'Donovan T.S., Murray D.B. (2007) Jet Impingement Heat Transfer – Part I: Mean and Root-Mean-Square Heat Transfer and Velocity Distributions. International Journal of Heat and Mass Transfer 50:3291-3301

Patricelli L. (2007) Application of Liquid Crystals Thermography in a Cooling Channel for Turbine Blade. VKI STP Report, von Karman Institute for Fluid Dynamics, Rhode-St-Genèse, Belgium

Perelman T.L. (1961) On Conjugated Problems of Heat Transfer. International Journal of Heat and Mass Transfer 3:293-304

Poser R., von Wolfersdorf J., Lutum J., and Semmler K. (2008) Performing Heat Transfer Experiments in Blade Cooling Circuits Using a Transient Technique With Thermochromic Liquid Crystals. ASME Paper GT2008-50364, ASME Turbo Expo 2008, Berlin, Germany

Poser R., von Wolfersdorf J., Lutum E. (2007) Advanced Evaluation of Transient Heat Transfer Experiments Using Thermochromic Liquid Crystals. Proceedings of IMechE – Part A: Journal of Power and Energy 221:793-801

Rabin Y. (2003) A general Model for the Propagation of Uncertainty in Measurements Into Heat Transfer Simulations and its Applications to Cryosurgery. Cryobiology 46:109-120

Raffel M., Willert C., Kompenhans J. (1998) Particle Image Velocimetry, A Practical Guide. Springer, Berlin Heidelberg New York

Rau G., Vanhalst J., Arts T. (1993) The Application of Liquid Crystal Techniques to Determine Heat Transfer Rates. In: Measurement Techniques in Fluid Dynamics. VKI Lecture Series, von Karman Institute for Fluid Dynamics, Rhode-St-Genèse, Belgium

Rau G., Çakan M., Moeller D., Arts T. (1998) The Effect of Periodic Ribs on the Local Aerodynamic and Heat Transfer Performance of a Straight Cooling Channel. Journal of Turbomachinery 120:368–375

Rhee D.H., Nam Y.W., Cho H.H. (2004) Local Heat/Mass Transfer With Various Rib Arrangements in Impingement/Effusion Cooling With Crossflow. Journal of Turbomachinery 126:615-626

Saha K., Guo S., Acharya S., Nakamata C. (2008) Heat Transfer and Pressure Measurements in a Lattice-Cooled Trailing Edge Of a Turbine Airfoil. ASME Paper GT2008-51324, ASME Turbo Expo 2008, Berlin, Germany

Saravanamuttoo H.I.H., Rogers G.F.C., Cohen H., Straznicky P.V. (2001) Gas Turbine Theory. 5th ed., Prenitce Hall

Scarano F., Riethmuller M.L. (2000) Advances in Iterative Multigrid PIV Image Processing. Experiments in Fluids 29:S51-S60

Scarano F., Riethmuller M.L. (ed.) (2009) Recent Advances in Particle Image Velocimetry. VKI Lecture Series, von Karman Institute for Fluid Dynamics, Rhode-St-Genèse, Belgium

Schlichting H. (1979) Boundary Layer Theory. 7th edition, McGraw-Hill, New York

Scialanga M. (2009) Conjugate Heat Transfer in Turbine Blade Trailing Edge Cooling Channel. VKI STP Report, von Karman Institute for Fluid Dynamics, Rhode-St-Genèse, Belgium

Segura D., Acharya S. (2010) Internal Cooling Using Novel Swirl Enhancement Strategies in a Slot Shaped Single Pass Channel. ASME Paper GT2010-23679, ASME Turbo Expo 2010, Glasgow, UK

Shah R.K., London A.L. (1978) Laminar Flow Forced Convection in Ducts. Academic Press, New York

Shen J.R., Wang Z., Ireland P.T., Jones T.V., Byerley A.R. (1996) Heat Transfer Enhancement Within a Turbine Blade Cooling Passage Using Ribs and Combinations of Ribs With Film Cooling Holes. Journal of Turbomachinery 118:428-434

Smith B.R. (1994) A Near Wall Model for the k-l Two-Equation Turbulence Model. AIAA paper 94-2386.

Son S.Y., Kihm K.D., Han J.-C. (2002) PIV Flow Measurements for Heat Transfer Characterization in Two-Pass Square Channels With Smooth and 90° Ribbed Walls. International Journal of Heat and Mass Transfer Volume 45:4809-4822

Spring S., Weigand B. (2010) Jet Impingement Heat Transfer. In: Internal Cooling in Turbomachinery. VKI Lecture Series, von Karman Institute for Fluid Dynamics, Rhode-St-Genèse, Belgium

Stasiek J., Madaj T., Mikielewicz J. (1999) Temperature Indicators. In: The Measurement Instrumentation and Sensors Handbook, J.G. Webster (ed.), CRC Press

Taslim M.E., Spring S.D. (1994) Effects of Turbulator Profile and Spacing on Heat Transfer and Friction in a Channel. Journal of Thermophysics & Heat Transfer 8:555-562

Taslim M.E., Li T., Spring S.D. (1995) Experimental Study of the Effects of Bleed Holes on Heat Transfer and Pressure Drop in Trapezoidal Passages With Tapered Turbulators. Journal of Turbomachinery 117:281-289

Taslim M.E., Li T., Spring S.D. (1997) Measurement of Heat Transfer Coefficient s and Friction Factors in Rib-Roughened Channels Simulating Leading-Edge Cavities of a Modern Turbine Blade. Journal of Turbomachinery 119:411-419

Taslim M. E., Li T., Spring, S.D. (1998) Measurements of Heat Transfer Coefficients in Rib-Roughened Trailing-Edge Cavities With Crossover Jets. ASME Paper 98-GT-435, ASME Turbo Expo 1998, Stockholm, Sweden

Taslim M.E., Bakhtari K., Liu H. (2003) Experimental and Numerical Investigation of Impingement on a Rib-Roughened Leading Edge Wall. Journal of Turbomachinery 125:682-691

Thibault D., Fénot M., Lalizel G., Dorignac E. (2009) Experimental Study of Heat Transfer From Impinging Jet With Upstream and Downstream Crossflow. International Symposium on Heat Transfer in Gas Turbine Systems, Antalya, Turkey

Van Treuren K.W., Wang Z., Ireland P.T., Jones T.V. (1994) Detailed Measurements of Local Heat Transfer Coefficient and Adiabatic Wall Temperature Beneath an Array of Impinging Jets. Journal of Turbomachinery 116:369-374

Verstraete T., Amaral S., Van den Braembussche R., Arts T. (2010) Design and Optimization of the Internal Cooling Channels of a High Pressure Turbine Blade – Part II: Optimization. Journal of Turbomachinery 132:021014 (9 pages)

Viskanta R. (1993) Heat Transfer to Impinging Isothermal Gas and Flame Jets. Experimental Thermal and Fluid Science 6:111-134

von Wolfersdorf J., Weigand B. (2010) Turbine Blade Internal Cooling – Selected Experimental Approaches. In: Internal Cooling in Turbomachinery. VKI Lecture Series, von Karman Institute for Fluid Dynamics, Rhode-St-Genèse, Belgium

Wang Z., Ireland P.T., Jones T.V. (1995) An Advanced Method of Processing Liquid Crystal Video Signals From Transient Heat Transfer Experiments. Journal of Turbomachinery 117:184-189

Wang Z., Ireland P.T., Kohler S.T., Chew J.W. (1998) Heat Transfer Measurements to a Gas Turbine Cooling Passage With Inclined Ribs. Journal of Turbomachinery 120:63-69

Webb B.W., Ramadhyani S. (1985) Conjugate Heat Transfer in a Channel With Staggered Ribs. International Journal of Heat and Mass Transfer 28:1679-1687

Weigand B., Semmler K., von Wolfersdorf J. (2006) Heat Transfer Technology for Internal Passages of Air-Cooled Blades for Heavy-Duty Gas Turbines. Annals of the New York Academy of Sciences 934:179-193

Weigand B., Simon V. (2006) Laws of Similarity in Fluid Mechanics. In: Flow Phenomena in Nature: A challenge to Engineering Design, R. Liebe (ed.), WIT Press

Wereley T., Gui L., Meinhart C.D. (2002) Advanced Algorithms for Microscale Particle Image Velocimetry. AIAA Journal 40:1047-1055

Westerweel J., Scarano F. (2005) Universal outlier detection for PIV data. Experiments in Fluids 39: 1096-1100

Willert C.E., Gharib M. (1991) Digital particle image velocimetry. Experiments in Fluids 10:181-193

Willert C. E. (1996) The Fully Digital Evaluation of Photographic PIV Recordings. Applied Scientific Research 56:79-102

Willockx A. (2009) Using the Inverse Heat Conduction Problem and Thermography for the Determination of Local Heat transfer Coefficients and Fin Effectiveness for Longitudinal Fins. Ph.D. dissertation, University of Ghent, Belgium

Young T.J., Vafai K. (1998) Convective Cooling of a Heated Obstacle in a Channel. International Journal of Heat and Mass Transfer 41:3131-3148

Younis, B.A. (2010) Modeling the Turbulent Scalar Fluxes. In: Internal Cooling in Turbomachinery. VKI Lecture Series, von Karman Institute for Fluid Dynamics, Rhode-St-Genèse, Belgium

# Appendix A – Uncertainty analysis

The absolute and relative uncertainties associated to the measured quantities are reported in Tab. A.1. The estimation of the uncertainty is based on the Gaussian error propagation equation, as described by Kline and McClintock (1953) and Moffat (1988). Let $q$ be a quantity depending on $n$ independent parameters $p_1,\ldots, p_n$:

$$q = f(p_1,...,p_n) \tag{A.1}$$

| Quantity | Symbol | Nominal value | Absolute uncertainty | Relative uncertainty |
|---|---|---|---|---|
| Reynolds number | $Re$ | 67500 [-] | 1300 | 2.9% |
| Air density | $\rho$ | 1.198 [kgm$^{-3}$] | 0.004 kg m$^{-3}$ | 0.35% |
| Air pressure | $P$ | 101000 [Pa] | 3 [Pa] | 0.003% |
| Air temperature | $T_f$ | 293.15 [K] | 0.15 [K] | 0.05% |
| Air dynamic viscosity | $\mu$ | $1.8\cdot10^{-5}$ [kgm$^{-1}$s$^{-1}$] | $6.7\cdot10^{-9}$ [kg m$^{-1}$s$^{-1}$] | 0.04% |
| Air conductivity | $k_f$ | 0.026 [Wm$^{-1}$K$^{-1}$] | $1.2\cdot10^{-5}$ [Wm$^{-1}$K$^{-1}$] | 0.05% |
| Inlet hydraulic diameter | $D_{inlet}$ | 0.0814 [m] | 0.001 [m] | 1.2% |
| Mid-wall slot hydr. diam. | $D_{mid}$ | 0.0219 [m] | 0.001 [m] | 4.5% |
| Inlet air velocity | $U_b$ | 12.8 [m/s] | 0.33 [m/s] | 2.6 % |
| Air dynamic pressure | $P_{dyn}$ | 100 [Pa] | 3 [Pa] | 3% |
| Heat transfer area | $A_h$, $A_0$ | 216000 [mm$^2$] | 1315 [mm$^2$] | 0.6% |
| Joule power (convective) | $Q_{Joule}$ | 270 [W] | 2.8 [W] | 1% |
| Convective power heat | $Q_{conv}$ | 245 [W] | 8 [W] | 3% |
| Joule power (conjugate) | $Q_0$ | 325 [W] | 6.5 [W] | 2% |
| Wall temperature (TLC) | $T_w$ | 308 - 329 [K] | 0.78 [K] | 0.02% |
| Wall temperature (IR) | $T_w$ | 305 - 325 [K] | 0.5 [K] | 0.015% |
| Non-dimens. wall temp. | $\Theta$ | 0.01 | 0.0005 - 0.0009 | 5 - 9 % |
| Heat transf coeff. (conv.) | $h$ | 69 [Wm$^{-1}$K$^{-2}$] | 3 - 6.5 [Wm$^{-1}$K$^{-2}$] | 5 - 11% |
| Heat transf. coeff. (conj.) | $h$ | 80 [Wm$^{-1}$K$^{-2}$] | 9.6 [Wm$^{-1}$K$^{-2}$] | 12% |
| Nusselt number (conv.) | $Nu$ | 60 | 4.1 - 8.3 | 6 - 12% |
| Nusselt number (conj.) | $Nu$ | 70 | 9.1 | 13% |
| Mean velocity (PIV) | $U$ | 12.8 [m/s] | 0.256 [m/s] | 2% |
| rms vel fluctuation (PIV) | $rms(u)$ | 2.56 [m/s] | 0.128 [m/s] | 5% |

**Tab. A.1 Absolute and relative uncertainty of the measured quantities**

For small variations of the parameters $p_i$, the effect of the uncertainties $\delta p_i$ on the total uncertainty $\delta q$ can be expressed in linear form:

$$\delta q = \sqrt{\sum_{i=1}^{n} \left( \frac{\partial q}{\partial p_i} \delta p_i \right)^2} \tag{A.2}$$

where the term $\partial q/\partial p_i$ is the sensitivity coefficient expressing the dependence of $q$ on $p_i$. The reported uncertainties are based on a 95% confidence level. When is felt that the mutual independency of the different sources of error is not clearly assessed, a more conservative estimation is given summing up the absolute values of the different errors. Uncertainties estimated in such manner are labeled as "direct summation" in the following. For the most relevant quantities a detailed arborescence of the sensitivity coefficients is presented.

## *A.1 – Inlet Reynolds number*

$$\mathrm{Re} = \frac{\rho u D_{inlet}}{\mu} \tag{A.3}$$

$$\delta \mathrm{Re} = \sqrt{\left( \frac{\partial \mathrm{Re}}{\partial \rho} \right)^2 \delta\rho^2 + \left( \frac{\partial \mathrm{Re}}{\partial u} \right)^2 \delta u^2 + \left( \frac{\partial \mathrm{Re}}{\partial D_{inlet}} \right)^2 \delta D_{inlet}^2 + \left( \frac{\partial \mathrm{Re}}{\partial \mu} \right)^2 \delta\mu^2} = \tag{A.4}$$

$$= \mathrm{Re} \sqrt{\left( \frac{\delta\rho}{\rho} \right)^2 + \left( \frac{\delta u}{u} \right)^2 \delta u^2 + \left( \frac{\delta D_{inlet}}{D_{inlet}} \right)^2 + \left( -\frac{\delta\mu}{\mu} \right)^2}$$

The relative uncertainty is $\delta Re/Re = 2.9\%$.

**Inlet hydraulic diameter:**

$D_{inlet} = 81.4$ mm
$\delta D_{inlet} = 1$ mm

The relative uncertainty is $\delta D_{inlet}/D_{inlet} = 1.2\%$.

**Inlet air density:**

$$\rho = \frac{P}{RT_f} \tag{A.5}$$

$$\delta\rho = \sqrt{\left(\frac{\partial\rho}{\partial P}\right)^2 \delta P^2 + \left(\frac{\partial\rho}{\partial T_f}\right)^2 \delta {T_f}^2} = \sqrt{\left(\frac{\delta P}{R T_f}\right)^2 + \left(\frac{-P}{R {T_f}^2}\delta T_f\right)^2} \tag{A.6}$$

where:

$T_f$ = 293.15 K
$P$ = 101325 Pa
$\delta T_f$ = 0.15 K
$\delta P$ = 3 Pa
$R$ = 287.1 J kg$^{-1}$K$^{-1}$ (specific gas constant for air)

The relative uncertainty is $\delta\rho/\rho$ = 0.35%.

**Inlet air dynamic viscosity:**

$$\mu = \frac{a T_f^n}{b + T_f} \tag{A.7}$$

$$\delta\mu = \sqrt{\left(\frac{\partial\mu}{\partial T_f}\right)^2 \delta T_f^2} = \sqrt{\left(\frac{n a T_f^{n-1}\left(b + T_f\right) - a T_f^n}{\left(b + T_f\right)^2}\right)^2 \delta T_f^2} \tag{A.8}$$

where:

$a$ = 1.485 [kg m$^{-1}$s$^{-1}$K$^{-0.5}$]
$b$ = 110.4 [K]
$n$ = 1.5 [-]
$\delta T_f$ = 0.15 K

The relative uncertainty is $\delta\mu/\mu$ = 0.04%.

**Inlet air velocity:**

$$U_b = \sqrt{2\frac{P_{dyn}}{\rho}} \tag{A.9}$$

$$\delta U_b = \sqrt{\left(\frac{\partial U_b}{\partial P_{dyn}}\right)^2 \delta P_{dyn}^2 + \left(\frac{\partial U_b}{\partial \rho}\right)^2 \delta\rho^2} = \sqrt{\left(\frac{1}{\sqrt{2\frac{P_{dyn}}{\rho}}}\right)^2 \delta P_{dyn}^2 + \left(-\sqrt{\frac{P_{dyn}}{2\rho^3}}\right)^2 \delta\rho^2} \tag{A.10}$$

where:

$P_{dyn}$ = 100 Pa
$\rho$ = 1.19 kg m$^{-3}$
$\delta P_{dyn}$ = 3 Pa
$\delta\rho$ = 0.004 kg m$^{3}$

The relative uncertainty is $\delta U_b/U_b$ = 2.6%.

## *A.2 – In plane velocity measured by PIV*

The analysis in section 4.2.5 holds (see Eq. 4.2 and 4.3). The relative uncertainty for the mean velocity is $\delta U/U$ = 2%, while the relative uncertainty for the rms of the in plane velocity fluctuation is $\delta rms(u)/rms(u)$ = 5%.

## *A.3 – Nusselt number in convective regime*

$$Nu = \frac{hD_{mid}}{k_f} \tag{A.11}$$

$$\delta Nu = \sqrt{\left(\frac{\partial Nu}{\partial h}\right)^2 \delta h^2 + \left(\frac{\partial Nu}{\partial D_{mid}}\right)^2 \delta D_{mid}^2 + \left(\frac{\partial Nu}{\partial k_f}\right)^2 \delta k_f^2} = \tag{A.12}$$

$$= \sqrt{\left(\frac{D_{mid}}{k_f}\right)^2 \delta h^2 + \left(\frac{h}{k_f}\right)^2 \delta D_{mid}^2 + \left(-\frac{hD_{mid}}{k_f^2}\right)^2 \delta k_f^2}$$

The relative uncertainty is $\delta Nu/Nu$ = 6% to 12 %.

**Mid-wall slots hydraulic diameter**

$D_{mid}$ = 21.9 mm
$\delta D_{mid}$ = 1 mm

The relative uncertainty is $\delta D_{mid}/D_{mid}$ = 4%.

**Air thermal conductivity**

$$k_f = \mathrm{A}\, T_f^3 + \mathrm{B}\, T_f^2 + \mathrm{C}\, T_f + \mathrm{D} \tag{A.13}$$

$$\delta k_f = \sqrt{\left(\frac{\partial k_f}{\partial T_f}\right)^2 \delta T_f^2} = \sqrt{\left(3AT_f^2 + 2BT_f + C\right)^2 \delta T_f^2} \qquad \text{(A.14)}$$

where:

A = $1.5207 \cdot 10^{-11}$ [$Wm^{-1}K^{-4}$]
B = $4.8574 \cdot 10^{-8}$ [$Wm^{-1}K^{-3}$]
C = $1.0184 \cdot 10^{-4}$ [$Wm^{-1}K^{-2}$]
D = $3.9333 \cdot 10^{-4}$ [$Wm^{-1}K^{-1}$]
$\delta T_f$ = 0.15 K

The relative uncertainty is $\delta k_f / k_f$ = 0.05%.

**Heat transfer coefficient**

$$h = \frac{Q_{conv}}{A_h \theta} \qquad \text{(A.15)}$$

where $\theta = (T_w - T_f)$ is the wall-to-fluid temperature difference.

$$\delta h = \sqrt{\left(\frac{\partial h}{\partial Q_{conv}}\right)^2 \delta Q_{conv}^2 + \left(\frac{\partial h}{\partial A_h}\right)^2 \delta A_h^2 + \left(\frac{\partial h}{\partial \theta^2}\right)^2 \delta \theta^2} = \qquad \text{(A.16)}$$

$$= \sqrt{\left(\frac{1}{A_h \theta}\right)^2 \delta Q_{conv}^2 + \left(-\frac{Q_{conv}}{A_h^2 \theta}\right)^2 \delta A_h^2 + \left(-\frac{Q_{conv}}{A_h \theta^2}\right)^2 \delta \theta^2}$$

The relative uncertainty is $\delta h / h$ = 5% to 11% depending on which TLC mixture is active.

**Convective power heat**

$$Q_{conv} = Q_{Joule} - Q_{rad} - Q_{cond,h} \qquad \text{(A.17)}$$

$$\delta Q_{conv} = \sqrt{\delta Q_{Joule}^2 + \delta Q_{rad}^2 + \delta Q_{cond,h}^2} \qquad \text{(A.18)}$$

$$Q_{Joule} = VI \qquad \text{(A.19)}$$

$$\delta Q_{Joule} = \sqrt{\left(\frac{\partial Q_{Joule}}{\partial V}\right)^2 \delta V^2 + \left(\frac{\partial Q_{Joule}}{\partial I}\right)^2 \delta I^2} = \sqrt{I^2 \delta V^2 + V^2 \delta I^2} \tag{A.20}$$

where:

$Q_{rad} = 0.02Q_{Joule}$ to $0.07Q_{Joule}$ on the floor and on the opposite smooth wall (negligible on rib's surface)
$Q_{cond,h} = 0.05Q_{Joule}$ on the inter-rib floor, $0.07Q_{Joule}$ (in absolute value) on rib's surface and $0.1Q_{Joule}$ on the opposite smooth wall
$\delta Q_{rad} = 0.3Q_{rad}$
$\delta Q_{cond,h} = 0.3Q_{cond,h}$
$\delta Q_{conv} = 0.025Q_{conv}$ on the ribbed wall
$0.04Q_{conv}$ on the opposite smooth wall

The relative uncertainty is $\delta Q_{conv}/Q_{conv} = 3\%$.

**Heated area**

$$A_h = H \cdot W \tag{A.21}$$

$$\delta A_h = \sqrt{\left(\frac{\partial A_h}{\partial H}\right)^2 \delta H^2 + \left(\frac{\partial A_h}{\partial W}\right)^2 \delta W^2} = \sqrt{\left(W \delta H\right)^2 + \left(H \delta W\right)^2} \tag{A.22}$$

where:

$W = 185$ mm width of the heated area
$H = 1200$ mm length of the heated area
$\delta W = 1$ mm
$\delta H = 3$ mm

The relative uncertainty is $\delta A_h/A_h = 0.6\%$.

**Wall-to-fluid temperature difference**

$$\theta = (T_w - T_f) \tag{A.23}$$

$$\delta\theta = \sqrt{\left(\frac{\partial \theta}{\partial T_w}\right)^2 \delta T_w^2 + \left(\frac{\partial \theta}{\partial T_f^2}\right)^2 \delta T_w^2} = \sqrt{\delta T_w^2 + \delta T_f^2} \tag{A.24}$$

The relative uncertainty is $\delta\theta/\theta = 2.3\%$ to $5.5\%$ depending on which TLC mixture is active.

**Wall temperature**

$T_w$ = 308 K for R35C5W
329 K for R55C5W

$$\delta T_w = \sqrt{\delta T_{TLC}{}^2 + \delta T_{detection}{}^2} \tag{A.25}$$

$$\delta T_{TLC} = \delta T_{TC} + \delta T_{cal} \text{ (direct summation)} \tag{A.26}$$

$$\delta T_{detection} = \frac{\delta pxl}{M} \nabla T_w \tag{A.27}$$

where:

$\delta T_{TLC}$ = 0.35 K is the uncertainty on the TLC temperature
$\delta T_{TC}$ = 0.15 K is the uncertainty associated to the thermocouples
$\delta T_{cal}$ = 0.2 K is the uncertainty associated to the TLC calibration curve
$\delta T_{detection}$ = 0.7 K is the uncertainty associated to the detection of the isolines
$\delta pxl$ = 4 pixels is the maximum when detecting isolines within the images
$M$ = 3 pxl/mm is the average magnification factor when imaging the wall surface
$\nabla T_w$ = 0.5 K/mm is the spatial temperature gradient along the wall surface

The relative uncertainty is $\delta T_w/T_w$= 0.05%.

**Inlet flow temperature**

$T_f$ = 293.15
$\delta T_f$ = 0.15 k (thermocouple uncertainty)

The relative uncertainty is $\delta T_f/T_f$= 0.05%.

## *A.4 – Non-dimensional temperature in conjugate regime*

$$\Theta = \frac{A_0 k_f \theta}{Q_0 D_{mid}} \tag{A.28}$$

where $\theta = (T_w - T_f)$ is the wall-to-fluid temperature difference and $Q_0$ is the power input at the outer side of the ribbed wall. Neglecting the uncertainty on the air conductivity, it is:

$$\delta\Theta = k_f \sqrt{\left(\frac{\partial\Theta}{\partial\theta}\right)^2 \delta\theta^2 + \left(\frac{\partial\Theta}{\partial A_0}\right)^2 \delta A_0^2 + \left(\frac{\partial\Theta}{\partial Q_0}\right)^2 \delta Q_0^2 + \left(\frac{\partial\Theta}{\partial D_{mid}}\right)^2 \delta D_{mid}^2} = \tag{A.29}$$

$$= k_f \sqrt{\left(\frac{A_0}{Q_0 D_{mid}}\right)^2 \delta\theta^2 + \left(\frac{\theta}{Q_0 D_{mid}}\right)^2 \delta A_0^2 + \left(-\frac{A_0\theta}{Q_0^2 D_{mid}}\right)^2 \delta Q_0^2 + \left(\frac{A_0\theta}{Q_0^2 D_{miid}^2}\right)^2 \delta D_{mid}^2}$$

The relative uncertainty is $\delta\Theta/\Theta$ = 5% to 9% depending on the surface location.

**Heated area**

For $A_0$ and $\delta A_0$ the analysis in section A.2 holds, being $A_0 = A_h$ and $\delta A_0 = \delta A_h$
The relative uncertainty is $\delta A_0/A_0$ = 0.6%

**Power heat**

$$Q_0 = Q_{Joule} - Q_{cond} \tag{A.30}$$

$$\delta Q_{conv} = \delta Q_{Joule} + \delta Q_{cond} \text{ (direct summation)} \tag{A.31}$$

$$Q_{cond} = 0.01 Q_{Joule} \tag{A.32}$$

$$\delta Q_{cond} = 0.3 Q_{cond} \tag{A.33}$$

For $Q_{Joule}$ and $\delta Q_{Joule}$ the analysis in section A.2 holds.
The relative uncertainty is $\delta Q_0/Q_0$ = 1.5%.

**Mid-wall slots hydraulic diameter**

$D_{mid}$ = 81.4 mm
$\delta D_{mid}$ = 1 mm

The relative uncertainty is $\delta D_{mid}/D_{mid}$ = 4.5%.

**Wall-to-fluid temperature difference**

For $\theta$ and $\delta\theta$ the analysis in section A.2 holds.
The relative uncertainty is $\delta\theta/\theta$ = 3% to 6.8% depending on the surface location.

**Wall temperature**

$T_w$ = 305 to 325 K over the investigated surface

$$\delta T_w = \sqrt{\delta T_{TC}{}^2 + \delta T_{isotherm}{}^2 + \delta T_{film}{}^2} \tag{A.34}$$

where:

$\delta T_{TC}$ = 0.15 K is the uncertainty associated to the thermocouples
$\delta T_{isotherm}$ = 0.4 K is the uncertainty due to the non-isothermal wall during calibration
$\delta T_{film}$ = 0.2 K is the uncertainty due to the non-isothermal polyethylene film during measurements

The relative uncertainty is $\delta T_w/T_w$= 0.015%.

## *A.5 – Nusselt number in conjugate regime*

$$Nu = \frac{hD_{mid}}{k_f} \tag{A.35}$$

Neglecting the uncertainty on the air conductivity, it is:

$$\delta Nu = \frac{1}{k_f}\sqrt{\left(\frac{\partial Nu}{\partial h}\right)^2 \delta h^2 + \left(\frac{\partial Nu}{\partial D_{mid}}\right)^2 \delta D_{mid}^2} = \sqrt{D_{mid}^2 \delta h^2 + h^2 \delta D_{mid}^2} \tag{A.36}$$

The relative uncertainty is $\delta Nu/Nu$ = 13 %

**Heat transfer coefficient**

The heat transfer coefficient $h$ obtained in conjugate regime is the result of a 3D finite element analysis, therefore it cannot be expressed analytically. The method proposed by Rabin (2003) is applied to estimate the propagation of the uncertainty in a situation where measured data are used as input to numerical calculations. Assuming that the solution is independent on the mesh size, the value of $h$ depends on the parameters used in the calculation and on the accuracy inherent to the method:

$$h = f(q_{kw}, q_{Tw}, q_{Tf}, q_{q0}, method) \tag{A.37}$$

where:

$q_{kw}$ = the value of the thermal conductivity assumed for the wall material

$q_{Tw}$ = the distribution of the wall surface temperature imposed on the streamlined surface
$q_{Tf}$ = the value of the reference fluid temperature
$q_{q0}$ = the level of the uniform heat flux imposed at the outer side of the wall
*method* = accuracy related to the method

The uncertainty on $h$ can be then expressed as:

$$\delta h = \sqrt{\frac{\partial h}{\partial q_{kw}}\delta q_{kw}^2 + \frac{\partial h}{\partial q_{Tw}}\delta q_{Tw}^2 + \frac{\partial h}{\partial q_{Tf}}\delta q_{Tf}^2 + \frac{\partial h}{\partial q_{q0}}\delta q_{q0}^2 + \delta h_{method}^2} \qquad \text{(A.38)}$$

$\delta h_{method}$ is evaluated applying the iterative method to the wall temperature distribution obtained by FEM calculation from a synthetic map of $h$, as discussed in section 4.4.4. It is estimated that $\delta h_{method} = 0.05h$.
To evaluate each sensitivity coefficient $\partial h/\partial q_i$ a calculations is run modifying the nominal value of $q_i$ by its uncertainty $\delta q_i$, and evaluating the corresponding area-average difference $\delta h$. The influence of $q_{kw}$ and $q_{Tf}$ is negligible, while the level of heat flux q0 affects h by 2% (consistently with the fact that $\delta q_0/q_0 \approx \delta Q_0/Q_0 = 2\%$). The main factor is of course $T_w$: an offset of 0.5 K determines a difference in area-average $h$ of about 12%. Only uniform shifts to the imposed temperature distribution are considered, as the iterative approach shows little sensitivity to measurement noise.
Overall the relative uncertainty is $\delta h/h = 12.2$ %.

# Appendix B – Publications

The present thesis is based on the work contained in the following publications.

## ARCHIVAL PUBLICATIONS

Coletti F., Scialanga M., Arts T. (2010) Experimental Investigation of Conjugate Heat Transfer in a Rib-Roughened Trailing Edge Channel With Crossing-Jets. Journal of Turbomachinery - Under review

Armellini A., Coletti F., Arts T., Scholtes C. (2010) Aero-Thermal Investigation of a Rib-Roughened Trailing Edge Channel With Crossing-Jets - Part I: Flow field Analysis. Journal of Turbomachinery 132:011009 (9 pages)

Coletti F., Armellini A., Arts T., Scholtes C. (2010) Aero-Thermal Investigation of a Rib-Roughened Trailing Edge Channel With Crossing-Jets - Part II: Heat Transfer Analysis. Journal of Turbomachinery - In press

## CONFERENCES PROCEEDINGS

Coletti F., Scialanga M., Arts T. (2010) Experimental Investigation of Conjugate Heat Transfer in a Rib-Roughened Trailing Edge Channel With Crossing-Jets. ASME Paper GT2010-22432, ASME Turbo Expo 2010, Glasgow, UK

Coletti F., Arts T. (2010) Experimental Study of Conjugate Heat Transfer in Internal Cooling Channel. In: Internal Cooling in Turbomachinery. VKI Lecture Series, von Karman Institute for Fluid Dynamics, Rhode-St-Genèse, Belgium

Coletti F., Scialanga M., Arts T. (2009) Conjugate Heat Transfer in a Turbine Blade Internal Cooling Channel. 8th National Congress on Theoretical and Applied Mechanics, Brussels, Belgium

Coletti F., Facchinetti E., Arts T. (2009) Effect of Inclined Ribs on the Aero-Thermal Performance of a Trailing Edge Cavity With Crossing Jets". 8$^{th}$ European Turbomachinery Conference, Graz, Austria

Armellini A., Coletti F., Arts T., Scholtes C. (2008) Aero-Thermal Investigation of a Rib-Roughened Trailing Edge Channel With Crossing-Jets - Part I: Flow field Analysis. ASME Paper GT2010-50694, ASME Turbo Expo 2008, Berlin, Germany

Coletti F., Armellini A., Arts T., Scholtes C. (2008) Aero-Thermal Investigation of a Rib-Roughened Trailing Edge Channel With Crossing-Jets - Part II: Heat Transfer Analysis. ASME Paper GT2010-50695, ASME Turbo Expo 2008, Berlin, Germany

# Curriculum vitae

## Filippo Coletti

born: June 17th 1982 in Perugia, Italy

address: 617, Chaussée de Boondael
1050 Bruxelles, Belgium
office phone: +32 (0) 23 59 97 66
office email: coletti@vki.ac.be
permanent email: filippo.coletti@gmail.com

### EDUCATION

**Ph.D. candidate** (expect to defend in October 2010) **from September 2006**
Turbomachinery and Propulsion Department
von Karman Institute for Fluid Dynamic, Belgium

Institute of Aerospace Thermodynamics
University of Stuttgart, Germany

**Diploma Course in Fluid Dynamics** **June 2006**
Turbomachinery and Propulsion Department
von Karman Institute for Fluid Dynamics, Belgium

**M.Sc.** **October 2005**
Faculty of Mechanical Engineering
University of Studies of Perugia, Italy

**B.Sc.** **September 2003**
Faculty of Mechanical Engineering
University of Studies of Perugia, Italy

### REFERENCES

Tony Arts
Turbomachinery & Propulsion Department, Head
von Karman Institute for Fluid Dynamics, Belgium
arts@vki.ac.be

Bernhard Weigand
Institute of Aerospace Thermodynamics, Head
University of Stuttgart, Germany
bernhard.weigand@itlr.uni-stuttgart.de

### LANGUAGES

Italian – native
English – fluent
French – fluent
Spanish – fluent